Dipl.-Ing. Katharina Gruber, BSc

Investigation of the electrochemical behaviour of macroporous carbon/sulfur electrodes and lithium metal electrodes in lithium-sulfur batteries

DOCTORAL THESIS

to achieve the university degree of

Doktorin der technischen Wissenschaften

submitted to

Graz University of Technology

Supervisor

Univ.-Prof. Dipl.-Ing. Dr.techn. Stelzer Franz

Institute for Chemistry and Technology of Materials

In Cooperation with VARTA Micro Innovation GmbH

Graz, June 2015

AFFIDAVIT

I declare that I have authored this thesis independently, that I have not used other than the declared sources/resources, and that I have explicitly indicated all material which has been quoted either literally or by content from the sources used. The text document uploaded to TUGRAZonline is identical to the present doctoral thesis.

Date	Signatur

Acknowledgements

I would like to express my gratitude to my supervisor, head of the Institute for Chemistry and Technology of Materials (ICTM) at TU Graz, Prof. Dipl.-Ing.Dr. techn. Franz Stelzer for giving me the opportunity to conduct this PhD thesis under his guidance.

Moreover, I wish to express my sincere thanks to Dr. Stefan Koller, CEO of Varta Micro Innovation GmbH Graz, for the chance to perform this PhD thesis in his company, for providing the research facilities and for the financial support. I would particularly like to thank Dr. Martin Schmuck, my project manager, for his support and encouragement during the past years of my thesis. I would also like to thank Dr. Bernd Fuchsbichler who filled this role in the beginning of my thesis.

Additionally I would like to deeply thank Dr. Sebastijan Kovačič, in those days post doc at ICTM, for cooperation and guidance.

Further I would like to express my real gratitude to my international colleagues as part of the LISA and MALISU project, for many fruitful discussions and for sharing their excellent scientific work at the project meetings.

I am honestly thankful for the chance to work with such great colleagues who became friends along the way. In this context, I want to truly thank Dipl.-Ing. Patricia Handel for her great scientific support and for becoming such a good friend. I especially want to thank Katja Kapper and Dipl.-Ing. Gisela Fauler for their support, for productive discussions and fun along the way. Further I want to express my gratitude to Dr. Colin God for his support especially during the time of writing my thesis. Additionally I want to thank Stephania Toulis, Christian Baumann, Christian Lenardt, MSc. Pierre Baumann, Dr. Christoph Stangl, Andrea Droisner and Dr. Harald Krenn. And last but not least, I want to acknowledge all scientific and non-scientific staff members of the ICTM.

Finally, I would like to thank my parents, my brother and Markus Petroczy, who support me in any situation!

Abstract

The exploitation of renewable energy sources, like wind and solar power, requires temporary storage of energy since there is often a mismatch of energy delivery and energy demand. Moreover, e.g. in the automotive sector, extended driving ranges of electric-vehicles at reasonable costs are more and more required.

Lithium ion batteries (LIB) are the technology of choice for many applications due to their high energy densities and long cycle lives. However, to meet the increasing energy density requirements and at the same time to reduce the costs, extensive research activities are devoted in the field of so-called *beyond LIB technologies*, like lithium-sulfur or lithium-air batteries. These systems especially convince because of their high theoretical energy densities that theoretically outperform LIB technology many times over. Nevertheless, these systems are still plagued by several drawbacks that delay their commercialization.

This thesis deals with different technological aspects of Li-S cells. On the one hand, the manufacturing process of macroporous HIPE-structured (high internal phase emulsion) carbon/sulfur electrodes is presented and their electrochemical performance in Li-S cells is evaluated. On the other hand, the behaviour of lithium metal negative electrode during electrochemical charge-discharge sequences is investigated. Finally, energy density calculations on Li-S cells and predictions on energy densities in dependence of several electrode parameters are discussed.

Kurzfassung

Bei der Gewinnung von elektrischer Energie aus erneuerbaren Energiequellen, wie etwa aus Wind- oder Sonnenkraft, decken sich Energieerzeugung und Nachfrage zeitlich nur selten, wodurch sich die Notwendigkeit der Zwischenspeicherung ergibt. Des Weiteren werden z.B. im Automotivbereich immer längere Reichweiten ausschließlich elektrisch betriebener Fahrzeuge verlangt.

Aufgrund ihrer hohen Energiedichten und Lebensdauern werden momentan für viele dieser Belange Lithium Ionen Batterien (LIB) eingesetzt. Um jedoch den steigenden Anforderungen bezüglich höherer Energiedichten bei gleichzeitig sinkenden Kosten gerecht zu werden, konzentriert sich die Forschung zunehmend auf sogenannte *beyond LIB Batterietechnologien*, wie etwa Lithium-Schwefel oder Lithium-Luft Systemen. Diese überzeugen vor allem durch ihre hohen theoretischen Energiedichten, die jene von LIBs um ein Vielfaches übersteigen. Allerdings sind diese Systeme derzeit noch von Nachteilen geprägt, welche eine Kommerzialisierung bis dato verhindert haben.

Diese Arbeit behandelt verschiedene technologische Aspekte von Lithium-Schwefel Zellen. Einerseits wird der Herstellungsprozess von makroporösen, HIPE–strukturierten (hohe interne Phasen Emulsion) Schwefel-Kohlenstoff Elektroden gezeigt und dessen elektrochemisches Verhalten in der Li-S Zelle getestet. Andererseits wird das Verhalten der negativen Lithium-Metall Elektrode während elektrochemischer Lade- und Entlade-Zyklen untersucht. Abschließend werden praktisch erreichbare Energiedichten in Li-S Zellen diskutiert und der Einfluss verschiedener Batteriekomponenten auf diese untersucht.

Contents

1 Motivation and content

The motivation for the extensive research on new and improved battery technologies can clearly be found in ensuring the growing demand of electric energy for an increasing world population. Referring to International Energy Agency's (IEA) world energy outlook 2014, the world primary energy demand in 2040 will be 37% above the current demand. Considering that conventional energy sources based on high-carbon materials such as coal and oil reach their plateaus by this time, renewable energy gains further importance and the IEA claims that renewable energy sources may account for half of the predicted global increase in energy demand.[1] Batteries will represent a key technology for compensating the fluctuating energy delivery ("peak load levelling") inherent to e.g. wind or solar sources.[2] Besides stationary uses, the increasing demand for batteries in the automotive sector and for portable electronic devices shifts the focus to the development of affordable batteries with high energy densities which e.g. enable reasonable driving ranges at reasonable costs. At this time driving ranges of electric vehicles (EV) are in the order of magnitude of 100 miles for cars available in a price segment of below 40000 € like the VW e-Golf. [3]

The lithium-sulfur (Li-S) battery technology might state a further step towards affordable higher energy density batteries as this battery chemistry promises a more than five-fold theoretical specific energy density of ~2500 Wh/kg (based solely on the mass of active materials, at 2.15 V cell voltage) than current state of the art lithium ion batteries (LIB) such as e.g. $LiCoO_2$/C with 387 Wh/kg (at 3.8 V cell voltage). However, several drawbacks prohibit the use of this technology. Cycle lives and practically obtainable energy densities with currently applied Li-S materials are not yet competitive with LIBs.

This work deals with several aspects of Li-S cells. The manufacturing process of HIPE-structured (high internal phase emulsion) macroporous carbon/sulfur electrodes is presented and their usability in Li-S cells is evaluated. Further, the behaviour of the lithium metal negative electrode during electrochemical charge-discharge sequences is investigated in terms of electrode polarization and surface morphology evolution. Finally, energy density calculations on lab-scale Li-S cells and predictions on energy densities in dependence of several electrode parameters are discussed.

2 Theoretical background

Since the concept of lithium-sulfur (Li-S) battery was introduced by Herbert and Ulam in 1962 [4] and the development of the first cell based on elemental sulfur, metallic lithium electrodes and organic electrolytes by Rao a few years later [5], many research efforts have been devoted to the development of lithium-sulfur batteries. However, poor cycling performance decreased attention for lithium-sulfur technology in the early years. On the other hand, the increased demand for cheap and environmentally friendly energy storage devices, which outperform current lithium ion technology in terms of energy density and costs, has regained the interest in Li-S technology. [6]

As lithium metal combines a low equivalent weight and the most negative potential (-3.04 V vs. standard hydrogen electrode), it is a promising candidate as negative active material and lays the foundation for commercialization of primary lithium metal batteries (e.g. Li-$SOCl_2$). However, serious safety issues arise upon repeated dissolution and deposition of lithium metal in secondary batteries (e.g. creation of lithium dendrites could short-circuit the cell and induce heating and thermal runaway), which prohibit their commercial use. The concept of using Li in its ionic rather than metallic state and the reversible intercalation and extraction of the Li^+-ion into host electrode materials allows to circumvent dendritic lithium metal deposition and related problems. The discovery of reversible carbonaceous intercalation anodes by Besenhard [7] and further development by Mohri et al [8] led to the development of the first commercially available lithium ion batteries (LIB) launched by Sony Corporation in 1991. $LiCoO_2$ (which was developed about 10 years earlier by Goodenough [9]) was applied as cathode material together with non aqueous liquid electrolyte. The batteries showed high average discharge voltages (3.6 V) and high specific energy densities in the range of 120-150 Wh/kg (on cell level). [10] Nowadays lithium ion batteries store about twice as much energy as the first commercial cells and are ten times cheaper. However, they are approaching their limits in terms of specific energy density, as insertion materials are mostly restricted to one electron transfer per formula unit. Improvements of about 30% are imaginable [11] which will be realized by applying advanced cell chemistries with high voltage positive electrodes (e.g. “5 V” positive electrodes such as $LiCoPO_4$ or $LiNi_{0.5}Mn_{1.5}O_4$). On the other hand negative electrodes with higher specific capacities, like lithium metal alloys (Li-Si or Li-Sn) can be applied. By moving from insertion process to conversion process, like it is the case in Li-S cells, specific energy densities in lithium cells can be increased further.[12]

Today's lithium ion batteries realize long cycle life of up to >6000 cycles (service life 20 years) and high energy efficiencies. Their energy densities are in the range of ~250 Wh/kg and predictions claim that a maximum of 300-350 Wh/kg will be reached at 2020. For lithium-sulfur technology 500 Wh/kg are predicted and therefore a doubled energy density of current state of the art LIB.[11]

Figure 1 shows the practical gravimetric and volumetric energy densities of various battery systems.

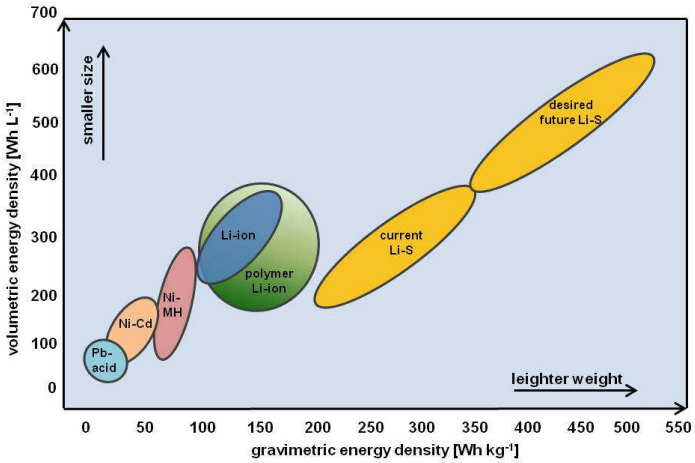

Figure 1: Volumetric and gravimetric energy density of various battery technologies [10][13]

Beyond lithium ion conversion technologies like lithium-sulfur or lithium-air may pave the way to meet future demands and reduce costs and environmental impact. However these technologies are plagued with several drawbacks not yet solved such as capacity fading at sulfur cathode (due to e.g. electrode passivation, polysulfide (PS) dissolution) and lithium degradation (e.g. creation of dendritic, mossy surface, creation of *dead* lithium), lithium related safety concerns and continuous electrolyte consumption (resulting in running dry and restricting cycle life). [14] Despite the interest over lithium-sulfur technology in recent years and enhanced research activities of prestigious groups all over the world, adverse opinions exist whether lithium-sulfur is able to overcome both safety and energy demands of prospective energy requirements. [11]

OXIS Energy LDT, located in Oxfordshire, UK, is currently planning to produce "long life" lithium-sulfur cells with a cycle life of 1500 until 80% DoD (depth of discharge) in high volumes and energy densities of 165 Wh/kg and 220 Wh/kg by mid 2015 and mid 2016 respectively. An "ultra

light" version with high energy density (up to 300 Wh/kg), but restricted cycle life of 100 cycles (80% DoD), is planned for 2016 on large scale production. [15]

An example for successful practical application of lithium-sulfur batteries was made in 2010 when Zephyr 7, a High Altitude Pseudo-Satellite (HAPS) developed by Airbus Defence and Space, was able to conduct a flight about 11 days exclusively powered by solar energy. The implemented lithium-sulfur battery with 350 Wh/kg, designed and assembled by Sion Power Corp. (Tuscon, Arizona), was charged during the day in order to power the unmanned aerial vehicle during night.[16]

2.1 Electrochemical basics

The following basic thermodynamic and kinetic descriptions are based on references [17][6][18][19][20][21]

A basic galvanic element consists of a negative and positive electrode immersed in an electrolyte. The electrode chambers are separated by a porous separator. The electrolyte and separator enable ionic conduction between both electrode chambers, while electronic conduction is solely possible through the closed external circuit. Electron delivering reactions occur spontaneously, with oxidation reaction at the anode generating electrons which flow (in the external circuit) to the cathode where reduction reaction occurs upon discharge. Electron flux between the electrodes is driven by the difference in electrochemical potentials and is accompanied by the corresponding ion flux in the electrolyte for charge equalization. All in all, the galvanic cell facilitates to separate electron and ion flow of a chemical reaction and therefore the conversion of chemical energy into electrical energy.

Faraday's law describes the quantitative relation between generated current and the amount of mass of substrates involved in the reaction at the electrode/electrolyte phase boundary.

$$m = \frac{M * I * t}{z * F} \qquad \textbf{Eq. 1}$$

m = active mass which was transformed
M = molar mass of the active material
z = number of exchanged electrons
I = current flow
t = time of current flow
F = faraday constant, 96485 As/mol

2.1.1 Thermodynamic and kinetic considerations

In general, the chemical potential of electrolyte and electrodes is different and therefore, when immersing a metal electrode into the electrolyte, dissolution or deposition occurs, reaching for chemical equilibrium condition. These processes cause the creation of oppositely charged phases at the electrode/electrolyte interface and are accompanied by the creation of an electrical potential. The electrical double layer prevents further dissolution/deposition after reaching a certain charge between electrode and electrolyte. In summary, the chemical potential μ_i in the inner phase of the electrode is influenced by the electrical potential at the phase boundary, resulting in the electrochemical potential $\tilde{\mu}_i$. When the equilibrium state is reached, the corresponding electrical potential is called galvani-potential.

$$\tilde{\mu}_i = \mu_{i,0} + \boldsymbol{RTlna_i} + \boldsymbol{z_i F \phi_i} \qquad \textbf{Eq. 2}$$

μ_i^o = standard chemical potential in the metal and electrolyte respectively
R = universal gas constant, 8.314 J/(mol*K)
T = temperature
a_i =ionic activity in the various phases
zi = charge of ions dissolved from the metal
F = faraday constant, 96485 As/mol
ϕ_i = electrical potential in the metal and electrolyte respectively

It is impossible to measure the galvani potential directly, but the difference of two galvanic potentials can be determined. For this reason, the standard hydrogen electrode (SHE) is applied as reference system (which is set arbitrarily to 0V by convention) and the obtained potential differences of materials against SHE are referred to as standard electrode potentials E_{00}.

$$\boldsymbol{E_{00} = \Delta\phi_{metal} - \Delta\phi_{SHE}} \qquad \textbf{Eq. 3}$$

In equilibrium state (no net current flow) the equilibrium cell voltage (ΔE_0) under standard conditions (ΔE_{00}) of a galvanic cell can either be determined by measuring the difference in electrochemical potential between positive and negative electrode (half cells) or it can be calculated from the reaction free energy ΔG. In general, the equilibrium cell voltage can be obtained by following equation

$$\Delta E_{00} = E_{c,positive\ electrode} - E_{a,negative\ electrode} \quad \textbf{Eq. 4}$$

The fundamental thermodynamic equation is the Gibbs Helmholtz equation,

$$\Delta G = \Delta H - T\Delta S \quad \textbf{Eq. 5}$$

ΔG = reaction free energy
ΔH = reaction enthalpy
ΔS = entropy
T = temperature

The Gibbs-Helmholtz equation states that the reaction free energy ΔG of a reaction, which is utilizable as useful work, equals ΔH-TΔS, the total energy released by the electrochemical reaction ΔH, minus or plus TΔS, the (reversible) amount of heat generated or utilized for decreasing or increasing the entropy of the reacting materials.

The maximum amount of usable electrical energy ΔG in an electrochemical reaction equals the amount of free energy of a mere chemical reaction. For reversible electrochemical reactions in equilibrium (at zero net current flow and no concentration gradient in the electrolyte), ΔG can be related to the equilibrium cell voltage and can be calculated by following equation

$$\Delta G_0 = -n * F * \Delta E_{00} \quad \textbf{Eq. 6}$$

ΔG = reaction free energy
nF = amount of charge which is transferred per mole
ΔE_{00} = equilibrium cell voltage

In case of a galvanic cell (ΔG<0) spontaneous reactions occur, while in case of electrolysis (ΔG>0) energy has to be supplied to force an electrochemical reaction.

The concentration dependence (and the dependence of conditions other than standard conditions) of the equilibrium cell voltage can be described by applying the Nernst equation (Eq. 9). It can be derived from the previously discussed equations (Eq. 2 to Eq. 6) in consideration of chemical thermodynamics, meaning the sum of chemical potentials μ_i of involved products and reactants which equals ΔG and can be set as

$$\Delta G_0 = \sum v_i * \mu_i \qquad \textbf{Eq. 7}$$

ΔG = reaction free energy
v_i = stoichiometric factors
μi = chemical potential

The chemical potential in a half cell is concentration dependent

$$\mu_i = \mu_{i,0} + R * T * ln a_i \qquad \textbf{Eq. 8}$$

$\mu_{i,0}$ = standard chemical potential of compound which react at the electrode
R = universal gas constant, 8.314 J/(mol*K)
T = temperature
a_i = activity of the compounds which are reacting at the electrode

Finally the electrochemical equilibrium potentials of the half cells are expressed by the Nernst equation

$$E_0 = E_{00} + \frac{R * T}{n * F} * \sum v_i * ln\, a \qquad \textbf{Eq. 9}$$

And for a metal-ion electrode it can be written as following

$$E_0 = E_{00} + \frac{R * T}{z * F} * ln \frac{a_{ox}}{a_{red}} \qquad \textbf{Eq. 10}$$

When power is drawn from practical systems, the terminal voltage differs from theoretically determined values at equilibrium. The deviations occur due to the ohmic voltage drop and polarizations (overpotentials) (cf. Figure 2). Consequently, the voltages that are required for the electrode reactions and hence for electron flux to occur are shifted towards lower and higher values during discharge and charge respectively. The maximum electric energy (=ΔG) stored or delivered by the electrochemical couple is diminished by polarization processes and the related energy amount is converted to heat.

During external load, the cell voltage can be described with the following equation:

$$E = E_0 - [\eta_{ct,a} + \eta_{c,a}] - [\eta_{ct,c} + \eta_{c,c}] - iR_i = iR \qquad \textbf{Eq. 11}$$

E_0 = open circuit potential (OCV)
$\eta_{ct,a/c}$ = activation polarization (=charge transfer polarization) at anode and cathode
$\eta_{c,a/c}$= concentration polarization at anode and cathode
i = current load
R_i = internal resistance of the cell

Figure 2 shows the influence of different types of polarizations on a typical discharge voltage curve of a battery. The dashed line indicates the voltage behaviour of an ideal cell with maximum electric energy (=ΔG) which would appear as rectangle, and an abruptly dropping voltage after electrode reactions are exhausted.

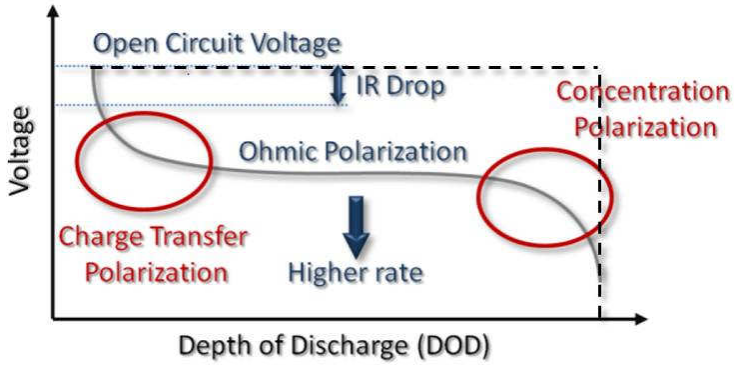

Figure 2: Schematic drawing of discharge curve showing influence of polarization [22]

The determination of single impacts of different polarizations on cell voltage is difficult and partly depends on the physical structure of the electrodes. Therefore only a qualitative description will be given.

- Charge transfer overpotential concerns the kinetic hindrance of charge transfer through the phase-boundary electrode/electrolyte. The Butler-Volmer equation describes mathematical relation between overpotential and current at the electrode (when mass transfer limitations are negligible and kinetic is limited solely by charge transfer resistance). Fast electrode reactions and porous electrodes with high surface (which offer more reaction sites at the phase boundary and reduce local current density) result in lower charge transfer polarization.

- Diffusion overpotential (concentration overpotential) is caused by limited mass transport of reactants in the electrolyte, causing depletion of reacting species at the electrodes. It is more distinct at higher current loads. Electrodes and separators with suitable pore structures and thicknesses, sufficient reactant concentration and ionically well conducting electrolytes reduce diffusion overpotential.
- Reaction overpotential has its origin by rate limited reactions, occurring prior or after the electrochemical reactions as such, like adsorption and desorption.
- Crystallization overpotential can be observed when the intercalation of metal ions into their lattice is kinetically prevented. This is especially important for lithium deposition upon charge in lithium-sulfur cells.
- Ohmic polarization has its origin in the internal resistance of the cell, which arises from electrolyte solution, materials (electrodes, current collectors, terminals) as well as contact resistance between the different cell components. This type of polarization shows linear dependence on current load and therefore follows the Ohm's law.

2.1.2 Battery characteristics: glossary

Terminal voltage U [V]: difference in voltages between positive and negative electrode during charge and discharge.
Open circuit voltage (OCV) [V]: difference in voltages between positive and negative electrode at zero current load.

Specific capacity [Ah/kg]: total amount of charge Q that can be stored or delivered per unit mass, it can be obtained by integration of current flow (i) over time (t).

$$\boldsymbol{Q = \int i\, dt} \qquad \textbf{Eq. 12}$$

Coulombic efficiency (CE) [%]:ratio between the charge obtained during discharge of the cell ($Q_{discharge}$) and the required charge for charging the cell (Q_{charge}):

$$\boldsymbol{CE = \frac{Q_{discharge}}{Q_{charge}} * 100} \qquad \textbf{Eq. 13}$$

Volumetric [Wh/l] and specific energy density [Wh/kg]: energy per unit volume or unit mass of the cell can be derived from the integration of the product of current (i) and voltage (U) over time:

$$E = \int U * i \, dt \qquad \textbf{Eq. 14}$$

Energy efficiency (EE) [%]: ratio between energy required for charging the cell and energy obtained from discharging the cell.

$$EE = CE * \frac{U_{discharge}}{U_{charge}} * 100 \qquad \textbf{Eq. 15}$$

Power [W]: the power that is delivered at a certain time can be obtained by following equation:

$$P = U * i \qquad \textbf{Eq. 16}$$

Relating the power to unit mass or unit volume gives the power density [W/l] and specific power density [W/kg] respectively.

Cycle life refers to the number of cycles that can be performed until a certain limit of capacity (80%) of the cell is reached. Service life refers to the time that a battery can be used before its capacity drops below a certain limit of capacity.

2.2 The lithium-sulfur (Li-S) System

2.2.1 Sulfur basics

In nature, sulfur is occurring as elemental sulfur, as well as in bonded state (H_2S, SO_2 and FeS_2). About 40%, or 40 Mio tons, of the world wide yearly sulfur production is based on the exploitation of natural deposits of elemental sulfur and 60% are obtained from H_2S in mineral oil and natural gas or in the form of SO_2 and FeS_2. Worldwide reserves of sulfur are estimated with 25 Megatons. Due to high abundance and easy exploitation, sulfur is a cheap material.[23]

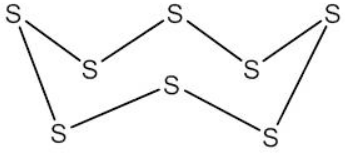

At ambient temperatures solid sulfur occurs as cyclo-octasulfur in rhombic modification ("α-sulfur"), which is the thermodynamically stable composition. This modification has a density of 2.06 g/cm^3. At 95.5°C α-S_8 is converted to β-S_8, the monoclinic modification, which melts at 119.6°C. Liquid sulfur has a viscosity minimum at 155°C enabling the preparation of composite cathode materials via sulfur melt infiltration into host materials. At 159°C the viscosity is abruptly

increasing, when the chemical equilibrium between low and high molecular sulfur molecules, which are present in molten sulfur, is shifted towards high molecular linear sulfur molecule μ-S_x. [23] The electrical conductivity of sulfur is as low as $5*10^{-30}$ S/cm at room temperature. [24]

2.2.2 Principle of Li-S batteries

In lithium-sulfur batteries sulfur serves as the positive and metallic lithium as the negative active material. Sulfur exhibits high theoretical capacity of 1672 mAh/g and a moderate average discharge voltage of 2.15 V vs. Li/Li^+. Thus, theoretical energy densities of up to 2500 Wh/kg and 2800 Wh/l can be obtained.

The mechanism of reversible energy storage in lithium-sulfur system fundamentally differs from LIBs. In comparison, in LIBs electrochemical redox reactions are based on reversible intercalation of lithium ions into a host material, while the redox reactions of sulfur are based on reversible chemical conversion.[25] Although the initial (elemental sulfur) and final state (lithium sulfide) of positive active mass is solid, the intermediate reaction species are soluble in polar aprotic electrolyte media, and therefore the solution based reaction chemistry can be discussed as liquid cathode.[26]

The basic principle is depicted in Figure 3.

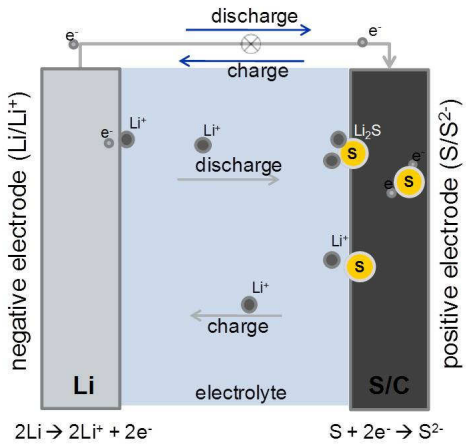

Figure 3: Schematic principle of a Li-S battery showing negative electrode (lithium metal anode) and positive electrode (sulfur/carbon composite cathode) and liquid organic electrolyte, redrawn from [27]

Upon discharge of the battery, Li^+-ions dissolve into the electrolyte and migrate through the separator to the cathode and react with sulfur to form polysulfides. The reduction of sulfur

involves breaking of S-S bonds and the formation of polysulfides of different chain lengths. Upon charge these reactions occur in the reverse direction. [27] The overall reaction can be summarized by following equation:

$$16Li + S_8 \leftrightarrow Li_2S \qquad \textbf{Eq. 17}$$

2.2.3 Discharge behaviour of Li-S

While the overall reaction of Li-S battery seems rather simple, a closer look reveals the complex nature of electrode reactions. The main reactions are summarized in the following section, while the exact mechanism is yet not fully clarified and controversially discussed in literature because disproportionation and dissociation reactions contribute to further complexity. Figure 4 depicts a typical charge-discharge voltage profile for the first discharge of a Li-S cell containing liquid ether based electrolyte with $LiNO_3$. The different regions of the curve are assigned to the main reaction steps. The voltage profile and exact reaction mechanism further depends on the electrolyte composition. [28] [29] [30]

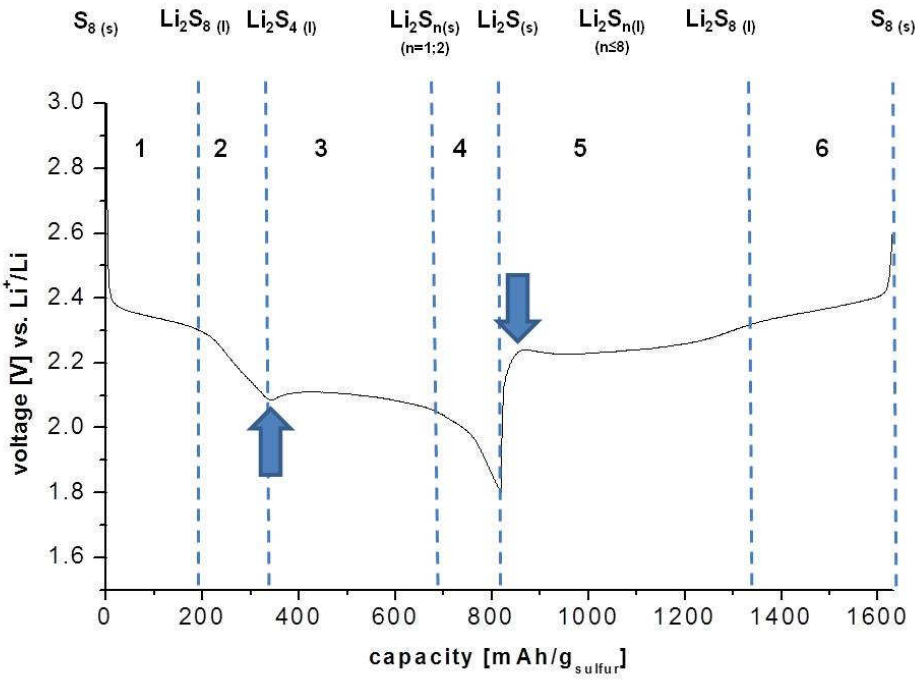

Figure 4: Typical charge discharge curve of a practical Li-S battery with a sulfur utilization of ~50%, modified from [31], source measurement: author

In general, the discharge reaction of sulfur occurs in a multistep reduction and a typical reduction can be divided into four regions. The upper voltage plateau at ~2.3 V-2.4 V (cf. region 1, Figure 4) is ascribed to the formation of long chain lithium polysulfide Li_2S_8 and is accompanied by a phase change from solid S_8 to soluble Li_2S_8 (Eq. 18). [31] The latter is well soluble in the electrolyte and furthermore tends to disproportionate, resulting in the formation of polysulfides (PS) with shorter chain length and again elemental sulfur (cf. Eq. 27). [26]

$$2Li^+ + 2e^- + S_8 \leftrightarrow Li_2S_8 \qquad \textbf{Eq. 18}$$

A steep slope in the discharge curve (region 2, Figure 4) has its origin in a series of reductions resulting in the formation of short chain PS Li_2S_4. All involved intermediate species are soluble in the liquid electrolyte (Eq. 19). The viscosity of the electrolyte reaches a maximum at the end of region 2, when PS with moderate chain length are dissolved. This results in a small peak in the discharge curve (marked with an arrow) due to higher overpotential for subsequent reduction. The change in the redox potential is caused by the relatively increased negative charge at sulfur atoms as the chain length decreases. [31] At the end of region 2, *0.5* electrons per sulfur atom are accepted.

$$Li_2S_8 + 2Li^+ + 2e^- \leftrightarrow 2Li_2S_4 \qquad \textbf{Eq. 19}$$

The second voltage plateau at 1.9-2.1 V (cf. region 3, Figure 4) refers to the reduction of dissolved medium chain length PS species Li_2S_4 to Li_2S_2 and Li_2S, which are insoluble in the electrolyte and precipitate at the electrode surface. Upon nucleation of PS species, the concentration of dissolved PS decreases and the overpotential at the beginning of region 3 is diminished as a consequence.[32] Considering that the complete reduction from elemental sulfur to Li_2S involves 2 electrons, a major contribution of capacity arises in this region, as it comes with the change in the formal charge of sulfur from $S^{-0.5}$ to S^{-2}. [31]

$$Li_2S_4 + 2Li^+ + 2e^- \leftrightarrow 2Li_2S_2 \qquad \textbf{Eq. 20}$$

$$Li_2S_4 + 6Li^+ + 6e^- \leftrightarrow 4Li_2S \qquad \textbf{Eq. 21}$$

A steep slope at the end of discharge (cf. region 4, Figure 4) marks the further reduction from Li_2S_2 to Li_2S, which is kinetically hindered as the two species are solids and additionally non-conductive. The reactions in region 3 compete with each other and influence the shape of the curve in region 4, with a steeper slope if Eq. 21 is predominant over Eq. 20.[31]

$$Li_2S_2 + 2Li^+ + e^- \leftrightarrow Li_2S \qquad \textbf{Eq. 22}$$

It is demonstrated by Schneider et al. [29] that solvent polarity (DMSO and DMSO/DOL vs. DME/DOL) influences the discharge voltages in Li-S system significantly. The free solvation energy of ions contributes to the reaction enthalpy and therefore to ΔG. Solvents of higher polarity like DMSO raise the voltage of the upper discharge plateau (region 1 in Figure 4) due to increased solvation energy (dissolution of PS species) in comparison to ether based solvents. However, when low order PS species start to precipitate at the beginning of the second discharge voltage plateau (region 3 in Figure 4), a corresponding decrease in voltage occurs due to de-solvation energy (in comparison to DME/DOL electrolyte). This fact results in an overall lower energy release, because the major contribution of discharge capacity is generated at the lower voltage plateau.

2.2.4 Charge behaviour of Li-S

The cell polarization at the beginning of oxidation may be explained by the solid and non-conductive layer of Li_2S_2 and Li_2S which is formed at the end of discharge. After being oxidized to soluble PS species cell polarization decreases, as can be seen in the voltage profile (indicated by the second arrow in Figure 4). In general the oxidation process shows two voltage plateaus.[31] The charging process consists again of a series of complex reactions involving charge transfer processes as well as chemical reactions between PS of different chain lengths. At the lower charge voltage plateau at ~2.3 V, Li_2S and short chain PS species are stepwise oxidized. Firstly, medium chain length PS are generated, which are soluble in the electrolyte (cf. Eq. 23). Kolosnitsyn and Karaseva have suggested [26] that medium-chain length PS species are oxidized to long chain PS at the lower charge voltage plateau (cf. Region 5, Figure 4).

$$mLi_2S_k \leftrightarrow gLi_2S_n + 2Li^+ + 2e^- \qquad \textbf{Eq. 23}$$

with mk=gn

These PS species in turn chemically react with insoluble Li_2S and Li_2S_2 (Eq. 24 and Eq. 25) until the latter are completely consumed. Again medium chain PS are created, which are subsequently oxidized to long chain species (region 5).

$$Li_2S + Li_2S_n \leftrightarrow Li_2S_k + Li_2S_{n-k+1} \quad \textbf{Eq. 24}$$

$$Li_2S_2 + Li_2S_n \leftrightarrow Li_2S_k + Li_2S_{n-k+2} \quad \textbf{Eq. 25}$$

The mentioned reactions facilitate the electrochemical reversibility of electronically insulating solid Li_2S_2 and Li_2S. Subsequently, long chain PS are oxidized concerted to elemental sulfur at the second voltage plateau at 2.4 V-2.6 V (cf. region 6, Figure 4).[26][33]

$$Li_2S_8 \leftrightarrow S_8 + 2Li^+ + e^- \quad \textbf{Eq. 26}$$

2.2.5 Disproportionation of PS

In general PS disproportionation reactions occur besides the electrochemical reactions, which do not come along with the generation of electrons and thus are less favourable.

$$Li_2S_x \leftrightarrow Li_2S_y + \frac{(x-y)}{8}S_8 \quad \textbf{Eq. 27}$$

The chemical equilibrium of Eq. 27 is shifted to the left, if temperature and PS concentration is increasing. Poorly soluble short chain PS and S_8 tend to precipitate when they are generated via disproportionation. If this reaction occurs in the separator or in dead corners of the cell capacity fading will be enhanced. Properly adjusted electrolyte/sulfur ratio may decrease the impact of disproportionation and minimizes the unfavoured precipitation. [34]

2.2.6 PS shuttle phenomenon

A major challenge in Li-S cells is the polysulfide shuttle phenomenon. Due to concentration gradient, well soluble long chain PS species diffuse through the liquid electrolyte and get chemically (Eq. 29) or electrochemically (Eq. 28) reduced at the electron-rich lithium anode. [31] [35]

$$(n-1)Li_2S + 2Li^+ + 2e^- \leftrightarrow nLi_2S_{n-1} \qquad \textbf{Eq. 28}$$

$$(n-1)Li_2S + 2Li \leftrightarrow nLi_2S_{n-1} \qquad \textbf{Eq. 29}$$

Shorter chain PS either precipitate directly at the lithium metal electrode surface and increase polarization causing capacity loss, or diffuse back to the cathode (again driven by concentration gradient), where they react with sulfur species or get re-oxidized upon charge and reduce coulombic efficiency. [31]

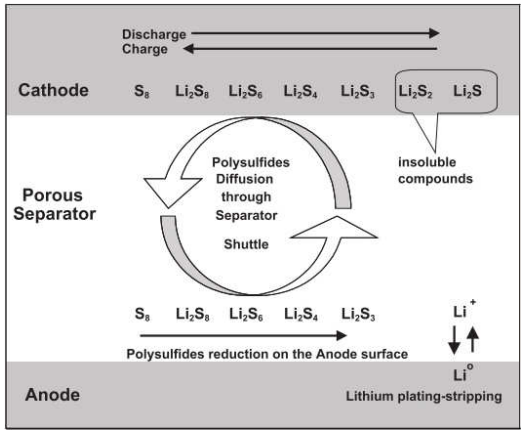

Figure 5: Schematic drawing of PS shuttle phenomenon [36]

If this reaction is not prevented by protecting the lithium metal electrode, the continuous consumption of electrons during charge decreases coulombic efficiency and prevents the cell from reaching the fully charged state. In this case, the cell voltage does not rise above ~2.3-2.4 V (cf. Figure 11, p.37) and heat is generated instead. [36] Mikhaylik and Akridge [37] conducted a quantitative study of the PS shuttle phenomenon. For understanding the effect of PS shuttle on the charge profile, the charge-shuttle factor (f_C) is defined:

$$\frac{k_s q_H [S_{total}]}{I_C} = f_C \qquad \textbf{Eq. 30}$$

I_C = charge current
q_H = specific capacity of sulfur in the high voltage plateau at 2.3-2.4 V
k_S = shuttle constant
$[S_{total}]$ = total amount of sulfur present in the cell

It is shown that if f_C is <1, the cell could be fully charged, and the amount of overcharge needed to recreate elemental sulfur is higher if values are near to 1. On the contrary if f_C>1, the cell never reaches fully charged state and shows voltage levelling, as the shuttle current exceeds or equals the charge current. By increasing the charge current the value of f_C is decreasing, according to Eq. 30 and a steep voltage increase occurs at the end of charge profile.

On the other hand, the electrolyte composition and conducting salt concentrations influence the shuttle constant. Higher salt concentrations, for instance, decrease the shuttle constant and lithium corrosion. This is shown for electrolytes with 0.5 M and 2.5 M concentration and possible explanations may be found in the influence of salt concentration on electrolyte viscosity, PS solubility and anode/electrolyte interface (and reaction rate of PS with Li). The repeated reaction of polysulfides at the lithium metal anode causes self-heating, which in turn enhance the reaction of PS and Li and the shuttle constant, as shown in Eq. 31. [37]

$$k_S(T) = k(T_0)\exp\left[-\frac{A}{R}\left(\frac{1}{T} - \frac{1}{T_0}\right)\right] \qquad \textbf{Eq. 31}$$

k_s = shuttle constant
A = activation energy
R = gas constant, 8.314 J/(mol*K)
T = temperature at the end of charge
T_0 = temperature at beginning of charge

Increased shuttle phenomenon is observed in cells with inhibited heat dissipation. Furthermore, a steady state condition (shuttle current=charge current) with constant temperature can be reached and prevents the cell from overcharge. [37] [6]
In general, any direct reaction of PS at lithium negative electrode (during charge or discharge) is not accompanied by the generation of usable energy and is not favourable. During storage of cycled cells, the high mobility and reactivity of lithium and high order polysulfides [38] [39] causes self-discharge. The available capacity at the higher plateau declines, while reactions at

the lower plateau are not influenced even after several weeks. At higher temperature the increased shuttle constant leads to higher self discharge.[37] For diminution of the self discharge process the electrolyte additive $LiNO_3$ is applied in practical cells, which suppresses the PS shuttle (see chapter 2.5.1.1, p.35).

2.2.7 Capacity fading

Capacity fading in Li-S has multiple causes. The dissolution of PS species into the bulk electrolyte and the subsequent diffusion to and direct reaction at the lithium metal anode results in major capacity loss. If the solid reduction products Li_2S and Li_2S_2 precipitate in layers with insufficient electronic connection (at both electrodes) they may not be available for re-oxidation in the following charging cycle. Electrically and ionically isolating layers on the surface of the cathode may additionally block further Li^+-ion migration/diffusion into deeper electrode regions and prevent sulfur utilization in some regions of the electrode. The passivation layer may further cause increased cell polarization. As mentioned (cf. 2.2.5, p.15), S_8 and insoluble short chain Li_2S_2 and Li_2S species may precipitate due to disproportionation reaction in the separator and in dead corners of the cell and are no longer available for electrochemical reaction at the electrode. Although electrically isolated Li_2S and S_8 may be (re-)activated by chemical reactions with long chain polysulfides, they cause a major contribution to capacity fading in Li-S cells. [40][33][34]
Phase changes of the active material (solid-liquid) alter the initial active mass distribution and structure of the positive electrode during a full cycle. In general the creation of Li_2S (1.67 g/cm^3) is accompanied by a volume expansion in comparison to the initial elemental sulfur (2.06 g/cm^3) which causes mechanical stress inside the electrode. This can result in a deteriorated electronic connection (electron percolation) within the electrode and a deteriorated connection to the current collector. Increased cathode thickness and discharge rates result in decreased sulfur utilization. The diffusion rate of PS and Li^+-ions is more hindered and as a consequence reduction to Li_2S predominantly occurs in layers near to the electrode/electrolyte interphase. Slow reaction kinetics of solid reduction products influence rate capability from the second discharge plateau onwards. On the contrary, the first plateau is less affected by the discharge rate since involved species are dissolved in the electrolyte and the diffusion rate towards the carbon surface determines the rate capability. [35] [41]

2.3 Sulfur electrode

In general porous electrodes with large surface areas are applied in most types of batteries, in order to reduce activation and concentration polarizations during electrochemical reaction. Due to this porous structure (different pore sizes and tortuosity), the mass transfer and consequently, the current density distribution vary at different locations of the electrode.[17]

For the preparation of the positive electrode in lithium-sulfur batteries, further facts have to be taken into account.[6]

- Structural integrity has to be preserved during physical phase changes and volume expansion upon transformation to solid Li_2S (in comparison to initial incorporated sulfur) needs to be compensated
- Fast electron and ionic transfer to electronically and ionically insulating sulfur reaction species has to be ensured also to obtain high sulfur utilization
- Pore clogging through re-deposited solid active material species should be prevented to maintain lithium-ion transport to deeper cathode regions
- Confinement of soluble reduction species with high ion mobility to prevent dissolution into the bulk electrolyte

Typically electrodes are prepared by slurry technique, meaning casting dispersions of composite materials, conducting agents and polymer binders (e.g. polyvinylidene fluoride (PVdF), sodium carboxymethylcellulose/ styrene butadiene rubber (CMC/SBR), polyethylene oxide (PEO), polytetrafluoroethylene (PTFE)) in appropriate solvents like N-methyl-2-pyrrolidone (NMP), water or acetonitrile (ACN) onto current collectors (mostly aluminium or carbon coated aluminium foils). Due to the insulating nature of sulfur, conducting additives are applied in high ratios up to 50-60 w%. Homogeneous sulfur distribution is mostly achieved either by simple mechanical mixing or combined with sulfur melt infiltration or infiltration of sulfur in the dissolved/dispersed state with an optional heating step. Binders are used in ratios between 5-10 w% to provide an adequate structural integrity of the electrode layer and adhesion to the current collector. [13]

A wide variety of sulfur cathode design approaches can be found in literature, meeting the above stated requirements to greater or lesser extent. Different carbon materials are applied as sulfur hosts such as core-shell particles, multi walled carbon nano tubes (MWCNT) or hierarchically structured porous carbons. Further, several cathode additives are applied for retarding the polysulfide diffusion. On the other hand organic polymer sulfur composites are investigated in

literature. In terms of electrode fabrication, a simpler yet effective approach is the application of commercially available conductive carbons and properly chosen binder materials.[42] The preparation techniques of advanced materials can involve multiple steps increasing manufacturing costs and decreasing industrial relevance, leading to reconsideration of advanced electrode materials. Moreover, the practicability of different types of electrodes strongly depends on the amount of inactive components and utilizable sulfur content in the electrodes. In general, the comparison of different approaches and the resulting electrochemical performances is difficult, as cathode and cell performance is significantly influenced by various factors like sulfur ratio and absolute sulfur loading, electrolyte chemistry and volume or binder material.[43][44] In the following section selected examples are given for various concepts.

2.3.1 Carbon frameworks for sulfur electrodes

The concept of highly ordered mesoporous carbons (CMK-3) was introduced by Nazar et al. [45] in 2009. Hollow carbon rods (6 nm outer diameter) stretched by carbon microfibers generating channel voids (3-4 nm), are melt infiltrated with sulfur (Figure 6a). In order to gain full advantage of the structure, the amount of sulfur is adjusted carefully with regard to the pore volume of 2.1 cm^3/g. Some micropores in the carbon walls are not filled with sulfur, facilitating electrolyte access and empty volumes accommodating volume changes upon creation of Li_2S. The framework structure retards diffusion of PS into the bulk electrolyte and capacity is further improved by polyethylene glycol (PEG) coating. The beneficial effect is attributed to retarded diffusion of polysulfides into the bulk electrolyte by creating a preferential hydrophilic surrounding for polysulfides inside the carbon structure. The function of PEG coating will be addressed in 2.3.3 (p.24). A specific sulfur capacity of about 1100 mAh/g after 20 cycles can be obtained with these electrodes (83% capacity retention at 168 mA/g and 70 w% sulfur in the composite and ~59 w% in the electrode loading).

Hierarchically structured, bimodal micro-mesoporous carbons as sulfur hosts were firstly investigated by Liang et al.[24]. Micropores (<2nm) and mesopores (>7.3nm) are combined and show a synergetic effect of large surface area and large pore volume (cf. Figure 6 b). The structure facilitates electron transport and keeps polysulfides within the carbon host and thus ensures mass transport and high ionic conductivity inside the composite material respectively. Further development has led to spherical particles and porous hollow carbon spheres with bimodal pore distribution [46] [47]. In addition to the synergetic effects described above, Archer's group [47] has figured out that the confinement of sulfur in the mesopores as well as inside the

voids of the partially graphitic hollow carbon spheres (~650 m^2/g and 3 nm average pore diameter and ~150 nm voids (Figure 6 c)) results in extended cycle life and high rate capabilities with reversible specific sulfur capacities of 974 mAh/g (91% capacity retention and 94% CE after 100 cycles at 850 mA/g and 70 w% sulfur in the composite and 65 w% in the electrode loading). However, vapour phase diffusion method is applied for sulfur filling, which is impractical at large scale level, as stated by Nazar et al.. [46]

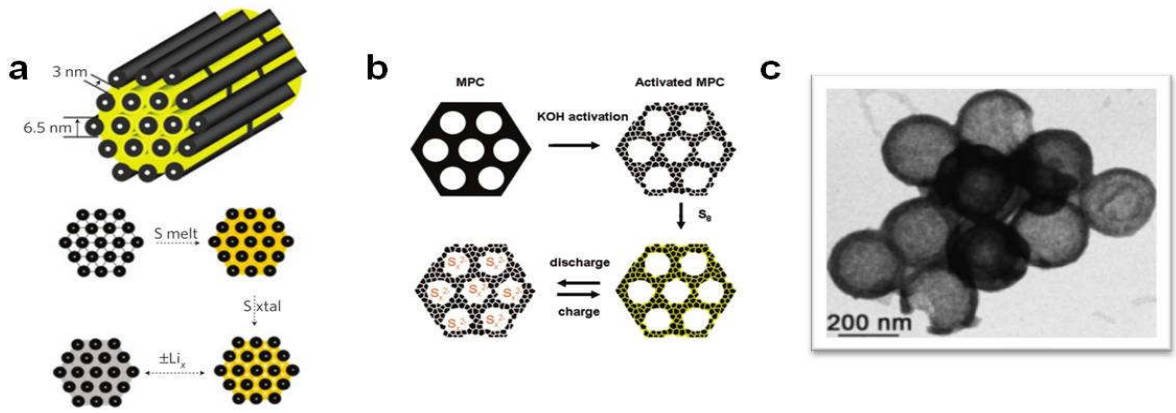

Figure 6: (a) schematic drawing of CMK-3/S [45], (b) schematic drawing of bimodal activated C/S [24], (c) TEM image of mesoporous hollow carbon spheres with S [47]

Graphene increases sulfur utilization if well dispersed on sulfur particles [48] but does not confine soluble PS species and therefore does not enhance capacity retention. In an approach by Cui et al. [49] PEG coated sulfur particles are wrapped with graphene oxide sheets and carbon black nanoparticles (Figure 7a) resulting in electrodes with ~600 mAh/g based on mass of sulfur after 100 cycles (80% capacity retention) at 0.2 C and 70 w% sulfur ratio in the composite (and 56 w% in the electrode loading). The good cycling behaviour is attributed to the wrapping, which compensates volume expansion during cycling and provides permanent electrical contact to sulfur particles beside the beneficial effect of the PEG coating. The insertion of oxygen [50] and nitrogen [51] functional groups in graphene enhances interaction with polysulfides and increases retention of soluble species at the positive electrode. The latter approach results in specific sulfur capacities of ~350 mAh/g after 2000 cycles (at 2 C and 60 w%S in the electrode loading) corresponding to a capacity decay rate of 0.028% per cycle.

Multi-wall carbon nanotubes (MWCNT) are used as electrode component in lithium ion batteries to increase rate capability and to stabilize the electrode structure. In lithium-sulfur batteries,

Manthiram et al. [52] has used a free standing flexible MWCNT film covered with sulfur, which shows high rate capability and capacity without the use of any binder and metal current collector. The electron conductive pathways enhance rate capability and the self-weaving arrangement of MWCNTs compensates volume changes. With a sulfur loading of 40 w% in the whole electrode specific sulfur capacities of 915 mAh/g (1 C) and 650 mAh/g (3 C) after 100 cycles are obtained. Scalable synthesis at low production costs of MWCNTs and no need of binder increase the practical relevance of this approach, while higher sulfur loadings might be realized by combining additional conductive materials.

Aiming at high sulfur loads and effortless production excluding any binder materials, Manthiram et al. [53] have further investigated a layered positive electrode by alternating layers of CO_2 activated carbon nanofiber and elemental sulfur (cf. Figure 7 b). Sulfur loadings up to 11.4 mg/cm^2 show a high capacity of 650 mAh/g after 100 cycles (at 0.2 C and 56 w% sulfur content in the whole electrode). The applied material (carbon fibers of 100 nm diameter) shows a moderate surface area of 714 m^2/g and a pore volume of 1.06 m^3/g. The resulting layered electrodes consist of cheap materials and an effortless production process enhances commercial relevance. Once more the results demonstrate that initial homogeneous mixing of sulfur and carbon is not necessary for achieving good electrochemical behavior, as the active mass distribution is rearranged by continuous dissolution and precipitation reactions during cycling, which is discussed in further detail by Zhang.[54]

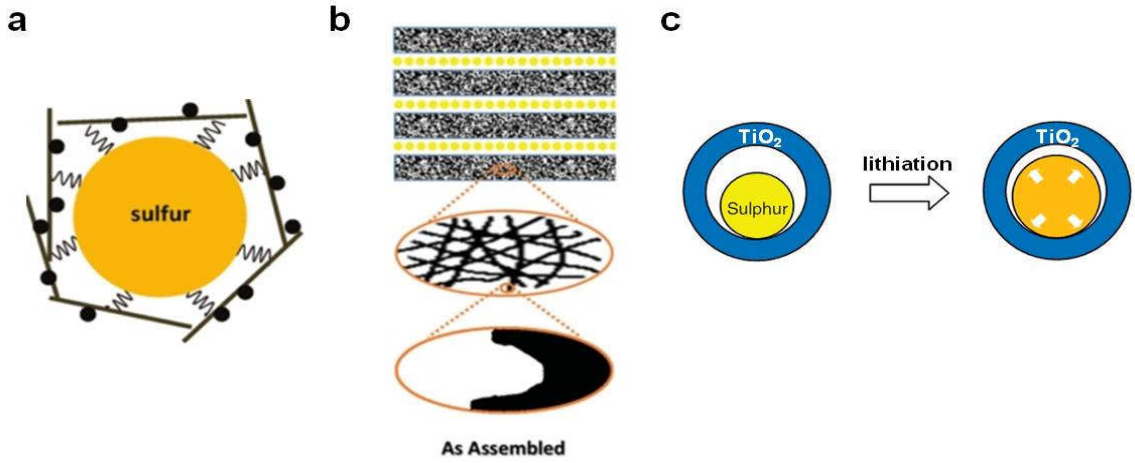

Figure 7: (a) PEG/Super P/graphene wrapped sulfur particle [49], (b) layered sulfur/activated carbon nanofiber as assembled before in situ sulfur redistribution [53], (c) Sulfur-TiO_2 yolk-shell composite [55]

2.3.2 Polymer-sulfur composites, electrode additives

The utilization of electronically conducting polymers for binding sulfur directly as part of the polymer framework or for serving as a host of elemental sulfur in the pores of the polymer, presents another strategy to reduce dissolution of reaction species out of the positive electrode volume. Possible materials are e.g. polyaniline (PA) [56] or polyacrylonitrile (PAN) sulfur composites with the latter being extensively investigated in literature. Applying e.g. PAN coated MWCNT sulfur composites specific sulfur capacities of up to ~590 mAh/g after 50 cycles (0.1 C and 85% capacity retention) are obtained. However, the practicability of these materials is limited due to low sulfur ratios applied in the composites. E.g. 48 w% sulfur in pPAN-S-MWCNT composite corresponding to ~38 w% of S in the electrode are applied to obtain the beneficial effect on cycling stability. At higher sulfur ratios of 63 w% in the composite, dissociated sulfur is created and dissolves into the electrolyte accompanied by capacity fading. Further, low average discharge voltages are obtained, which are as low as 1.8 V vs. Li/Li^+ in case of the discussed example. [57]

Tailoring polysulfides' adsorptivity by applying metal oxides as sulfur host or additive materials is a reasonable approach to enhance cycle life of sulfur electrodes. [58][59] Besides high adsorptivity, a high electronic conductivity, high accessible surface area and tailored pore volume to host sulfur has to be met. Different oxide and carbonaceous materials have been screened. [60] Oxide materials like MnO_2 nanosheets, graphene oxide (GO) and mesoporous TiO_2 show highest adsorptivity among the investigated materials and result in higher capacity retention after 100 cycles than carbonaceous materials such as Super-P carbon black. Polar surfaces interact with PS species and decrease the diffusion of PS out of the electrode. Sulfur-TiO_2 yolk shell composites which combine the beneficial aspects of mesoporous TiO_2's ability to bind polysulfide anions and offering void space to accommodate volume expansion are developed by Cui's group (Figure 7c). [55] After 1000 cycles a specific sulfur capacity of ~700 mAh/g is achieved (at 0.5 C and 71 w% in the composite resulting in 53 w%S in the electrode, with an electrode mass loading of 0.4-0.6 mg/cm^2) corresponding to a capacity decay of 0.033% per cycle. Sulfur/MnO_2-nanosheet composite materials [61] exhibit specific sulfur capacities of ~250 mAh/g after 2000 cycles (at 2 C and 75 w%S in the composite and ~56 w% in the electrode) with a capacity decay rate of 0.036% per cycle. The mechanism of polysulfide retention is identified to occur via the generation of thiosulfate groups on the surface of the host material (e.g. TiO_2 or GO). These subsequently catenate soluble high order polysulfides to form polythionates, which transform into insoluble short chain polysulfides upon discharge.

2.3.3 Binders and separators

The above stated theory for the performance improvement of PEG coated carbon sulfur materials (cf. 2.3.1, p.20) is further investigated by Lacey et al. [62] by studying the effect of PEO as binder and coating and PEG as electrolyte additive. It is figured out that swelling and dissolution of PEO modifies the electrolyte composition. The observed improvement of electrochemical performance in PEG coated carbon/sulfur composites is therefore ascribed to increased solubility of short chain PS and reversibility in electrolytes with long chain glymes (cf. chapter 2.5.1. p.33). Cathode passivation is suppressed as indicated by a flat and long discharge characteristic at the second discharge plateau (increased capacity) and a reduced or even eliminated polarization at beginning of charge.

In general the binder should ensure and preserve the structural integrity of the electrode during cycling and facilitate electronic and ionic transport in the electrode by creating good interface properties between conducting additives, active mass and current collector.[6] In Li-S systems volume changes have to be buffered and PS diffusion may be retained by choosing binder materials properly.[63]

The investigation of the effect of PEO and PVdF as binder and a mixture of CMC:SBR on the electrochemical behaviour of Li-S cells reveals a superior performance of CMC:SBR sulphur electrodes. [64] Electrodes exhibit lower polarization of the second voltage plateau during cycling and higher capacity. Lower impedance of the CMC:SBR containing electrodes before discharge and lower charge transfer resistance after cycling is attributed to the elastomeric properties of SBR:CMC which accommodate volume changes and maintain interfacial contact between conducting agent and active material.
Additionally water soluble binders are favourable instead of to commonly used NMP to dissolve PVdF due to the higher costs and toxicity of NMP itself. [65]

The application of tailored bi-functional binder system of PEO:PVP (polyvinylpyrrolidone) 4:1 leads to sulfur electrodes with a competitive cycling performance in comparison to advanced carbon material sulfur electrodes though employing commercial Super-P and elemental sulfur (specific sulfur capacity of 800 mAh/g after 200 cycles at 1 C). In addition to the beneficial effects of PEO binder, PVP is able to diminish the polysulfide dissolution into the bulk electrolyte which is ascribed to strong affinity of polysulfides and oxygen atoms in carbonyl groups. Although the results are obtained with low sulfur loadings (50 w% sulfur and 0.5-0.8 mg/cm^2 electrode mass loading) the potential of tailoring binder functionalities is proven. [42][66]

The separator has to provide a porous structure to facilitate fast ionic transport, while being electronically insulating. Growth of lithium dendrites through the separator are to be prevented and membranes with high mechanical strength and sub-micrometer pores are utilized as a consequence. Besides, general characteristics such as wettability and chemical stability against the electrolyte system determine the suitability of a separator for certain battery systems Separators often consist of polypropylene PP, polyethylene PE, and layered structures thereof. The behaviour in case of elevated temperature can impose important safety features, therefore in LIBs shutdown separators (PP-PE-PP) are applied. In case of internal shorts induced by e.g. dendrites heat is generated and can cause thermal runaway. Shut down separators apply a low melting layer (PE) closing the pores and stopping ionic transport in case of T>130°C while the higher melting component (PP) ensures mechanical integrity. [67] E.g. In order to prevent thermal runaway, cells with Co containing positive electrodes should not be heated above 150°C as cells become thermally unstable, also the melting point of lithium at 180°C must not be reached.

In case of Li-S batteries the separator should restrain PS diffusion additionally. A lithiated-Nafion® coated separator can suppress PS shuttle and – if applied in thin layers – allows reasonable rate capability, comparable to uncoated separators. The ion-selective Nafion® coating consists of a polytetrafluoroethylene framework with sulfonated perfoluorovinyl ether groups (cf. Figure 8 c). SO_3^- groups enable ion hopping of Li^+-ions while negatively charged ions may not pass through the layer due to coulombic interactions. Thicker Nafion® membranes lower the second discharge voltage plateau due to increased transport resistance and cell polarization.[68][69]

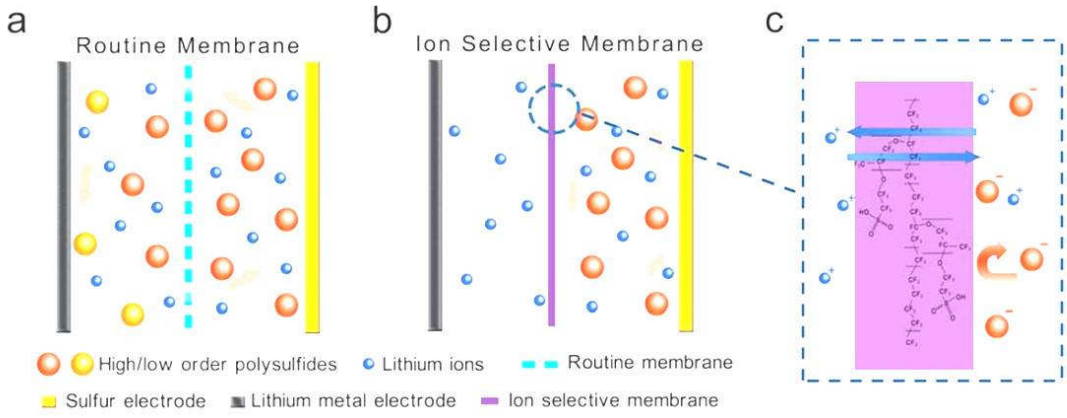

Figure 8: Schematic drawing of cells with (a) conventional separator, (b) ion selective separator and (c) function of ion selective membrane [69]

The transference number of lithiated Nafion® is determined with t_{Li^+} = 0,986.[70] The transference number refers to the ratio of the total current carried by a specific ion. If Li^+-ion transference numbers are close to 1 in the electrolyte, lithium dendrite growth can be suppressed predominantly. Therefore the application of ion selective separators indicates that lithium morphology can be positively influenced with ongoing cycling. [71]

2.4 Lithium electrode

Lithium has a high theoretical specific capacity of 3862 $mAh*g^{-1}$ combined with a low equivalent weight of 6.94 g/mol and the most negative electrochemical potential of –3.04 V (vs. SHE). These properties make it highly attractive as negative electrode material in rechargeable batteries, aiming at high voltages and high energy densities.

Besides its use in batteries, lithium is used for many different applications like in glasses and ceramics, in lubricants or in psychiatric medications. A share of 29% of the worldwide lithium consumption by end-use industry in 2012 were directed to battery production, only ceramics and glasses claiming a higher share of 35%. The abundance of lithium is about 20 ppm in earth's continental crust. About 39 million tons of lithium resources can be found worldwide and approximately 13 million tons are lithium reserves that can be exploited economically. Most important lithium sources are closed basin brines in which lithium is dissolved or occurs in form of deposits (58% of worldwide sources). Besides, lithium occurs as trace element in pegmatites and granites which is a main lithium source (26%; statistics of 2013). These values and estimations were given by U.S. Geological Survey USGS. [72]

Sulfur electrodes show a rather low average discharge voltage of 2.15 V vs. Li/Li^+, therefore the combination with metallic lithium as anode material is important to maximize the cell voltage. Several drawbacks yet have to be overcome before actually taking advantage of the promising lithium properties, keeping scientists busy for the past 40 years. The main challenges occur during repeated charging/discharging when non uniform lithium deposition/stripping cause the growth of high surface morphologies like dendrites, which can induce poor coulombic efficiency and serious safety hazards in case of a short circuit. [71][73] Rechargeable batteries with metallic lithium anodes have not yet been commercialized successfully and among other factors, impede the possible commercialization of Lithium-sulfur batteries. In commercially available LIBs e.g. graphite is used as Li^+ intercalation material substituting metallic lithium and circumventing its drawbacks (cf. 2, p.2). However, when combined with sulfur positive electrodes, the low

specific capacity and the higher potential of graphite in comparison to metallic lithium would diminish energy density.

2.4.1 Solid Electrolyte Interphase (SEI)

Organic, aprotic polar electrolyte solutions are thermodynamically instable and decompose spontaneously when exposed to metallic lithium. This process causes the creation of the solid electrolyte interphase (SEI), a thin layer of electrolyte decomposition products (originating from solvents and salts) which are insoluble in the electrolyte. After reaching a certain thickness, further reaction with electrolyte solution is prohibited because electron transfer through the interphase gets blocked while the layer remains permeable to Li^+-ions.

The composition of the SEI strongly depends on the applied electrolyte composition as well as on the *native* surface film formed on Li metal during production of Li foils. In general the SEI consists of a multilayered structure with species of lower oxidation state (e.g. inorganic species like LiF) created close to the lithium surface. These layers are permeable for Li^+ cations under electric field due to imperfections of the layer. Species of higher oxidations states (organic species like lithium alkoxy groups) are formed closer to the solution side, as lithium and solution species are no longer in direct contact and the reducing potential of Li is diminished by the inorganic SEI layer in between. The outer layer of the SEI film is porous (Figure 9a), because electron transfer through the inorganic salt layer is only possible at certain locations (holes, defects).[74][71][75][76]

Aurbach et al. conducted detailed studies of Li metal electrode surface composition in various electrolyte solutions applying FTIR, XPS and Raman spectroscopy. The surface species that are formed at lithium metal, when immersing in a typical Li-S electrolyte DOL/LiTFSI/$LiNO_3$/Li_2S_6 are identified and shown in Figure 9b. [77]

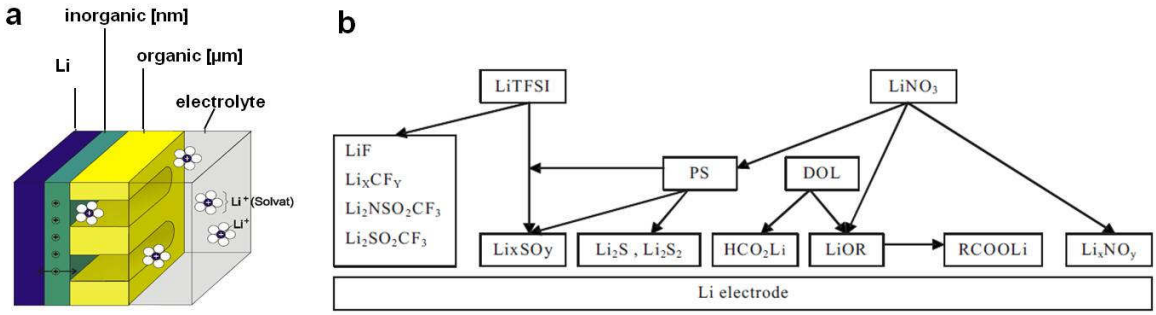

Figure 9: (a) schematic drawing of layered structure of SEI on lithium metal [76] and (b) surface species at Li metal in DOL/LiTFSI/$LiNO_3$/Li_2S_6 electrolyte [77]

2.4.2 Lithium morphology during electrochemical charge/discharge

Different Li metal electrode surface morphologies (dendritic, mossy and granular) can be observed depending on various factors like property and uniformity of the SEI and cycling conditions. A mechanism for lithium deposition is suggested by Yamaki [6] (Figure 10a). Lithium cations are deposited on lithium metal surface underneath the SEI during charging. The transport of Li^+-ions through the SEI is an important factor influencing the morphology of lithium deposition, with chemical and physical microstructure of the SEI being determining. As discussed in the previous paragraphs, the chemical composition of the SEI varies laterally and vertically.[78] In areas with thinner SEI (which opposes some resistance to ionic conductivity) or in areas with higher Li^+-ion conduction through the SEI, lithium deposition occurs more likely. In general, the electrode surface geometry influences ion migration and is enhanced at convex curved surfaces due to potential gradients. All this processes result in an inhomogeneous current distribution at lithium surface and thus influence the lithium deposition and dissolution (cf. Figure 10 b). Furthermore crystalline defects, grain boundaries, pits and cracks in the lithium metal may be preferred deposition sites. Although the SEI layer is elastic to some extent it may crack due to morphological changes and lithium grows out of the planar surface in dendritic shape. After full coverage with dendritic shaped deposits, preferred deposition at the substrate is hindered and kinks form at crystalline defects at the dendrite. The probability of the creation of mushroom shaped dendrites rises. Upon discharge (lithium dissolution) these reactions run in reverse. After dissolution of kinks, the dendrite dissolution occurs predominantly at the substrate surface due to larger current distribution. This can result in the creation of *dead* lithium as soon as the electrical contact to the substrate gets lost and isolated lithium is not taking part in electrochemical reactions anymore.[73][6][78][79][17]

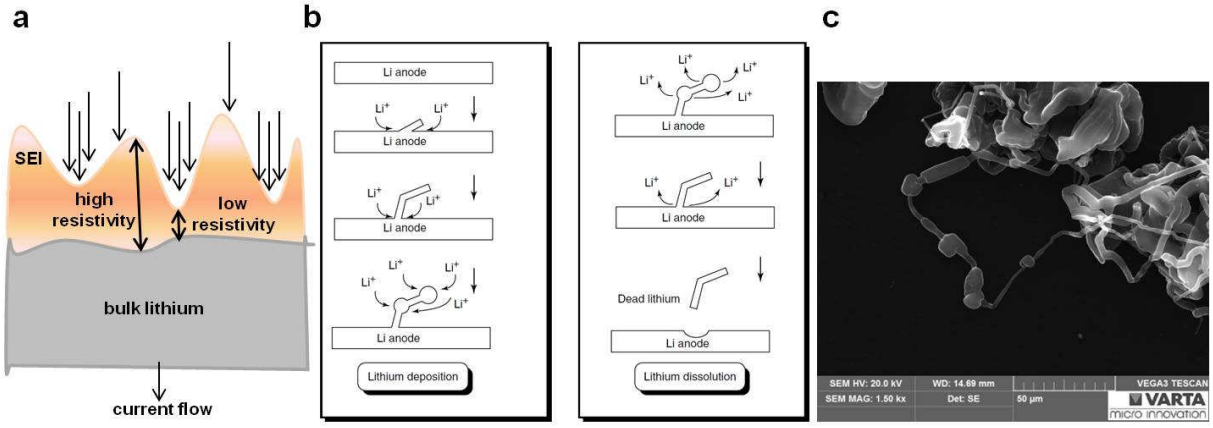

Figure 10: Schematic drawing of (a) current distribution on lithium/SEI redrawn from [73], (b) proposed mechanism for lithium deposition on lithium metal [6], (c) SEM image of lithium dendrite showing lithium kinks source: author

Among general battery working conditions, charge and discharge current density have a major influence on lithium surface morphology evolution during cycling. Higher current densities result in more dendritic depositions while at lower current densities mossy or particulate depositions are predominant and the SEI may not crack. [6] In case of lithium-sulfur batteries, PS species are present in the electrolyte solution and cover freshly created lithium surface with insoluble and non-conductive Li_2S and Li_2S_2. The electronic conductivity of created dendrites is lower and decreases the probability of further lithium deposition and thus of internal short circuit. [26]

2.4.3 Lithium cycling efficiency

Dead lithium is one of the main reasons for the poor cycling efficiency of lithium. Besides that, lithium is irreversibly consumed during the creation of SEI layer on freshly formed lithium surfaces and may have a high impact when large amounts of lithium are deposited in each cycle within high energy density cells. Cycling efficiency should be increased when suppressing dendritic growth. The isolation of lithium isles, encapsulated in the bulk SEI can cause further lithium losses. Due to local heating of the SEI by ion transport during deposition, electronic conductivity is enhanced in the SEI inducing Li deposition even in otherwise electrically insulating areas. [6] Moreover mechanical pressure influences Li deposition morphology as well as cycling efficiency. A more uniform deposition and a decreased amount of dead lithium are responsible for higher cycling efficiency under higher pressure load. [80]

The attributes of an ideal SEI layer may be summarized in uniform texture, flexibility and low resistance for Li^+-ion migration. Several attempts have been made to improve SEI properties and hence cycling efficiency by engineering the electrolyte composition and by engineering the structure and composition of Li metal anodes directly before implementation as discussed in the following chapter.

2.4.4 Design of lithium metal electrodes

In the following chapter several attempts for the design of lithium anodes in Li-S batteries are given.

Protection layers composed of Li_3N on top of lithium metal electrode are identified to suppress reactions between electrolyte solution and lithium metal and generate a stable and smooth SEI. In Li-S batteries undesired reactions of polysulfides and lithium are suppressed prohibiting polysulfide shuttle.[81] However, ex-situ formed layers may not be regained during operation and once the protective surface layer is cracked it can lead to non uniform lithium deposition and accelerated dendrite generation in the following cycles. [71]

The deposition of sulfur powder on Li negative electrodes prior to their use leads to an improved SEI layer and causes a decrease of insulating Li_2S deposition on Li surface during cycling (probed by XPS) in comparison to standard Li-S cells and Li-S cell with PS containing electrolytes.[82] However no long term cycling experiment has been conducted to confirm the superior performance over prolonged cycling.

In another recent approach for Li-S batteries metallic lithium is substituted by Li-B alloy (Li_7B_6) in which free lithium is incorporated in a sponge like Li_7B_6 framework. A uniform and stable SEI is created and dendrite formation is suppressed. Li_7B_6 is electrochemically inert and XPS measurements reveal the participation of boron in SEI layer formation, probably in form of B_2S_3. Lower anode polarization during operation of the Li-S cell increases the average discharge potential. However, a large amount of 30 w% of boron (47 w% free lithium) is necessary to observe positive effects on deposition morphology which in turn decreases the total energy density. [83]

The application of Li anodes with thin Li-Al surface layer shows improved cycling performance in PS containing electrolyte with even more efficient lithium protection than observed in $LiNO_3$ containing Li-S cells.[84] The decreased PS shuttle phenomenon is ascribed to the formation of a superior Al_2S_3 SEI protective layer on lithium surface.[31]

2.4.5 Substitution of the lithium metal negative electrode

Replacing metallic lithium electrodes by pre-lithiated alloys is an approach for successful enhancement of safety and cycling stability with more moderate electrolyte decomposition. However, substitution of metallic lithium is mostly accompanied by decreased average discharge cell voltages due to relatively higher anode potentials. An attractive anode material in terms of specific capacity is silicon (theoretical capacity of 4200 mAh/g at $Li_{4.4}Si$ stoichiometry). Aurbach et al. [85] use galvanostatically pre-lithiated columnar structured amorphous Si as anode material for a Li-ion sulfur system. A reversible capacity of 380 mAh/g of sulfur after 60 cycles (at ~0.17 mA/cm^2) is achieved in a galvanostatic cycling experiment using discharge capacity limited conditions to reduce volume stress at Si electrodes. Hagen et al.[86] use CNT-S vs. Si microwire array anode and achieve a sulfur capacity of 550 mAh/g after 200 cycles (at 1.28 mA/cm^2) when employing a Li_2S containing electrolyte. The superior cycling stability for cells with Li_2S containing electrolyte is ascribed to the higher lithium fraction in the cell and lower increase of cell impedance.

2.4.5.1 Replacing lithium by sodium – The Na-S battery

In general, an increased demand for lithium batteries for portable devices and a growing share of battery powered cars unsurprisingly raises the question for security of lithium supply and cost. A growing interest for possible alternatives generally leads to increased research activities towards sodium based electrochemistry. The share of sodium in earth's crust is much higher than that of lithium with 23000 ppm vs. 20 ppm respectively and is present in sea water. However sodium is three times heavier than lithium and shows a potential of –2.71 V vs. SHE. Both characteristics lower the obtainable energy density in comparison to lithium based negative electrodes.[2]

High temperature sodium-sulfur batteries are commercially available and currently used in stationary applications for peak load-levelling and emergency power applications due to the advantages of low material cost, high energy density, high efficiency and long life. In traditional sodium-sulfur batteries beta alumina ($NaAl_{11}O_{17}$) is used as solid electrolyte. This ceramic shows good Na^+-ion conductivity at temperatures at or above 300 °C, which is beyond the melting point of the active materials (eliminating dendrites and dendrite induced short circuits). Initially a two phase region of sulfur and Na_2S_5 is created. Upon discharge the reduction to Na_2S does not take place because further reduction is inhibited as soon as a solid Na_2S_2 layer which increases the

resistance at the positive electrode. Consequently the reduction is stopped at Na_2S_3 and only half of the theoretical specific capacity of sulfur is available resulting in a theoretical specific energy density of 760 Wh/kg (average discharge potential of 1.78-2.08 V). Keeping the cell at its high operating temperature requires high amounts of energy and molten sodium and sulfur being more reactive and corrosive may cause safety problems. Hence, research aims at Na-S batteries operating at lower or even at room temperature (RT). [87][88] In a recent approach a RT Na-S battery has been realized which shows a reversible specific sulfur capacity of 1000 mAh/g and a specific energy density of 750 Wh/kg (based on active materials) by combining a liquid carbonate based electrolyte and a specially designed cathode. The reaction of Na and S in liquid electrolytes usually shows a low reactivity and incomplete reduction. This problem is circumvented by employing a S_{2-4} cathode, in which metastable and highly reactive small sulfur molecules are trapped in microporous carbon. These electrodes prohibit the full oxidation to S_8 eliminating long chain PS dissolution and reaction with carbonate based electrolyte solvents.[87]

2.5 Electrolyte

A battery electrolyte is composed of a dissociated salt in appropriate solvents. The choice of electrolyte components is crucial to cell performance. The main purpose of the electrolyte solution is to facilitate fast ion transport between the electrodes. [17] The electrolyte should be electronically insulating, allowing the generated electrons to move solely through the outer electrical circuit between anode and cathode. Besides specific requirements for electrolytes in lithium-sulfur batteries, there are several aspects that are relevant to any battery system. Among them, the major criterion is the electrochemical stability of the electrolyte within the potential window of the electrodes, withstanding the strong oxidizing and reducing nature of cathode and anode respectively. As discussed previously, polar aprotic solvents are thermodynamically not stable in contact with lithium metal; hence the fast creation of a stable SEI is the determining factor for subsequent electrochemical stability. Apart from SEI creation, faradaic current should exclusively arise from redox reactions of active masses rather than from electrolyte reactions at the electrodes. Chemical stability of cell components such as separator, housing and electrode substrates should be granted in the applied electrolyte.[89] Since solvents ideally show a high solubility for the conductive salt, media with high dielectric constants and polar groups are preferably chosen on this account. Solvents of high dielectric constants show high viscosities. On the contraty, low electrolyte viscosity enables fast ion transport and prevents cell polarization due to generation of a concentration gradient. These controversial requirements are realized by

applying tailored solvent mixtures with each component introducing certain characteristics. Low freezing points, with only minor increase in viscosity at low temperatures, and high boiling points, ideally with low vapour pressures at elevated temperatures and low risk towards flammability and explosion respectively allow the use of a battery within a wide temperature range. [89]

2.5.1 Electrolytes in Li-S batteries

When selecting electrolyte components for lithium-sulfur system additional requirements need to be considered. An important factor is the electrolyte's ability to dissolve polysulfides. In Li-S batteries the electrolyte influences the reaction mechanism and the appearance of electrode surfaces due to dissolution and deposition reactions at positive and negative electrodes. The dissolution of sulfur and PS species increases utilization of the active material. However, if long chain PS species are not trapped within tailored host matrices, the dissolved active material tends to diffuse into the bulk electrolyte, and cause capacity loss, self discharge and PS shuttle. A high solubility of short chain PS species (Li_2S_n with $n<4$) should prevent or delay the formation of insoluble insulating layers on the electrodes.[90] As demonstrated in early works by Rauh et al. [91] applying UV-Vis spectroscopy, and in a more recent study by Hagen et al. [28] applying in-situ Raman spectroscopy, a varying electrolyte composition alters the reaction mechanism in lithium-sulfur batteries.

In current literature, most common electrolytes in Li-S batteries are based on lithium bis(trifluoromethane)sulfonimide (LiTFSI), lithium trifluoromethanesulfonate (LiTf), in combination with $LiNO_3$ co-salt in ethereal solvents. Less frequently lithium perchlorate ($LiClO_4$) salt is applied due to safety issues. Prominent salts applied in LIBs such as lithium hexafluorophosphate ($LiPF_6$) or lithium tetrafluoroborate ($LiBF_4$) are not well suited for lithium-sulfur electrolytes due to reaction of PS species with their anions. Additionally, $LiPF_6$ generates the strong Lewis acid PF_5 which initiates polymerisation of 1,3-dioxolane (DOL) and 1,2-dimethoxyethane (DME, monoglyme G1), two prominent electrolyte solvents in lithium-sulfur batteries.[31] Linear and cyclic ethers are chemically stable against polysulfides and therefore preferably used as electrolyte solvents for lithium-sulfur batteries. Mostly DOL and DME solvent mixtures or further glycol ether (glymes) based solvents like tetraethyleneglycol dimethylether (TEGDME) as single solvent or in mixture with lower viscosity solvents are applied. Moreover, sulfones like ethyl-methl sulfone (EMS) and sulfolane (tetramethyl sulfon TMS) are used, the latter being more viscous requiring in turn a mixture with a low viscosity solvent to achieve suitable ionic conductivities.[90] Carbonate based electrolytes that are implemented in LIBs are only

compatible with certain S-containing electrodes, e.g. like in cells applying sulfur electrodes with small S_{2-4} molecules [92][87] or sulfurized polyacrylonitril-composite PAN-S electrodes [93]. In most *conventional* Li-S batteries, however, the nucleophilic addition or substitution reaction of highly reactive high order polysulfides and carbonates prohibits their application.[94] Table 1 and Table 2 list physico-chemical properties of various solvents and viscosities as well as ionic conductivities of selected electrolytes for Li-S batteries.

solvent	structure	T_m / T_b [°C] a)	η [mPas]	ε	vapour pressure [mm/Hg] 20°C,a)	DN	AN
DOL		-95/76	0.597	6.9	70	18.0	
DME, G1	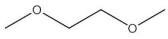	-58/85	0.407	7.1	48	24.0	10.2
TEGDME, G4	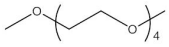	-30/276	3.25	7.7	<0.01	16.7	11.7
TMS 30°C		27/285	10.3	43		14.8	19.2
EMS	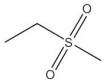	34/239					
THF		-108/66	0.459	7.43	143	20.0	8.0

Table 1: Physico-chemical properties of solvents used in Li-S electrolytes at 25°C [95][90] and a) data from Sigma Aldrich; T_m=melting point, T_b=boiling point, η =viscosity, ε=dielectric constant, DN=donor number, AN= acceptor number;

The solvent donor number (DN, dimension for basicity in terms of Lewis acid base theory) is an important factor influencing the electrochemical performance by means of the solubility of salts and hence PS. Solvents exhibiting high DN such as ether based solvents favour the dissolution of PS, based on the interaction of the strong Lewis acid Li^+ and donor solvent molecule and facilitate the dissociation of alkali metal salts. [91][96] The glyme structure and more precisely the number of oxygen atoms in the ether solvent molecule strongly influence the solvation ability of lithium salts. In solution the lithium ion is commonly coordinated by 6 oxygen atoms in most cases. [97] A superior solvation ability of (long chain) glyme solvents with multiple solvent donor

atoms (=ether oxygen) in one molecule in relation to other solvents with higher dielectric constants was found.[98] As reported by Barchasz et al. [99] the solvation ability of glymes affects utilization of sulfur in lithium-sulfur cells directly. On the one hand, the elongation of the second discharge plateau is induced by delayed precipitation of short chain PS in comparison to electrolytes consisting of shorter glymes, but on the other hand capacity retention is not affected positively.

Electrolyte	viscosity η [mPas]	ionic conductivity σ[mS/cm]
1M LiTFSI-DME/DOL	1.34	11.8
1M LiTFSI-0.25M $LiNO_3$-DME/DOL	1.51	11.1
1M $LiClO_4$-DME/DOL	1.05	7.95
1M LiTFSI-G4[a)]	13.1	2.72
1M LiTFSI-TMS[b)]	26.6	2.07
1M LiTFSI-TMS/DME(9/1)[b)]	16.3	2.82

Table 2: Ionic conductivities and viscosities of various electrolytes for Li-S batteries; a)[100]; b)[101] at 20°C; all the other values were determined at 20°C by the author

2.5.1.1 LiTFSI/$LiNO_3$/DME/DOL electrolyte system

In the following the specific roles of single components in LiTFSI/$LiNO_3$/DME/DOL based electrolyte system are discussed, as this electrolyte composition is used in this work.

DOL was initially used as co-solvent in toluene (TOL) and tetrahydrofuran (THF) based electrolytes [39] due to its low viscosity and good compatibility with metallic lithium. However it influences sulfur utilization in Li-S batteries negatively when it is used in too high concentration, because the reduction process is terminated early at the stage of Li_2S_2 instead of Li_2S as final reduction species.[90][102] In contact with metallic lithium the reduction products of DOL ($CH_3CH_2OCH_2OLi$ and HCO_2Li) induce some flexibility to the created SEI arising from oligomers of polydioxolane (–OLi edge groups, the oxygen atom is attached to the lithium surface) formed from ring opening reactions. As a consequence, higher cycling efficiencies in DOL based electrolytes can be obtained. [77] DME shows high PS solubility and increases the utilization of the active mass. In consideration of physico-chemical properties of solvents, DME (with high DN and low ε) facilitates the dissolution of PS and preferentially stabilizes long chain PS. On the contrary, DOL with lower DN shows less solubility for PS. DME-DOL solvent mixtures were first

applied by Sion Power and led to enhanced performance than the single solvent electrolytes. [103][16] However, safety hazards come along with the high vapour pressure of DME.

Chemical compatibility with PS species is a major factor for the selection of the appropriate salt. LiTFSI, as well as Litf, fulfil this criterion and are well working with ethereal solvents and PS species additionally. LiTFSI is well soluble in solvents with low dielectric constants such as DME or DOL. The large anion with its delocalized negative charge, caused by electron-withdrawing triflic groups and their conjugation with the lone electron pair of nitrogen is responsible for this behaviour. Despite the large anion, which normally causes higher viscosities, LiTFSI solutions show high ionic conductivities (e.g. ~12 mS/cm at 20℃ in DME/DOL (1:1 v:v), source: author). It is believed that high dissociation constant compensates lower ion mobility.[89]

The SEI formed in LiTFSI-DME-DOL solutions allows the ongoing reaction of PS with Li metal. Although PS species influence SEI composition by generating Li_2S protective layer, it tends to dissolve at the end of charge via reaction with high order PS species. Therefore, $LiNO_3$ is introduced which successfully promotes the creation of a stable SEI and PS shuttle suppression.[31][104][105] The application of $LiNO_3$ as additive or co-salt causes increased coulombic efficiency in Li-S batteries and was patented by Mikhaylik in 2004.[106] However, $LiNO_3$ is consumed continuously on fresh lithium surface upon cycling and therefore the positive effect will vanish sooner or later when all $LiNO_3$ has reacted. [107] Aurbach et al. investigated the function of $LiNO_3$ by studying the composition of the SEI present on the lithium metal electrode surface in an electrolyte solution consisting of mixture of DOL/LiTFSI/$LiNO_3$/Li_2S_6 by means of FTIR and XPS. The superior performance of Li-S cells applying $LiNO_3$ in the electrolyte is ascribed to the reaction of lithium metal with $LiNO_3$ to form insoluble Li_xNO_y species on its surface, which in turn react with dissolved polysulfides to form insoluble Li_xSO_y species and passivate the anode surface and suppress the PS-shuttle effectively. [108]

Figure 11 shows the impact of $LiNO_3$ on the potential profile of a lithium-sulfur cell.

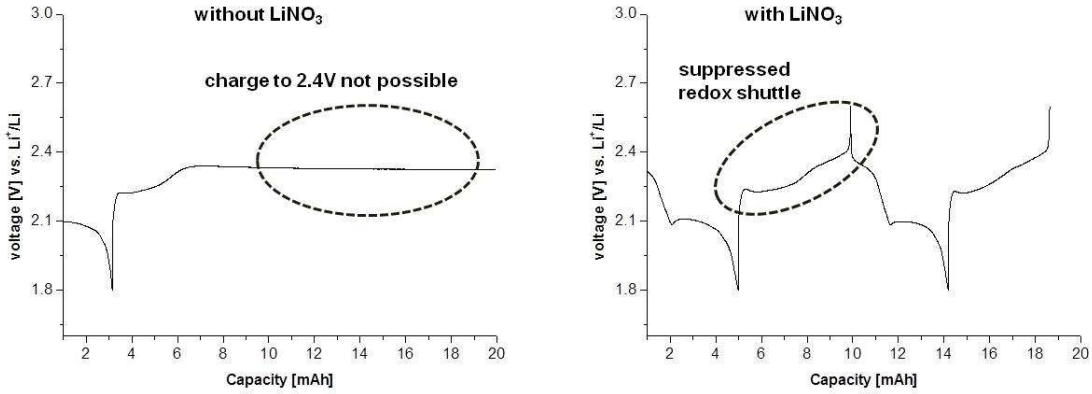

Figure 11: Impact of $LiNO_3$ on voltage profile of a Li-S cell, source: author

However, one should keep in mind that the oxidative nature of $LiNO_3$ may impose safety risks at high concentrations, elevated temperatures and high currents, constituting the same reason why $LiClO_4$ has been classified as impractical for industrial use. [89]

2.5.1.2 Stability of current collectors

Aluminium corrosion is a prominent problem in LiTFSI based electrolytes. In general Al starts to oxidize at 1.39 V vs Li/Li^+ but due to the generation of a protective passive layer (composition depending on electrolyte e.g. AlF_3, $Al_2(CO_3)_3$) on top of its surface high voltages (>3.5V depending on the electrolyte) can be realized. The oxidation potential of Al current collector in LiTFSI based electrolytes strongly depends on type of solvents and correlates with their dielectric constants (higher oxidation stability is given in low dielectric media, due to precipitation of initial oxidation products that block active reaction sites for further reaction).[109] Therefore, the low dielectric constants of the used ethers and low working potentials eliminate the problem of Al corrosion in lithium-sulfur system.

2.5.1.3 Liquid electrolyte consumption and electrolyte amount

Aurbach has stated that non-uniform lithium deposition (cf. chapter 2.4 p.26) and the formation of high surface lithium is inevitably accompanied by continuous electrolyte consumption in lithium metal cells applying liquid electrolytes at high charging rates (>1mA/cm^2).[110] Sooner or later the complete consumption of electrolyte will cause cells to run dry and prior to that the consumption of $LiNO_3$ during cycling will decrease coulombic efficiency of the battery.

Despite their important roles as film forming and PS solvating electrolyte components, continuously generated ether decomposition products can cause deterioration of battery performance and are summarized in Figure 12. Lithium-2-methoxyethoxid (LiOEM) is soluble in the electrolyte and is a main decomposition product of DME. This compound influences cathode performance negatively by decreasing sulfur utilization. Investigating the residue electrolyte after certain amount of cycles, it is shown that DME is preferentially depleted due to reactions with Li metal and PS. Besides, gaseous products cause swelling of cells. [16]

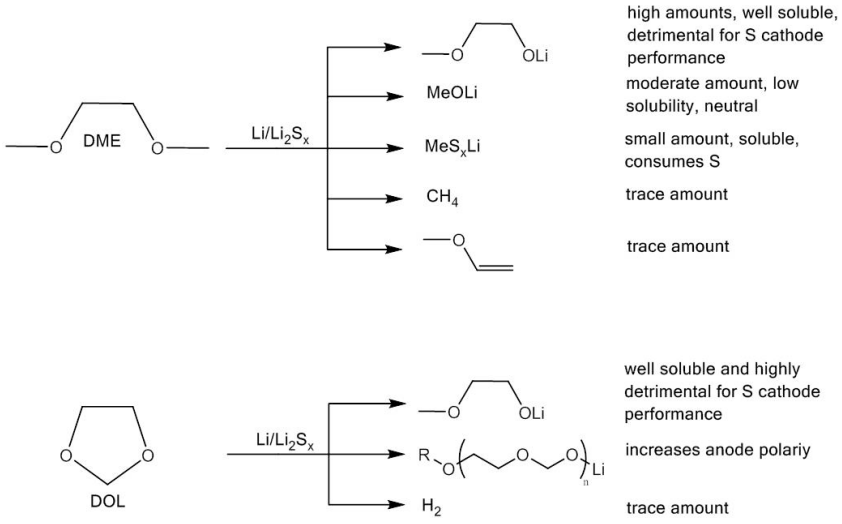

Figure 12: Reaction products of DME and DOL at Li surface in presence of PS [16][77]

One can easily deduce that in order to increase cycle life an excess amount of liquid electrolyte has to be added. This in turn increases inactive mass and lowers the achievable energy density of lithium-sulfur cells with liquid electrolytes. Studies on optimized electrolyte/sulfur ratios reveal that too high liquid electrolyte amounts cause faster capacity decay by leaching of PS species into the bulk electrolyte and increased precipitation of insoluble species due to Eq. 27 inside the separator or in dead corner of the cell. These reactions cause decreased coulomb efficiency. On the contrary, too low electrolyte/sulfur ratios cause poorly reproducible and shorter cycle life (early dry out and enhanced PS shuttle in case of high PS concentration; low initial capacities due to increased viscosity). The optimum electrolyte amount is dependent on the type of solvents and sulfur cathode as well as composition, thickness, specific surface area etc. and therefore, has to be determined individually for specific cells.[34][43] [111]

2.5.1.4 Modified electrolytes addressing lithium deposition morphology, stable SEIs and PS solubility

Modified electrolyte compositions are used in order to positively influence the creation of a stable SEI on the lithium surface, the suppression of PS shuttle, the morphology of lithium deposition or to alter PS solubility. Most of these requirements are addressed by applying different additives in the electrolyte. However, referring to $LiNO_3$ co-salt, a challenge common to many additives despite of their chemistry remains their continuous consumption during cycling. This is caused by the creation of the SEI on lithium surfaces generated continuously during deposition. In the following section some recent approaches based on additives, increased salt concentrations and binary salt electrolytes different from LiTFSI-$LiNO_3$ are summarized.

A promising electrolyte additive for Li-S cells is phosphorus pentasulfide (P_2S_5) which creates a soluble complex with Li_2S and decreases its irreversible precipitation. The passivation of lithium metal is enhanced by generating a thick layer with Li_3PS_4 as a main component in the SEI, which is highly conducting to Li^+ cations but eliminates the PS shuttle. Improved capacity retention and cycling efficiency is proven for 40 cycles. [112] Copper acetate additive in the electrolyte leads to improved SEI and morphology on lithium metal anode in a Li-S battery. A passivation film, mainly consisting of $Li_2S/Li_2S_2/CuS/Cu_2S$ and electrolyte decomposition products is found to be less likely to break, suppress dendritic lithium growth and shows reduced passivation of lithium surface during cycling. These improvements are achieved at the cost of reduced average discharge voltage during the first 100 cycles.[113] The use of ionic liquids mixed with organic solvents in a way to obtain suitable viscosities aims at the stabilization of PS molecules by suppressing disproportionation reactions of long chain PS species to create shorter PS and elemental sulfur. This approach is based on the hard and soft acids and bases theory (HSAB) according to which the hard acid Li^+ and the soft base polysulfide anion create instable lithium polysulfides, while soft acids like quaternary ammonium cations stabilize soft polysulfide anion bases. As a result, specific capacity and capacity retention are improved.[114]

Further it is shown by Scrosati's group [115] that addition of Li_2S_8 (5 w%) to a Li-S cell (LiFSI-TEGDME based electrolyte) influences sulfur electrode properties during cycling positively. A decreased ratio of polysulfide dissolution (from the positive electrode) into the liquid electrolyte and a better preservation of the initial positive electrode characteristics is observed and is ascribed to a buffer effect in accordance with Le Chatelier's principle.

A different attempt to control lithium morphology and PS shuttle is to apply high salt concentrations of 5M [116] and in a similar approach of Armand's group even 7M [103] LiTFSI salt concentrations ("solvent-in-salt" electrolyte). A more uniform lithium deposition by suppressing or the delay of dendrite formation is obtained. Moreover, the shuttle phenomenon is decreased because PS dissolution and diffusion of bulky long chain polysulfides through the viscous electrolyte is retarded. Reduced PS dissolution is ascribed to the common ion effect. However, this improvement is realized at the expense of low ionic conductivities, high costs and increased weight which influences energy density negatively. Recently, the combination of LiTFSI and LiFSI binary salt mixtures in DME/DOL (1M LiFSI – 0.5M LiTFSI in DME/DOL (1:1 v:v)) solvents has been discovered to improve smoothness of Li surface and the electrochemical performance in comparison to single salt electrolytes even after 100 cycles. LiFSI causes longer second discharge plateaus than in LiTFSI electrolyte, whereas higher cycling stability is given in LiTFSI electrolytes. These characteristics are combined in binary mixtures and additionally improved coulombic efficiency is observed. The smoother and dendrite-free lithium deposition is argued by an electrostatic shield caused by ion-pairing in a system with multiple anions.[117]

The successful suppression of dendritic lithium deposition is demonstrated by addition of small amounts of Cs^+ or Rb^+ cations to a $LiPF_6$ – PC electrolyte in symmetrical Li-Li cells. These cations exhibit a lower effective reduction potential and activity coefficient than Li^+ if applied in low concentrations and therefore are not reduced at Li^+ reduction potential. They rather accumulate around spots with concentrated negative charge and the generated positively-charged electrostatic shield prevents further lithium deposition on protuberances and forces lithium to deposit in neighbouring regions. [118] In a further study [119] the cross section of the Li deposits in the multi-cation electrolyte is investigated on Cu substrate and reveals self-aligned, compacted nanorod structures instead of dendritic formations. The important advantage of Cs^+ and Rb^+ additives is that they remain in the ionic state and are not consumed upon cycling. However, the main drawback is identified in the deterioration of lithium nanorod structure already after 10 cycles (loosely packed and porous structure) accompanied by a huge increase in surface area and therefore, electrolyte consumption. Despite the drawbacks, the expansion of this approach to Li-S system might be an interesting topic because of the striking advantage that these cations are not consumed over cycling.

2.5.2 Solid state Li-S batteries

The use of inorganic solid electrolytes (SE) for rechargeable lithium batteries goes hand in hand with the advantage of substituting flammable solvents and suppression of lithium dendrite formation and, in case of Li-S cells, the ability to eliminate PS shuttle. Various types of SE like crystalline (e.g. NASICON-type structures), glass (e.g. sulfide glasses like Li_2S-P_2S_5) and glass-ceramic (crystallization of glass electrolytes with the advantage of reduced grain-boundary resistance) are investigated, aiming at high ionic conductivity and electrochemical stability. [120] For their use in Li-S cells, poor ionic conductivity of the active material has further to be taken into consideration. Liang and co-workers [121] therefore apply Li_3PS_4 Li^+ -conducting glass electrolyte in combination with a lithium polysulfidophosphate (Li_3PS_{4+5} with a PS_4 core and chains of five S bonded via S-S bonds to three of the S atoms of the core), a lithium conducting sulfur rich cathode material and achieve 1200 mAh/g at 60°C after 300 cycles with regard to incorporated sulfur content based on breaking and forming S-S bonds in Li_3PS_{4+5}. Only one sloping discharge plateau is observed starting from ~1.8 V and approaching ~1.25°V at end of discharge. High polarization is obtained especially at RT resulting in low energy efficiencies of ~60% which is improved to ~83% at 60°C. Nagata and Chikusa [122] show a solid state Li-S cell by combining a positive electrode consisting of sulfur, $Li_{1.5}PS_{3.3}$ (SE with Li^+ ionic conductivity of $2*10^{-5}$ S/cm) and acetylene black as conducting material. As solid electrolyte $Li_{10}GeP_2S_{12}$ (with Li^+ ionic conductivity of $12*10^{-3}$ S/cm at 27°C [123]) is applied and Li-In alloy is used as negative electrode (0.6 V vs. Li/Li^+). Despite the impressive sulfur utilization of 1600 mAh/g after 100 cycles (at 1.3 mA/cm^2 = 1 C) and a coulombic efficiency of 100% the single discharge voltage plateau is below1.5 V vs. Li/In with steeper slopes in case of higher current densities.

The successful application of solid electrolytes may be an important step towards commercialized rechargeable lithium metal batteries. It may be an approach to realize high energy density cells as it circumvents the necessity of high liquid electrolyte amounts for achieving Li-S cells with long cycle lives and increases safety of resulting cells. Nevertheless, a lot of research has to be directed towards solid Li^+-conducting materials for discovering materials showing higher RT ionic conductivity and reduced interfacial resistances between electrode and electrolyte, which determines cell polarization, rate capability and achievable capacities and therefore energy density.

3 Experimental

3.1 Carbon/sulfur electrodes

3.1.1 S/C-electrodes for balancing experiments and lab-scale demonstrator cells

The sulfur electrodes which were applied for lithium polarization experiments in chapter 4.3.1 (p. 73) and for preparation of prismatically wound Li-S cells in chapter 4.4 (p.90) were provided by Fraunhofer IWS Dresden as part of MaLiSu project. Electrode development and further characterizations were conducted by Fraunhofer IWS Dresden.
The electrodes were composed of 42.5 w% conductive carbon, 42.5 w% sulfur and 5 w% CMC/SBR binder coated on 15 µm Al current collector foil. The total sulfur loading was ~0.90 mg/cm^2 in case of single side coated electrodes and ~1.7-1.8 mg/cm^2 (at each side) for double sided electrodes respectively. Prior to use, electrodes were dried at room temperature under vacuum over night. If not stated differently, these electrodes were used for the depicted measurements.

3.1.2 Sulfur electrodes prepared from HIPE structured carbon materials

The preparation of HIPE (high internal phase emulsion) structured carbon scaffolds for use in carbon/sulfur electrodes consisted of three consecutive steps: preparation of polyHIPE layer cured on metal foil, pyrolysis and sulfur infiltration.

3.1.2.1 pDCPD-HIPE preparation on metal substrates

The preparation process and composition of the standard HIPE material was done in accordance to the work of Kovačič [124][125]. Appropriate amounts of the monomer DCPD (heated to temperatures about 33°C) and Pluronic®L-121 serving as surfactant were put in a three-neck-round bottom flask together with toluene as solvent to prevent crystallization of DCPD at RT (e.g. 90 µl for 4 g of monomer). The mixture was stirred at 400 rpm for 1h to ensure dissolution of the surfactant in the monomer. Deionised water was added drop wise (1 drop/5 sec) which caused the former colourless solution to turn milky white as the water in oil emulsion was formed. The emulsion was further stirred at 600 rpm for at least 2h until only a

single visible phase was present. Afterwards M2 initiator ([1,3-Bis(2,4,6-trimethylphenyl)-2-imidazolidinylidene]dichloro-(3-phenyl-1H-inden-1-ylidene)(tricyclohexylphosphine)ruthenium(II)) solution in toluene (0,03mol/l) was added. After stirring at 600 rpm for 30 seconds the emulsion was directly cast on nickel foil (26 µm) using a doctor blade. The casting process was done within 3 minutes as long as the viscosity of the polymerizing emulsion allowed an easy casting process. As prepared foils were placed between two glass plates with 7 mm spacer and put in a compartment drier at 80°C for two hours for curing. Evaporated and condensed water on the upper glass plate was removed. For oxidation of the polyDCPD the foils were kept at 42°C for several days until a yellowish discoloration appeared.

Additionally Al foil (roughened in an edging process in hot 5 w% KOH for 30 seconds), Ni-mesh (rectangle Ni mesh with W/S=99 µm and W/K=101 µm and a wire diameter of D/S=60 µm and D/S=63 µm) and Cu foil (20 µm, roughened dendritic surface) were tested as substrates.

If not stated differently, the following ratios, based on the initial monomer amount, were used for preparation of standard polyDCPD: 7 v% Pluronic®L-121, 80 v% H_2O (deion.) and a monomer-initiator ratio of ~7000:1. An internal phase of 80v% corresponds to a porosity of 80% in the resulting polymer. As prepared polyDCPD-HIPE materials are referred to as pDCPD(80;7). Additionally an increased surfactant amount of 21 v% was tested and is referred to as pDCPD(80;21).

3.1.2.2 Pyrolysis

A tube furnace (Carbolite T1600 tube furnance) was used for pyrolysis which was conducted in argon atmosphere. If not stated differently the oxidized polyDCPD samples on metal substrates were heated at a rate of 4°C/min to a set temperature of 600°C which was hold for 2h prior to cooling at a rate of 0.8-1°C/min. For the determination of electrical conductivity bulk samples without metal substrate were pyrolysed at temperatures of 1400°C, 1100°C, 900°C, 700°C and 500°C while heating rates were kept constant.

3.1.2.3 Sulfur infiltration

The amount of carbon loading on the rectangular cut electrodes was calculated from the average mass loading on stamped electrodes. The applied amount of sulfur ratio of 60 w% or 46-48 w% was calculated based on the obtained mass of carbon layer on the metal substrates. Sulfur was dissolved/dispersed in toluene and this paste was spread on carbonized samples in

order to achieve a more homogeneous distribution. These were placed in a Büchi oven (Büchi glass oven B 585) and heated to 155°C under inert gas. All together the sulfur infiltration process was accomplished within 30 min. As soon as sulfur melted (at 119.6°C), it was completely soaked into the porous carbon material. The amount of sulfur inside the electrode was determined by weight.

3.2 Characterization methods

All steps which were performed under inert atmosphere were conducted inside an Ar filled glove box (MBraun Labmaster; H_2O and O_2 content below 0.1 ppm).

3.2.1 Scanning Electron Microscopy (SEM)

Scanning electron microscopy (Vega-3, Tescan) with a secondary electron detector was used to investigate the surface morphologies of electrodes and pDCPD materials. The samples were sputter coated with a ~3 nm thin layer of gold to increase electrical conductivity (Cressington 108auto sputter coater). A tungsten cathode was used as electron source and an acceleration voltage of 20 kV was applied. 3D images were generated applying 3D software (Mex 5.1) by recording SEM images at a tilt of 3°. Moreover an Energy Dispersive X-Ray (EDX) Detector was applied for probing the elemental composition.

For SEM sample preparation of lithium metal foil electrodes in chapter 4.3.2 (p. 78), electrodes were disassembled from the pouch cell and washed in a 1:1 mixture of DME and DOL under inert atmosphere. The samples were exposed to air during sample transfer into the sample chamber for approximately 30 seconds. In this case samples were not sputter coated. A significant change of Li morphology was not expected within this time and observed surfaces match comparable SEM images in literature.

3.2.2 Measurement of ionic conductivity viscosity and density of liquids

Ionic conductivity measurement was performed under inert gas applying a Knick 703 conductivity meter. The measurement cell was placed in a Thermostat (Julabo F32 EH) which allowed accurate adjustment of temperature. The sample was held at each temperature for 15-20 minutes to ensure thermal equilibrium. The cell constant was determined using aqueous 0.1M NaCl solution. Obtained results were used in Table 2.

A Stabinger Viscometer (Anton Paar SVM 3000) was used for viscosity and density measurements. About 4 ml of sample were immediately transferred from Ar filled glove box inside a syringe. Density and viscosity were determined in dependence of temperature. Obtained results were used in Table 2 and energy density calculations respectively.

3.2.3 Four point probe measurement of electrical conductivity

For the determination of electrical conductivity of polyDCPD derived carbon materials in dependence of pyrolysis temperature cuboid shaped pDCPD(80;7) samples of initial dimension of 20 x 1.5 x 0.5 cm^3 were used. These bulk samples had to be prepared without metal foil substrate in order to obtain electrical conductivity solely of the carbon material.

The electrical conductivity was determined applying four point probe measurements. A current of 100 mA was applied (Knick Präzisionsstromgeber) over a 20 cm part of the sample. The voltage drop was taped (Fluke multimeter 11) over 10, 8, 6 and 4 cm distances within the current carrying sample. Applying Ohmic law, electrical conductivity was calculated.

3.2.4 ATR-FTIR spectroscopy

Oxidation of pDCPD samples was confirmed by ATR-FTIR (Perkin Elmer Spectrum Frontier) within a range of 4000-650 cm^{-1} and a resolution of 4 cm^{-1}. Ge coated KBr optic is applied in the spectrometer. Diamand/ZeSe is used as ATR-crystal and determines the above mentioned wavelength range. During measurement, pressure was applied to ensure good optical contact between the crystal and the solid sample. Spectrum 10 (Perkin Elmer) was used as software.

3.2.5 Electrochemical characterization

Galvanostatic cycling and cyclovoltammetric measurements were performed on MACCOR Series 4000 battery tester and Biologic MPG-2 respectively. If not stated differently, cut-off voltages duting galvanostatic cycling measurements were set at 1.8 V and 2.6 V vs. Li^+/Li and the a C-rate was 0.1 C for a maximum of 200 cycles. The C-rate defines the charge and discharge current of the cell during galvanostatic measurement. Applying a C-rate of 1 corresponds to charging or discharging the cell within one hour. It was calculated based on the theoretical capacity of sulfur (1672 mAh/g) irrespective of the practical sulfur utilization. Experiments were either controlled as half cell (control of cut-off voltages between reference and working electrode E_{RE} - E_{WE}) or full cell (control of cut-off voltages between working and counter

electrode E_{WE} - E_{CE}). Auxiliary channels were added if the monitoring of single electrodes potentials $E_{CE} – E_{RE}$ or $E_{WE} – E_{RE}$ were necessary. Cyclovoltammetric measurements were performed at a scan rate of 0.03 mV/sec.

3.2.5.1 Test cells for electrochemical characterizations

Electrochemical measurements were performed in Swagelok® T-cells or in pouch cells. A schematic drawing is shown in Figure 13.

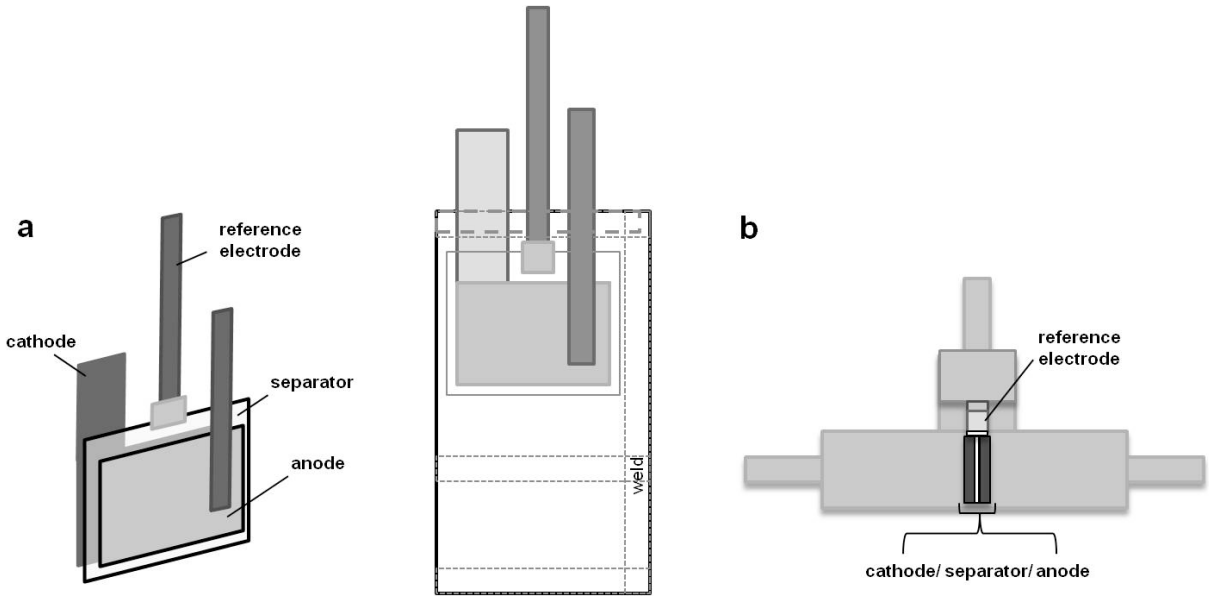

Figure 13: Schematic drawing of cell types for electrochemical measurements (a) pouch cell and (b) Swagelok®-T cell, source author

An acrylate/Al/PP compound foil served as casing of the pouch cells, with PP (polypropylene) layer being the inner layer. For standard Li-S cell measurements the electrode stack consisted of a 2*3 cm^2 sulfur/carbon working electrode and a metallic lithium stripe (100µm or 230µm) counter electrode, which were separated by Celgard 2400 separator. Compound foil and PP separator were dried under vacuum at 90°C prior to cell assembly. The current collector tap of the sulfur/carbon electrode was cut out of the Al foil on which the active material layer was casted while a Ni-foil stripe, pressed on Lithium served as current collector tap at the negative electrode. Additionally a reference electrode was placed between the current collector taps as depicted in Figure 13 a. The reference electrode consisted of a small piece of lithium foil wrapped around the Ni foil current collector tap and was in contact with the separator. After electrolyte addition the compound foil was heat-sealed and a stripe of hot melt adhesive was

additionally placed around the metal taps, ensuring the tightness of the sealing at metal/PP contact areas. Cell assembly was accomplished under inert atmophsere. If not stated differently, assembled cells were opened at ambient conditions and were instantaneously vacuum-sealed to eliminate Ar from inside the cell. During electrochemical measurement, cells were placed in a jig to apply a moderate pressure on the electrode stack.

The size and capacity of the pouch cells was variable. Single layer cells (applying single sided positive and negative electrodes) or cells with prismatically wound electrodes were prepared. For the latter, double side coated positive electrode foil of various lengths were wrapped together with lithium foil of the same size, which was enveloped in a separator. In order to obtain a prismatically wound electrode stack, the layered electrodes were bended all 2 cm. No reference electrode was placed in prismatically wound cells. In this way, cells of higher capacity and energy density than simple single layer pouch cells were prepared.

For measurements in Swagelok® T-cells, electrode size was fixed at 12 mm diameter. Celgard 2400 was used as separator. Additionally a nonwoven PP separator (Freudenberg 2226) was used for separating perpendicular placed lithium reference electrode from working and counter electrode. A Mylar® foil was used to electrically isolate steel cell and electrode stack and was in contact with electrolyte and electrodes. Pressure was applied on the electrode stack by a spring. Cell assembly was performed under inert atmosphere.

3.2.5.2 Electrolyte

If not stated differently a solution of 1M LiTFSI – 0.25M $LiNO_3$ in a DME/DOL (1:1 w:w) mixture served as the liquid electrolyte. LiTFSI was dried at 90°C under vacuum for minimum of two days. $LiNO_3$ was used as received. DME and DOL were distilled and were stored above molecular sieve for minimum one day prior to use. The obtained electrolytes showed a water content below 20 ppm. For electrochemical tests, the electrolyte amount in standard cells was held constant at 14 µl/mg of sulfur present at the applied electrode. The electrolyte amount was calculated based on the theoretical amount of sulfur at the electrode irrespective of the actual sulfur utilization. Electrolyte preparation was performed under inert atmosphere.

For preparation of polysulfide (PS) containing electrolyte, stoichiometric amounts of metallic lithium and elemental sulfur to obtain a 0.15M Li_2S_6 solution were mixed in DME-DOL (1:1 v:v) solvent mixture and stirred for four days at room temperature whereupon a dark red solution was formed with no solid reactant residues.

4 Results and Discussion

The following section is divided into three chapters dealing with different questions on Li-S systems. Firstly, polyDCPD derived polyHIPE structured carbon matrices as sulfur host for the preparation of sulfur electrodes were evaluated. Apart from considerations on the positive electrode, the behaviour of the lithium negative electrode in Li-S cells was investigated in terms of surface morphology evolution (via SEM study) and electrode polarization during electrochemical testing. In the last section a general evaluation on practically obtainable energy densities in Li-S cells and the influence of several factors on energy density are discussed.

Prior to the discussion of the respective results, a short summary of factors that influence electrochemical performance will be given.

4.1 Discussion of electrochemical performance determining factors in Li-S cells

Prior to the discussion of specific results, some general remarks on the interpretation of electrochemical results are given in the following section. These include considerations on the influence of several factors such as the type of electrochemical testing device or the influence of the C-rate on the electrochemical performance of different types of Li-S cells.

While initially all electrochemical tests were performed in Swagelok®-T-cells due to low material effort and convenient assembly, the set up was changed to pouch cell (cf. Figure 13 a). Testing identical materials under comparable conditions in pouch cell and Swagelok® T-cell respectively resulted in significant differences in the galvanostatic cycling performance. As can be seen in Figure 14 a it was found that improved initial capacity (specific discharge capacity of sulfur +200 mAh/g) and capacity retention (specific discharge capacity of sulfur after 220 cycles +400 mAh/g) was obtained when performing the measurement in pouch cells. This behaviour might have been caused by insufficient seal tightness or the applied pressure on the electrode stack instantaneously after electrolyte addition (squeezing out the electrolyte before it was soaked into the separator and porous carbon/sulfur electrode).

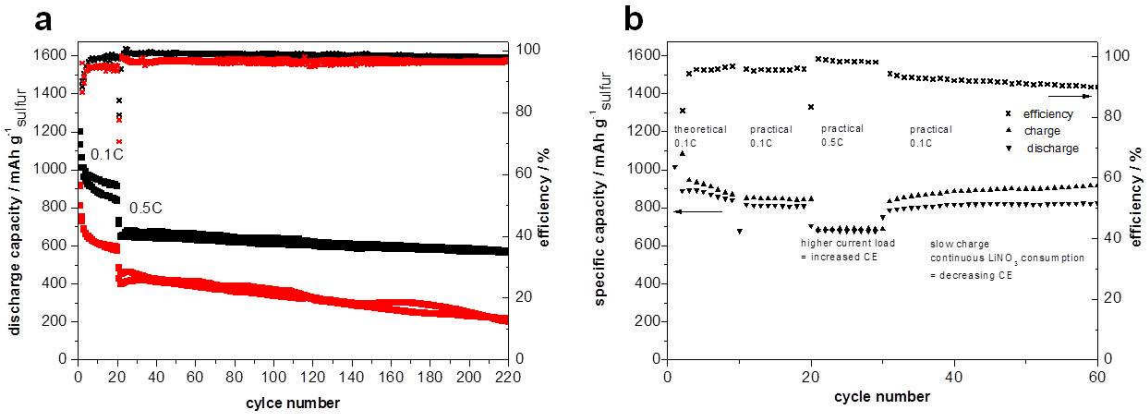

Figure 14: Influence of cell set up (pouch cell vs. Swagelok ® cell) on capacity retention and influence of C-rate on CE on capacity

Within this work the applied C-rates were determined based on theoretical sulfur loadings at the electrodes. At low sulfur utilization the applied theoretical C-rate translated to higher current loads with regard to actually active sulfur. Higher current loads in turn resulted in further decreased sulfur utilization. Considering C-rate and coulombic efficiency (CE) it was observed that CE increased with increased current load as show in Figure 14 b, where CE increased from 95.5% to 98.5% due to increase of the C-rate from 0.1 C to 0.5 C after 20 cycles. This observation is explained with regard to less pronounced PS-shuttle in case of higher charge current, according to Eq. 30. In turn it can be concluded, that CE is increased in case of lower sulfur utilization when the deviation of theoretically planned and practically applied current load (considering the actual active sulfur) increases.

The general impact of the electrolyte amount on electrochemical performance is discussed in chapter 2.5.1.3 (p. 37) and 4.4 (p. 90). In this work the electrolyte amounts were held constant for all experiments within one series for comparability reasons.

Sulfur utilization heavily depends on electrode thickness and sulfur ratio (w%S) in a sulfur electrode. Low sulfur ratios and thin electrodes result in high sulfur utilization. [126] [43]

All the above mentioned factors influence the values of key performance parameters of Li-S cells and make direct comparison of various results (in literature) difficult. The evaluation of Li-S cell performances has to be performed under consideration of above stated factors.

4.2 Evaluation of sulfur electrodes prepared from polyHIPE structured carbon matrices

Macroporous polymer coatings with open cellular morphology were prepared via ring opening metathesis polymerization (ROMP) of dicyclopentadiene (DCPD)/water high internal phase emulsion (HIPE) films casted on metal substrate. The cured polyDCPD (pDCPD) layers were oxidized and converted to a carbon material during pyrolysis under preservation of the typical HIPE structure. [127] The resulting carbon scaffold served as conducting matrix for sulfur electrodes. The electrochemical performance of the as prepared electrodes was investigated.

Figure 15 provides an overview about the preparation of sulfur/carbon electrodes based on HIPE structured carbon matrices.

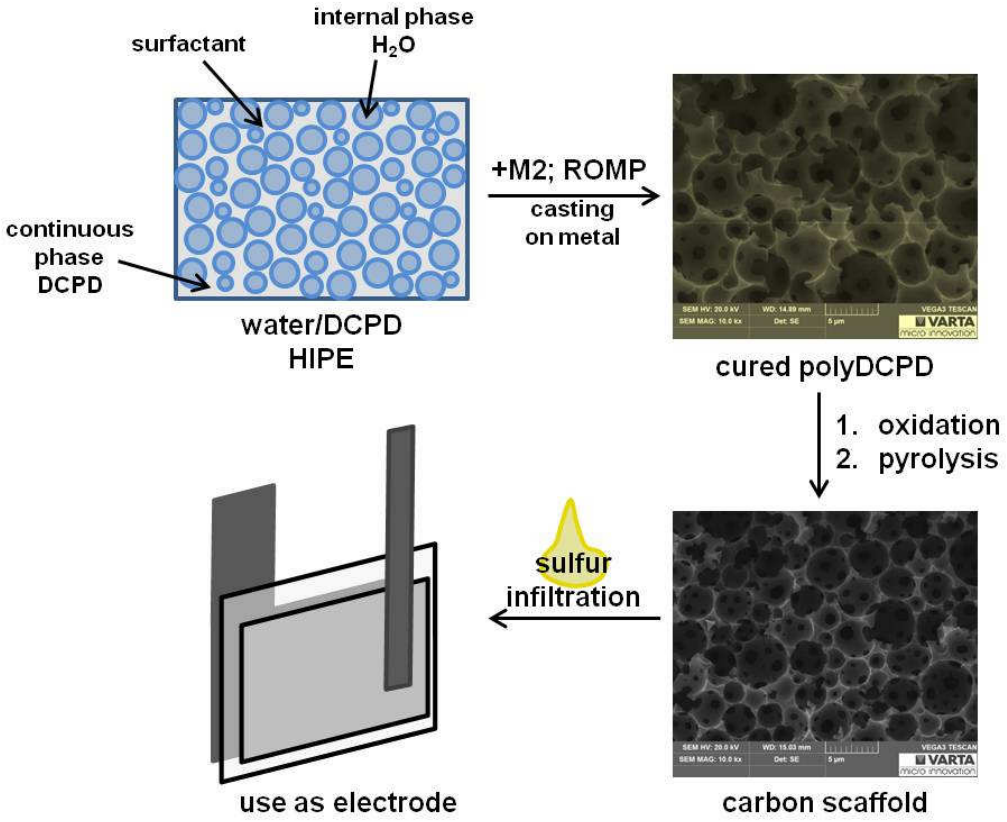

Figure 15: Schematic drawing of the preparation of HIPE structured electrodes

In general, a high internal phase emulsion is characterized by an internal phase with volume fraction above 74 v%. Here, the continuous phase consists of DCPD, a cheap by-product of the petrochemical industry. Water serves as the internal phase and a surfactant stabilizes the emulsion. DCPD is easily polymerized via ROMP applying M2 ([1,3-Bis(2,4,6-trimethylphenyl)-2-imidazolidinylidene]dichloro-(3-phenyl-1H-inden-1-ylidene)(tricyclohexylphosphine)ruthenium(II)) catalyst as initiator and yields highly cross-linked polymers of high toughness and rigidity. In DCPD the norbornene double bond reacts more easily via ROMP than the double bond in the cyclopentadiene ring. The latter is partially reacting and is responsible for cross-linking (crosslinking via olefin metathesis), while further cross-linking occurs via olefin addition. The resulting highly unsaturated polyDCPD network allows for easy functionalization.[128] [129]

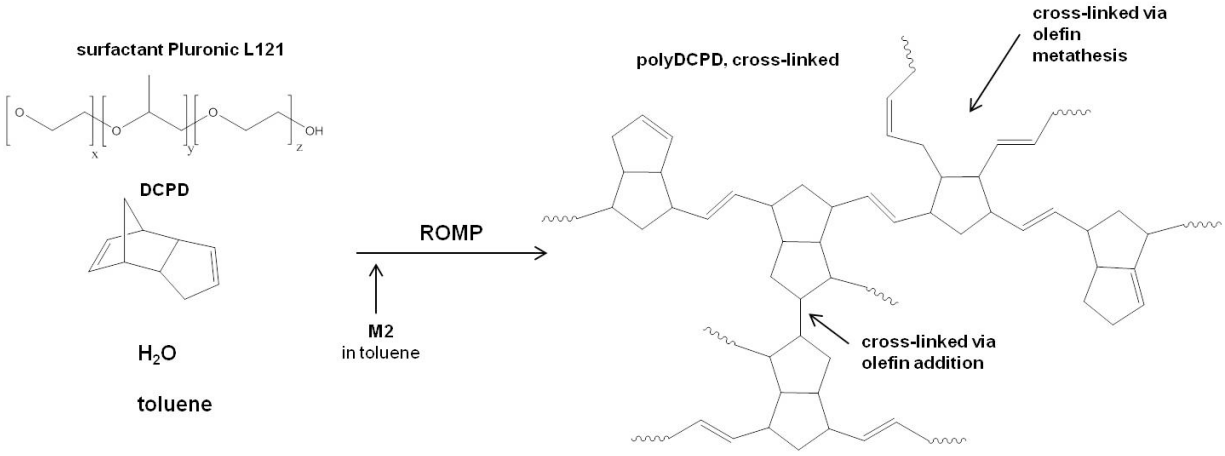

Figure 16: ROMP of DCPD, redrawn from [128]

Through ROMP of the continuous phase of a high internal phase emulsions, polymers of typical HIPE structures are accessible. This is characterized by pores (voids) which are interconnected through smaller holes in the pore walls (windows) and high porosity (>74 v%). Subsequent oxidation and pyrolysis yields an interconnected macroporous carbon structure. The sponge like structure could be especially useful when considering its application as battery electrode material, where the interconnected pathways could be filled with electrolyte and allow for fast Li^+-ion diffusion to all electrode regions.

4.2.1 Preparation of HIPE structured carbon layers on metal substrates

In the following section the preparation of HIPE structured carbon thin films on metal substrate and their use for preparation of sulfur electrodes is discussed. The initial formulation and the preparation method (cf. chapter 3.1.2 p. 42) were established by Kovačič et al. [124][127] while the feasibility of sulfur electrode preparation was investigated within this work. In this context, the effect of different metal substrates (Ni foil and Ni mesh, Al foil and Cu foil which served as current collectors in the resulting electrodes), and the effect of increased surfactant amount (7 v% in standard formulation vs. 21 v%) on electrochemical performance of resulting sulfur electrodes was studied.

Criteria for useful porous carbon coated metal substrates, which could be further processed to sulfur electrodes, included a well preserved adhesion of the polymer and the resulting carbon layer to the metal substrate. Further a reasonable thickness of the coatings is necessary to allow for high sulfur loadings and hence the possibility to achieve high energy density electrodes.

4.2.1.1 Preparation of HIPE structured polyDCPD coatings on Ni foil substrate

Polymer coatings obtained from emulsions with 7 v% surfactant (pDCPD(80;7) on Ni foil

The surface morphology and the yield of the polymer (as layer on the metal foil) strongly depended on the set up used during curing. [124][130] The coated foils were placed between two glass plates during polymerization and rubber stripes were used as spacer, in a way that an air chamber was created and was in contact with the curing emulsion during polymerization. Therefore the upper glass plate was not in direct contact with the sample. The surface morphology of the resulting film of pDCPD(80;7) is shown in Figure 17 a and revealed a rather closed surface with a few irregularly distributed pores. The surface seemed to be covered by a thin polymer layer which covered up the HIPE structured bulk underneath. The layer on top might have been created through evaporation and re-condensation of the monomer at the phase boundary. The phase boundary emulsion/air further enhanced the creation of a closed surface due to hydrophobic nature of air. [131]

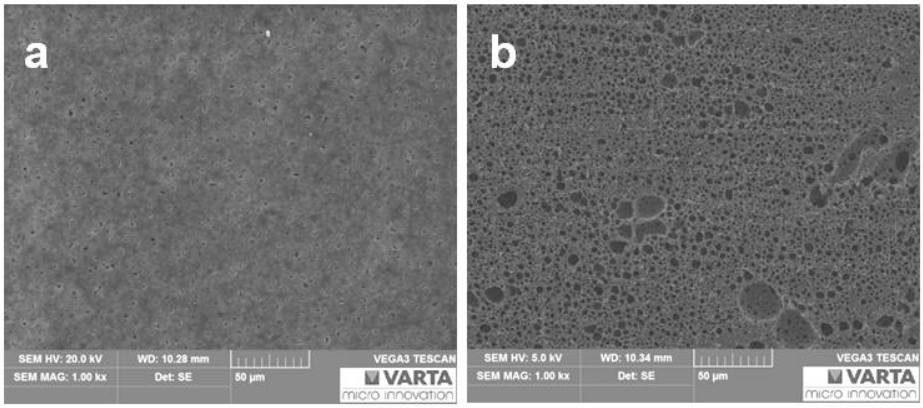

Figure 17: SEM pictures of the surface morphology of polyDCPD-HIPEs (pDCPD (80;7)) in contact with air (a) and in contact with glass (b) during polymerization

On the contrary, HIPE structured pDCPD(80;7) films which were cured in direct contact with glass (cf. Figure 17 b) were prepared and confirmed the afore-mentioned dependence of surface morphology on curing conditions. A porous surface was revealed probably caused by the adhesion of polar water drops on the polar glass substrate.[131] For use as sulfur host material the morphology of porous surface structure would be less favourable, as the diffusion of soluble PS species out of the positive electrode area is facilitated.

Apart from the different surface morphology, a higher polymer yield was obtained when the curing polymer layer was directly covered with glass. Due to different polymerization conditions (air contact vs. glass contact) two coatings prepared from the same emulsion with the same wet film thickness and curing them under identical temperature and time conditions resulted in polymer loadings of ~2.0 mg/cm^2 and ~2.5 mg/cm^2. However, the adhesion of as prepared polymer layers to the metal substrate was insufficient and prevented further investigations as electrode material.

Varying polymer yields could be attributed to the evaporation of monomer. While elevated temperatures were necessary to speed up polymerization reaction, cyclopentadiene was created through thermally induced retro-Diels Alder reaction of DCPD. [130] Cyclopentadiene is volatile and therefore escapes into the gas compartment in the reaction chamber. Moreover the evaporation of monomer influenced the inner structure of the polymer film as pore walls get thinner and windows widen.

On the other hand, the evaporation of water further influenced the appearance of the inner structure of the polyDCPD-HIPE structure. Partial removal of the dispersed phase during

polymerization of DCPD resulted in a deformed pore structure with pores being rather ellipsoid than spherical.

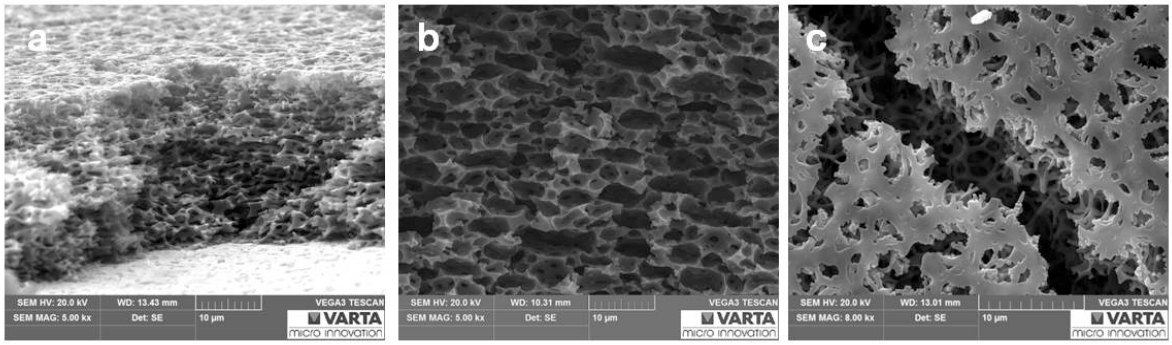

Figure 18: Inner structure of pDCPD (80;7) with deformed pores in cross section of coating on Ni substrate (a) of bulk piece (b) and surface of coating with a crack that reveals a top view inside the coating layer (c)

The samples which were directly covered with glass during curing showed spherical pore structures as expected, as monomer and water evaporation were not possible during curing and hence the pore structure mainly depended on stability of the emulsion. As a consequence of suppressed monomer evaporation polymer yields were much higher as discussed above.

In general it was observed that thicker polymer layers showed decreased adhesion to metal substrate after polymerization (or after pyrolysis) and the probability that the coating peeled off during preparation steps increased. A possible reason could be that the shrinkage of the polymer (walls) during polymerization caused a contraction force towards the inside of the layer, which was less pronounced for thinner coatings.

Polymer coatings obtained from emulsions with 21 v% surfactant pDCPD(80;21) on Ni foil

Aiming at smaller pores, which would be favourable for achieving higher sulfur utilization and increased retention of PS in the carbon structure, a higher surfactant amount of 21 v% instead of 7 v% was applied. As can be seen when comparing the SEM images of sample pDCPD(80;21) in Figure 19 to pDCPD(80;7) in Figure 17 and Figure 18, a visible reduction of pore size came along with the higher surfactant amount. However, examination of the surface revealed more cracks in the pDCPD(80;21) sample when observing the surface in the polymer thin-film (SEM investigation of oxidized sample).

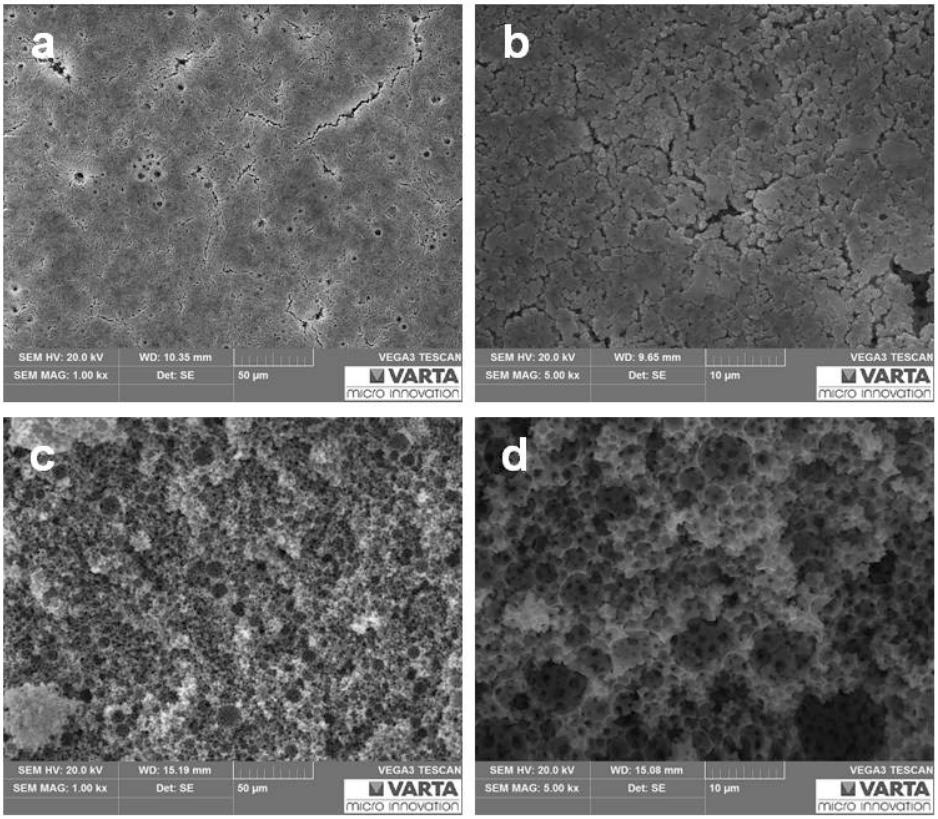

Figure 19: Surface of thin layer of pDCPD(80;21) on metal substrate at 1kx and 5kx (a,b) and cross section of bulk piece of pDCPD(80;21) at 1kx and 5kx (c,d)

The origin of cracks in case of higher surfactant amounts was described by Kovačič [125] for bulk samples with varying surfactant amounts between 0.25 v%-10 v% of the emulsion. The deterioration of mechanical properties of obtained polymer samples was attributed to the accumulation of surfactant inside the DCPD phase in case of higher ratios, which added additional pores and cracks inside the polymer phase, while at lower surfactant amounts the amphiphilic compound was solely located at the water - DCPD phase boundary.

4.2.1.2 Oxidation of pDCPD

Storing the samples at 42°C in air resulted in oxidation of the unsaturated polymer structure after several days as proven by FTIR measurement. Figure 20 a shows the ATR-FTIR spectra of basic materials (DCPD and Pluronic L121) and in Figure 20 b the polymerized pDCPD after one day of storage at ambient conditions (hardly oxidized) and after one month storage at 40-42°C in air (oxidized, yellow discoloration of polymer) is shown. The creation of hydroxyl (–OH) and

carbonyl (–C=O) groups upon oxidation was proven by the IR-absorption frequencies at 3400 cm^{-1} and 1700 cm^{-1} respectively and came along with a decreased IR-absorption at 2800-3200 cm^{-1},indicating the reaction of double bonds with oxygen.

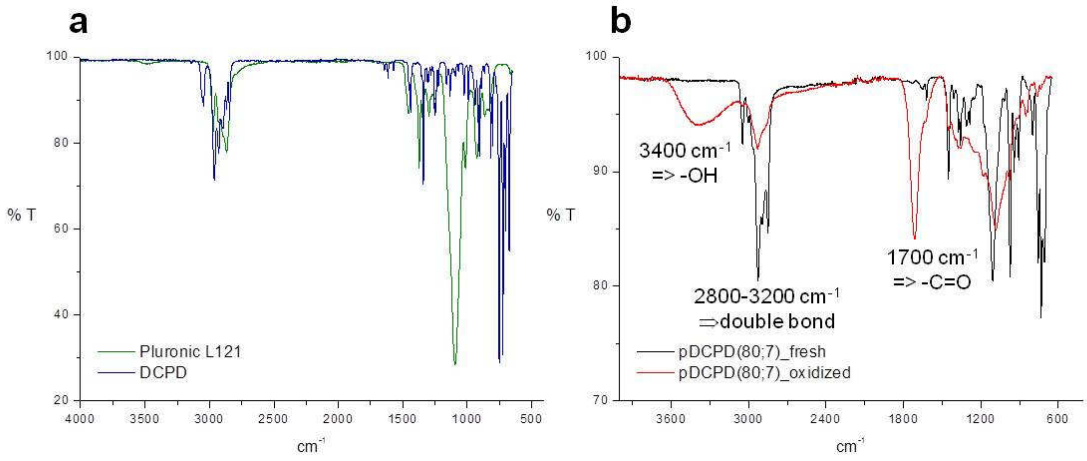

Figure 20: ATR-FTIR measurement of DCPD and surfactant (a) and polymerized pDCPD one day after preparation and oxidized for several days (b)

The oxidation step was important for further processing of the polymer layer as it was found that oxidized samples preserved their porous structure upon pyrolysis. [127]

4.2.1.3 Pyrolysis of pDCPD

During pyrolysis the polymer was converted to carbon while the polyHIPE structure of the polymer was preserved. The oxidation step introduced structural stability during the conversion even at high pyrolysing temperatures of 1400°C. Therefore porous interconnected carbon materials were accessible through an easy soft templating process. The internal water phase was removed prior to carbonization, circumventing the necessity of an additional processing step for template removal, as usual for hard template approaches [132].

As can be seen from the TGA/DSC curves in Figure 21 a mass loss of about 70% was observed when heating the polymer to 700°C which was not further increased when raising the temperature to 1000°C. Mass loss was caused by the thermal decomposition of the polymer during conversion to carbon and the related release of volatile products. According to mass spectroscopy a major contribution to mass loss resulted from the release of CO_2, H_2O, OH^+, O^+ and CH_3^+ groups. Temperatures of 500°C (for 2h) led to the carbonization of pDCPD, while

lower temperatures (400°C, for 2h) led to incomplete conversion as was easily noticeable through dark brown coloration instead of expected black coloration of the resulting sample.

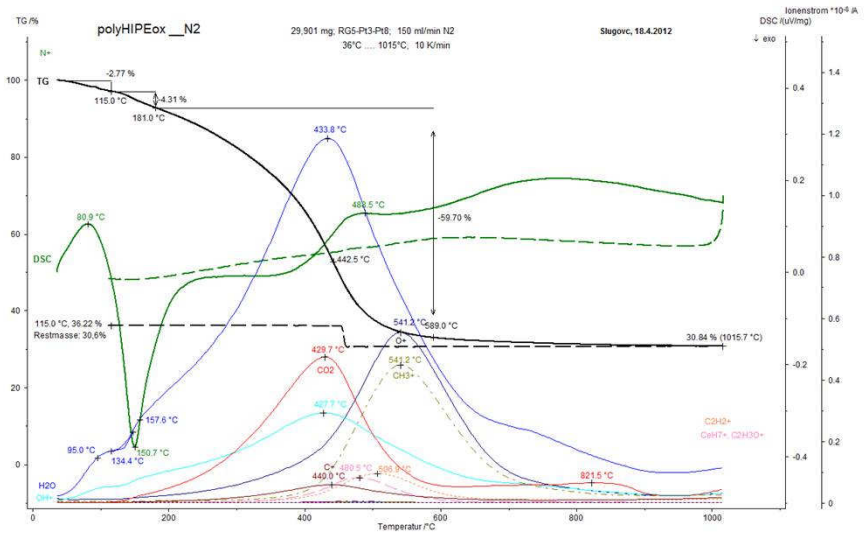

Figure 21: TGA/DSC of oxidized polyDCPD, provided by Kovacic and published in [133]

Polymer-shrinkage during pyrolysis was examined for free standing bulk samples (without metal substrate) of a certain dimension. The volume of bulk samples shrank about 75 v% and 80 v% at pyrolysis temperatures of 500°C and 900°C respectively. Accordingly, decreased pore diameters were observed in cross section analysis as shown in Figure 22, when e.g. comparing a polymer bulk sample of pDCPD(80;7) and the resulting carbonized sample after 900°C. The pore size in dependence of temperature was determined by Kovačič et al.[134]. At 900°C the pore size was determined with 4.3 ±1.6 µm and window size was determined with 1.2±0.6 µm.

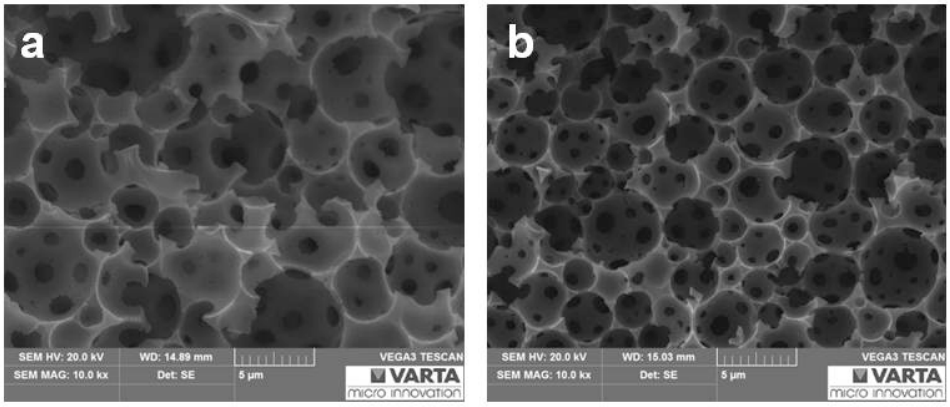

Figure 22: Bulk pieces of oxidized pDCPD(80;7) (a) and pyrolysed at 900°C (b)

Pyrolysis of pDCPD(80;7) on Ni foil

Considering the technological point of view, shrinkage of the polymer film on metal substrate constitutes an additional challenge for the preservation of adhesion of carbon layer to metal substrate current collector. Polymer coated Ni foils had to be pyrolysed at lower temperatures for preserving the adhesion of the carbon film on the metal substrate. For polymer layers of up to 150µm (after polymerization and oxidation) pyrolysis temperatures of 600°C lead to well preserved structures and maintained adhesion to the metal foil substrate. As can be seen from TGA curve in Figure 21, at 600°C the main mass loss due to thermal decomposition of the polymer is completed to a great extent and peak temperatures for the release of different fragments lie below 600°C. A shoulder in the H_2O MS-curve at 700-800°C indicated that at a pyrolysis temperature of 600°C a residue amount of oxygen and hydrogen were present and therefore the conversion to carbon was not fully completed.

However, at higher temperatures (700°C) scale like carbon flakes peeled off the Ni foil substrate and samples were not further useable for preparation of electrodes. The expansion of nickel foil substrate (13.4 $10^{-6}K^{-1}$ at 293°K (20°C) and 16.8 $10^{-6}K^{-1}$ at 800°K (523°C)[135]) in combination with the shrinkage of the polymer layer during enhanced temperatures and contraction of the metal substrate during the subsequent cooling step probably caused the carbon layer to peel off.

SEM images of the surface of a sample with preserved, intact carbon coating and corresponding images of the cross section (obtained from a bulk piece prepared without metal substrate but from the same emulsion) after pyrolysis at 600°C are shown in Figure 23 a) and b). A more open structure of the surface was created due to shrinkage upon transformation of polymer to carbon material. The porous surface allowed for easy melt infiltration of sulfur into the porous carbon coating by spreading elemental sulfur on top of the surface and heating to temperatures (155°C) above the melting point (119.6°C). On the contrary, the open surface may facilitate the diffusion of dissolved PS species out of the cathode region during electrochemical reaction.

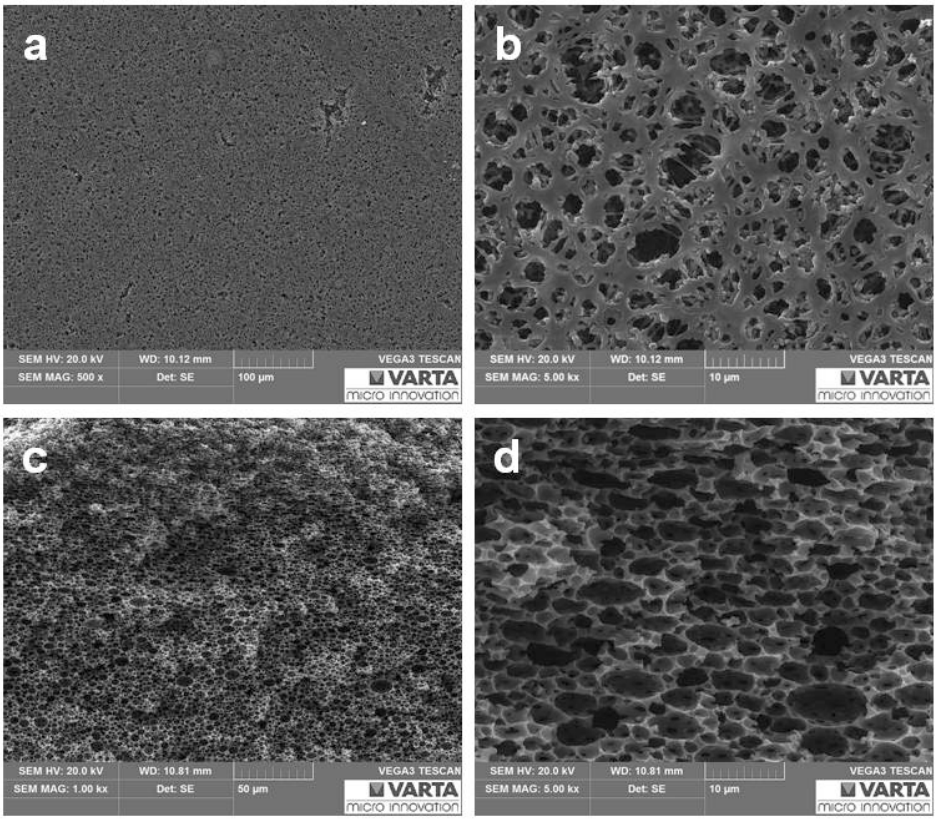

Figure 23: pDCPD(80;7) pyrolysed at 600°C: surface of carbon coating on Ni foil substrate(a,b) and cross section of bulk piece (c,d)

Pyrolysis of pDCPD(80;21) on Ni foil

The adhesion of polymers obtained from emulsions of higher surfactant amount was again lost in case of pyrolysis temperatures of 700°C. Pyrolysis of pDCPD(80;21) thin films on Ni foil substrate at 600°C revealed a significantly different surface morphology than samples of the standard formulation pDCPD(80;7), as can be seen in Figure 24 a and b. As a consequence of shrinkage, the already existing cracks in the polymer surface (as discussed in Figure 19) were now widened and an increased number of cracks became visible. Cracks were the ideal areas for compensation of the tensions inside the material during shrinkage. As can be seen from Figure 19 b the widening of the cracks was progressing until the Ni foil underneath became visible and could also be observed macroscopically. Comparison of the cross sections of bulk samples in high magnification (5 kx) in Figure 23 and Figure 24 revealed a decreased pore diameter for higher surfactant amount.

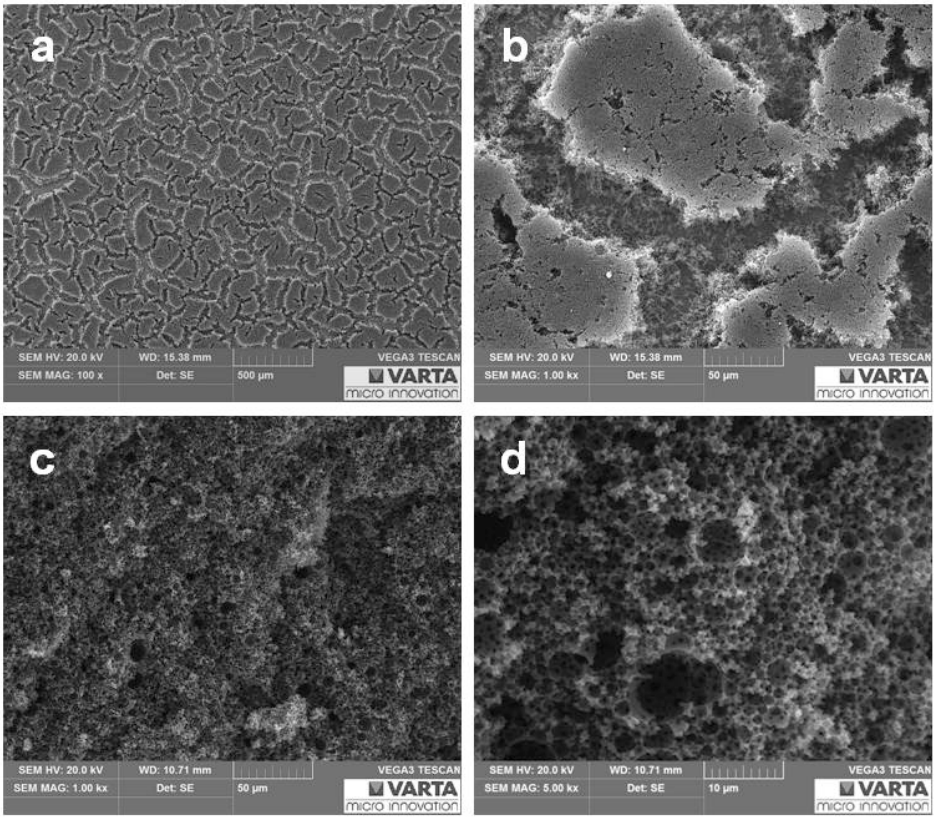

Figure 24: pDCPD(80;21) pyrolysed at 600°C: surface of carbon coating on Ni foil substrate(a,b) and cross section of bulk piece (c,d)

The surface structure of the as prepared sample seemed rather damaged and therefore useless for further processing, nevertheless the material was used for preparation of sulfur electrodes, as the remaining isles of intact material showed good adhesion to the metal substrate.

4.2.1.4 Preparation of HIPE structured carbon layer on Al-, Cu- foil and Ni-mesh

Polymer coated Al-foil, Cu-foil and Ni-mesh substrates within this chapter were provided by Kovacic. Further processing (pyrolysis, electrode preparation and SEM/electrochemical characterization) was performed by the author.

Preparation and pyrolysis of pDCPD(80;7) on Al foil

At the pyrolysis temperature of 600°C the use of aluminum as metal substrate is theoretically possible because the melting point of Al at 660°C (compared to Ni with 1443°C) is lying above the end pyrolysis temperature. The use of Al instead of Ni would come with the advantages of

lower weight (26.98 g/mol of Al vs. 58.69 g/mol) and price (1919 USD/ton Al vs. 13760 USD/ton Ni official LME (London Metal Exchange) prices [136]) caused by the metal foil current collector. However, the use of Al foil as metal substrate resulted in the reaction of the Al surface with reactants from the coating, indicated by a yellow discoloration which appeared during polymerization and oxidation of the polymer layers at 80 °C and 42 °C in regions directly below or adjacent to the polymer coating. Areas far off the coating remained (visibly) unchanged. The surface reaction was proven by EDX measurement, revealing a three-fold oxygen content (and an increased carbon content probably a residue from the removal of the polymer layer) at the Al surface in comparison to the EDX spectrum obtained from a sample area with no visible discoloration (9 w% vs. 27 w% oxygen and 8 w% vs. 14 w% carbon; cf. appendix Table 4, p. 114). Despite the obvious surface reaction, sulfur was melt infiltrated into the carbon structure and the electrochemical performance was tested. However, as expected, the resulting carbon/sulfur electrodes showed no electrochemical activity probably caused by the electrically non-conductive (oxide) layer on top of the metal. Al as substrate was not further investigated.

Preparation and pyrolysis of pDCPD(80;7) on Ni mesh substrate

Furthermore Ni mesh was applied as current collector (Figure 26). In general, the application of mesh current collector brings the advantage of reduced weight and allows for high electrode loadings. [133] The emulsion was casted on Ni mesh and interspaces in between the Ni wires were filled additionally to the continuous layer on top of the mesh. The adhesion of the polymer was preserved after polymerization (cf. Figure 25).

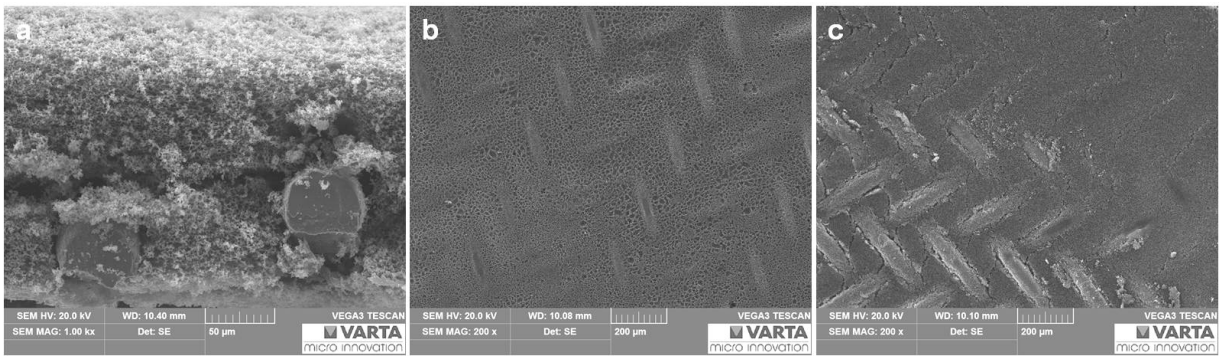

Figure 25: pDCPD(80;7) on Ni mesh in cross section (a), surface in glass contact during polymerization (b) and surface in contact with air during polymerization (c)

Shrinkage during pyrolysis caused partial degradation of the adhesion of the carbon coating on Ni mesh. In areas in which Ni mesh was completely coated by polymer (interspaces filled and

continuous top layer), intact carbon coatings were obtained after pyrolysis while in areas with polymer solely on top of the mesh without penetration to interspaces or vice versa resulted in loss of adhesion or Ni wire getting exposed and scales of carbon layers in between.

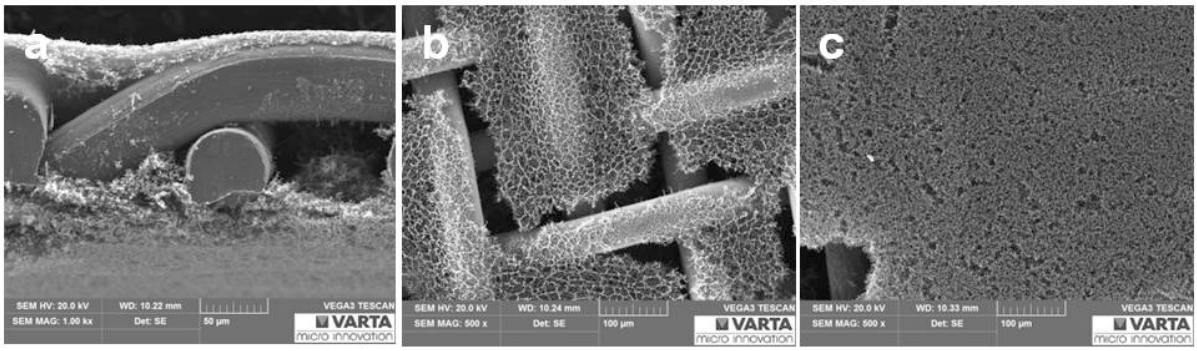

Figure 26: pDCPD(80;7) on Ni mesh pyrolysed at 600°C: in cross section (a), surface of in glass contact during polymerization with exposed Ni wires(b) and surface in contact with air during polymerization (c)

Preparation and pyrolysis of pDCPD(80;7) on Cu foil

The preparation of polymer pDCPD(80;7) coated copper foil substrates and subsequent pyrolysis worked out comparably to Ni foil substrates at pyrolysis temperatures of 600°C and showed comparable surface structures.

4.2.1.5 Investigation of electric conductivity of carbon materials obtained from pyrolysed pDCPD-HIPE materials

An important factor concerning the suitability of the obtained carbon materials as sulfur host is their electrical conductivity. Carbonized bulk samples (without metal substrate) were analyzed applying four point probe method. The determination of electrical conductivity of the carbon films on metal substrates by this method was not possible, because the applied current would have passed through the material with lower resistivity and therefore through the metal substrate. Electrical conductivity was measured in dependence of pyrolysis temperature at 500°C, 700°C, 900°C, 1100°C and 1400°C. Results are depicted in Figure 27. At 500°C no value for electrical conductivity could be obtained probably because of too low conductivity and too low sensitivity of the measurement set up.

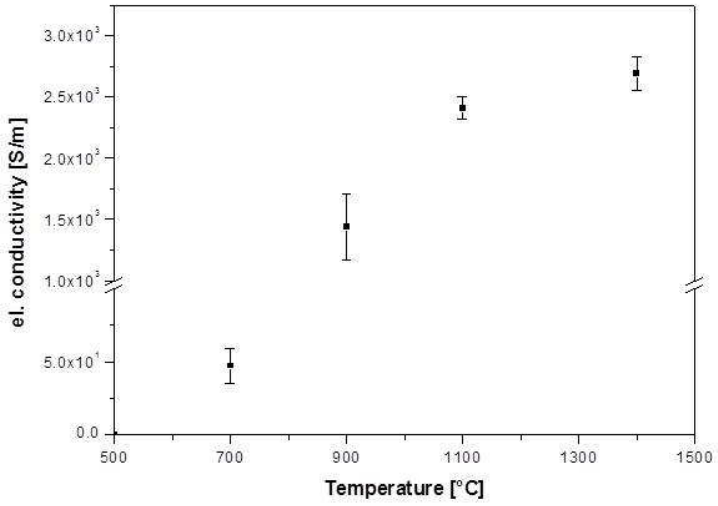

Figure 27: Electrical conductivity of pDCPD(80;7) derived HIPE structured carbon samples pyrolysed at different temperatures

Variations in the obtained electrical conductivity values were probably caused by inhomogeneous dimension of the carbonized stick-samples (bubbles during polymerization leaving holes in the sample, inaccuracies in dimensions etc.) as indicated by error bars. The electrical conductivity was determined at 700°C and was about 50 S/m±10 S/m and could not be determined for 500°C; the value for 600°C was assumed to lie in between. At higher temperatures such as 1100°C the obtained electrical conductivity was as high as $2.40*10^3$ S/m±90 S/m.

An increase in electrical conductivity was observed with increased pyrolysis temperature. This trend was in accordance with additional characterizations in terms of TEM and EELS measurements performed by Kovačič et al. [134] and was ascribed to the increased ordering of carbon and a higher degree of graphitization upon higher pyrolysis temperature.

For electrode preparation, a temperature of 600°C was found to be the upper temperature resulting in useable carbon layers on metal substrates. Despite the considerably low electrical conductivity values at low pyrolysis temperatures (≤700°C) the (following) electrochemical measurements revealed working carbon/sulfur electrodes with reasonable sulfur utilization. Therefore it might be suggested that carbon layers on metal electrodes reveal higher electrical conductivities than it was the case for bulk samples.

4.2.2 Electrochemical investigation of HIPE structured carbon/sulfur electrodes

Electrochemical performance of pDCPD(80;7) derived carbon/ sulfur electrodes on Ni foil

Carbonized pDCPD(80;7) on Ni metal foils were infiltrated with sulfur in a weight ratio of ~46 w% and 60 w% with regard to carbon loading. It has to be noted that the electrode loadings of the obtained electrodes were rather small, due to small residue amount of carbon after ~70 w% mass loss during pyrolysis. The resulting sulfur loadings were 0.44 mg/cm^2 and 0.74 mg/cm^2 corresponding to a sulfur ratio of 46 w% and 60 w% respectively. With a porosity of ~80 v% (resulting from 80 v% internal phase in the initial HIPE) and an average thickness of ~22 µm of the carbon layer (for the considered measurements in Figure 28), a sulfur loading of 3.6 mg/cm^2 would have corresponded to the complete sulfur filling of the carbon pores. The BET surface areas of for samples pyrolysed at 500°C and 700°C were determined with 2.5 m^2/g and 3.1 m^2/g respectively. The corresponding cavity sizes were determined with 4.2±1.2 µm and 4.6±1.6µm and window sizes of 1.5±0.9 µm and 2.1±0.9 µm. BET surface and pore sizes determined by Kovačič et al. [134] for bulk samples without Ni substrates.

The densities of the sulfur electrodes were about 0.43 g/cm^3 and 0.57 g/cm^3 for the two different sulfur ratios. The galvanostatic cycling experiments were conducted in pouch cells, applying 14 µl electrolyte per mg of sulfur (14 µl/mgS) and an excess of lithium. Results for 46 w% and 60 w% sulfur are depicted in Figure 28.

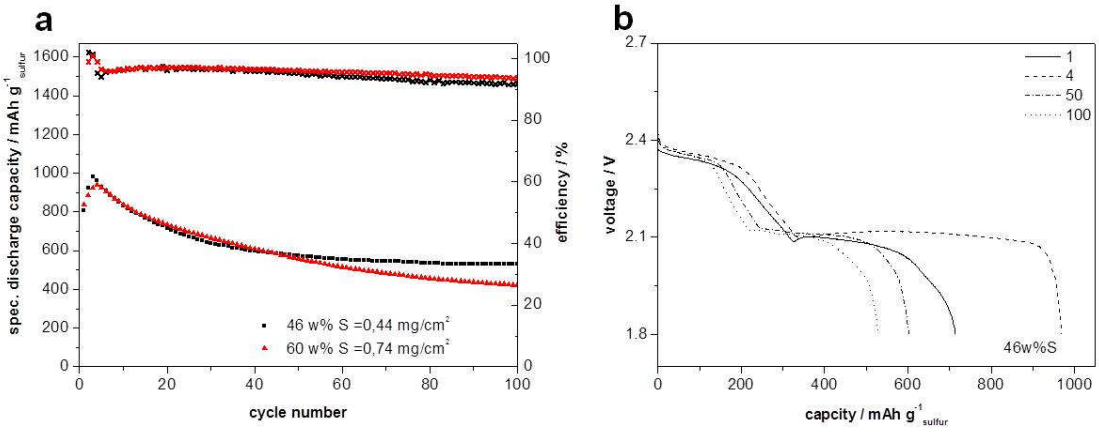

Figure 28: Cycle performance of pDCPD(80;7) derived sulfur electrodes with 46 w% and 60 w% sulfur (a) and corresponding voltage profile of 1st, 4th, 50th, 100th cycle for 46w% sample(b)

As can be seen in Figure 28 a, the initial capacities of pDCPD(80;7) derived sulfur electrodes were in the range of 800 mAh/g, irrespective of higher or lower sulfur loadings. A comparable ratio of sulfur was electrochemically accessible. During the first four cycles an increase in capacity was observed which was very likely caused by the repeated dissolution and precipitation processes occurring during charge and discharge. The rearrangement of sulfur during the first cycles led to higher sulfur utilization in the subsequent cycles. As can be seen from Figure 28 b the initial rise in capacity could mainly be attributed to the elongation of the second discharge plateau, corresponding to the reduction of low order polysulfides to Li_2S_2 and Li_2S. Probably the diffusion of well soluble PS species to initially unused regions of the carbon matrix increased the accessibility of created long chain PS species for further (complete) reduction. Moreover it can be seen from Figure 28 b that cathode polarization decreased within the first four cycles, resulting in slightly higher reduction voltages at the upper and the lower voltage plateau. During the first charge-discharge cycles the coulombic efficiency exceeded 100% because of the gradually increasing amount of sulfur species that got accessible due to rearrangement. CE levelled off to 96-97% and to 90% after 100 cycles probably due to the continuous consumption of $LiNO_3$.

Considering the specific capacity of sulfur after the initial rise, values of ~1000 mAh/g and 940 mAh/g were obtained for 46 w%S and 60 w%S samples (Figure 29).

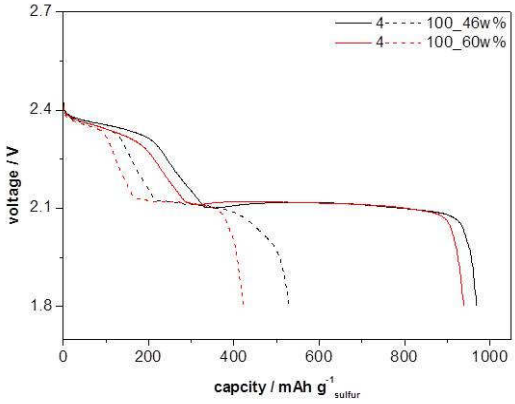

Figure 29: Voltage profile of 4th and 100th cycle of pDCPD(80,7) with 46 w% and 60 w% sulfur

Decreased capacity retention in case of higher ratio was probably caused by an increased amount of insulating Li_2S deposits at the cathode surface. The precipitated Li_2S layers probably isolated the remaining sulfur species from reaction sites at the carbon surface which led to more

incomplete utilization. This statement was supported by the relatively higher decrease in capacity caused by the second discharge plateau over 100 cycles of galvanostatic charging/discharging.

Electrochemical performance of pDCPD(80;7) derived carbon/ sulfur electrodes on Ni mesh

Higher polymer and hence, higher carbon loadings were obtained for Ni mesh substrates. During preparation the emulsion filled up the space between the Ni wires and additionally was present as continuous layer on top of the mesh. A comparable loading at metal foil substrates resulted in the polymer layer to peel off during polymerization or pyrolysis. The carbon to sulfur ratio was adjusted to 47w% (comparable to 46w% from previous samples) but resulted in higher absolute sulfur loadings per cm^2 (47 w%S = 1.5 mgS/cm^2). The cycling performance of pDCPD(80;7) derived sulfur electrode on Ni mesh substrate is depicted in Figure 30.

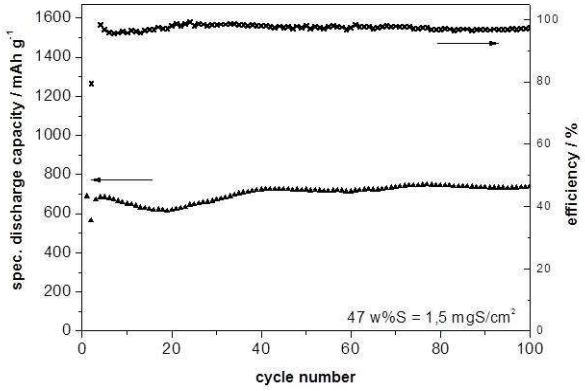

Figure 30: Cycle performance of pDCPD(80;7) derived sulfur electrodes with 46 w% on Ni mesh

The initial specific capacity was about 700 mAh/g considering the mass of sulfur. While the obtained capacity was beneath the capacity of previously discussed samples (with lower absolute sulfur loadings per square centimetre on Ni foil (cf. Figure 28)), the capacity retention was improved over 100 cycles and a specific sulfur capacity of 740 mAh/g was obtained. The shape of the curve suggested that initially not utilized active material got accessible during cycling and buffered the continuous capacity loss.

However, the results were obtained with lower electrolyte amount of 8 µl/mgS and therefore better capacity retention was probably partially caused by decreased electrolyte volume.

Electrochemical performance of pDCPD(80;21) derived carbon/ sulfur electrodes on Ni foil

Carbon/sulfur electrodes obtained from pDCPD(80;21) revealed superior performance in comparison to the pDCPD(80;7) in terms of cycling stability (Figure 31). As shown in Figure 19 and Figure 24 a the higher surfactant amount resulted in smaller voids, while at the same time undesired cracks were generated which resulted in uncovered electrode areas after shrinkage during carbonization. Nevertheless, obtained samples were further processed to sulfur electrodes and showed promising results as shown in Figure 31 a.

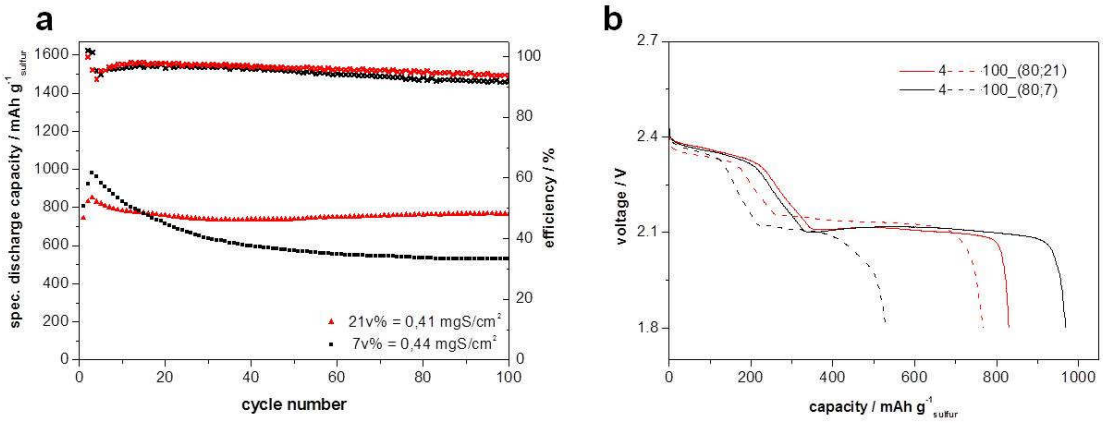

Figure 31: Cycle performance of pDCPD(80;21) in comparison to pDCPD(80;7) derived sulfur electrodes with 46 w% (a) and voltage profile of 4th and 100th cycle (b) of both samples

A less pronounced rise in capacity during the first three to four cycles can be attributed to good initial sulfur distribution and easy accessibility of electrolyte to all electrodes regions through the channels generated by the cracks. The lower initial specific capacity of sulfur may be caused by the partially damaged surface of the electrodes by cracks and the creation of electrode areas of less sulfur utilization. However, at the same time lower decrease in discharge capacity over 100 cycles was observed. After 100 cycles the capacity was 91.4% of the capacity obtained in the forth cycle and CE was about 93%.

Increased capacity retention may be attributed to improved retention of dissolved polysulfides in the smaller pores (=higher carbon surface), as can be seen in the slightly less pronounced capacity decrease in the upper voltage plateau in Figure 31 b. However the major contribution to

capacity after 100 cycles was caused by the second voltage plateau. Smaller pores resulting from the higher surfactant amount, offered higher electrically conducting surface area for redox reaction of PS species. Although some inactive Li_2S deposits might have been generated over prolonged cycling, the point at which the carbon surface got covered by insulating solid Li_2S_2 and Li_2S and prohibited further reduction reaction of PS at an early stage is less probably in case of higher available carbon surface.

Electrochemical performance of pDCPD(80;10) derived carbon/ sulfur electrodes on Cu foil

Cyclovoltammetric measurements of pDCPD(80;10) (with slightly higher surfactant amount than standard formulation) derived sulfur electrodes applying Cu metal foil as substrate showed typical sulfur reduction peaks at ~2.3 V and ~2.1 V and oxidation peak at ~2.4 V-2.5 V respectively in the first cycle (cf. Figure 32 black curve). However, in the second cycle an additional reduction peak at ~1.6 V occurred together with an additional oxidation peak at ~1.8 V (cf. Figure 32 red curve). While newly evolved peaks increased, the typical sulfur redox peaks at 2.3 V and 2.4-2.5 V for reduction and oxidation respectively diminished (Figure 32). Comparing to literature [137] [138], the in situ generation of CuS was very likely the reason for the observed behaviour. An electrolyte without $LiNO_3$ was applied, due to the fact that the lower cut off voltages were set to 1.0 V and 1.5 V vs. Li/Li^+ for potentiostatic and galvanostatic measurements respectively. This would have caused the early decomposition of $LiNO_3$.[107]

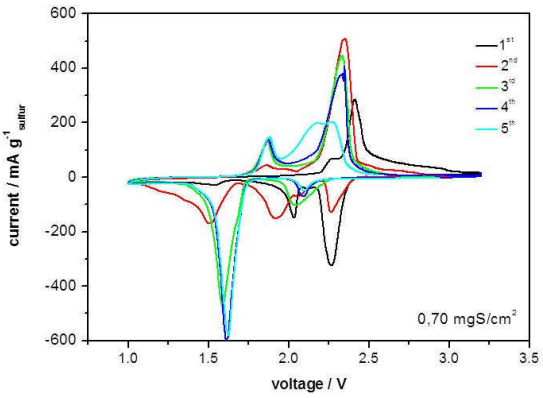

Figure 32: Current voltage curve of pDCPD(80;10) derived cells with Cu metal substrate

Subsequent galvanostatic cycling of pDCPD(80;10) derived electrodes on Cu substrate was performed within a broader voltage range of 1.5 V – 3.2 V for 50 cycles than typically applied for

galvanostatic measurements and was conducted directly after CV experiment (the curve in Figure 33 a therefore starts at the sixth cycle).

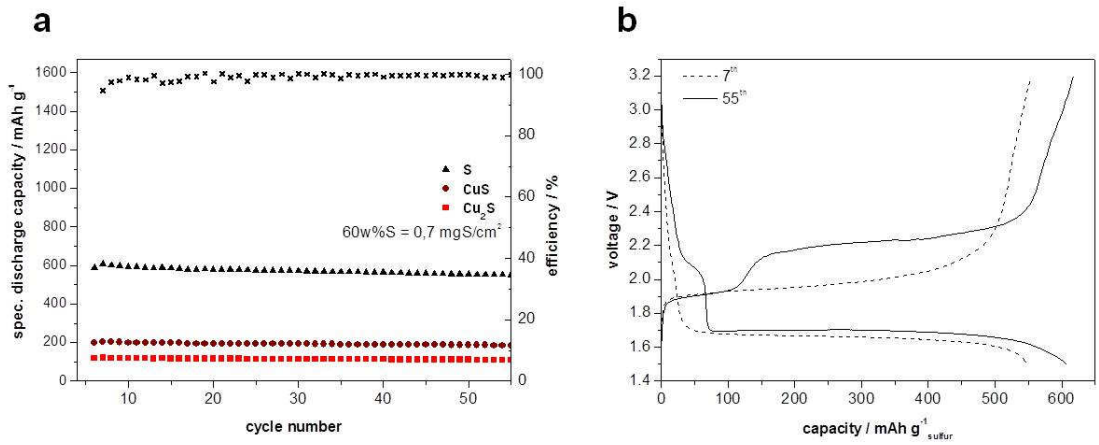

Figure 33: Cycle performance of pDCPD(80;7) on Cu foil substrate starting after 5 cycles CV (a) and voltage profile at 7th and 50th cycle capacity based on mass of sulfur(b)

The cycling behaviour is depicted in Figure 33 a and showed the specific capacity calculated on mass of sulfur and mass of CuS and Cu_2S respectively. The amount of theoretically possible in-situ generated CuS and Cu_2S was calculated based on the amount of initial sulfur loading of 0.70 mg/cm^2. A stable cycling performance with only minor capacity loss over 50 cycles and a capacity retention of ~90 % in comparison to the fifth cycle was obtained. Considering solely the applied mass of sulfur in specific capacity calculation (as CuS is generated in situ from reaction with the current collector and therefore no additional mass was added in electrode preparation) a stable value of 600 mAh/g was obtained. Calculation based on CuS and Cu_2S led to 200 mAh/g and 120 mAh/g respectively. The C-rate for galvanostatic cycling was based on specific sulfur capacity (1672 mAh/g) and therefore the applied C-rate of 0.1 C translated to 0.3C for CuS (560 mAh/g). As can be seen in Figure 33 b, the discharge plateau at ~2.1 V and the corresponding charge plateau at 2.2 V vanished during repeated charge and discharge, while the plateaus at 1.7 V and 1.9 V for reduction and oxidation respectively were elongated.

The electrochemical behaviour CuS and Cu_2S in LiTFSI-DOL-DME electrolyte system, discussed in [138], matched the observed evolution of the discharge and charge plateaus in the depicted voltage profile in Figure 33 b quite well. It was concluded that CuS was initially generated in-situ through (chemical) reaction of Cu current collector and polysulfides during charge and discharge of the Cu/S electrode in the DME/DOL based electrolyte. The voltage

plateaus matched the theoretically calculated plateaus for the reduction of CuS to the intermediate of Cu_2S at 2.14 V and further reduction to Cu and Li_2S at 1.78 V respectively.

$$\boldsymbol{CuS + Li^+ + e^- \leftrightarrow 0.5Cu_2S + 0.5Li_2S} \qquad \textbf{Eq. 32}$$

$$\boldsymbol{0.5Cu_2S + Li^+ + e^- \leftrightarrow Cu + 0.5Li_2S} \qquad \textbf{Eq. 33}$$

In subsequent cycles however, the voltage plateaus (at ~2.1 V and ~2.2 V for discharge and charge respectively) caused by reaction in Eq. 32 vanished and the redox reaction mainly occurred between Cu_2S and Cu + Li_2S as the formation of CuS was kinetically less favoured.[138] Coulombic efficiency increased from initial 97-98 % to 99 % upon diminishing of the upper voltage plateaus. Initially observed sulfur reduction peaks completely disappeared and probably sulfur active material and corresponding dissolved polysulfide species were converted to copper sulfide species. The fact that no $LiNO_3$ was present to suppress the PS shuttle further evidenced the missing sulfur redox reaction.

Despite the advantage of high coulombic efficiency and capacity retention of the as prepared electrodes, the conversion to CuS reduced the average discharge voltage in comparison to sulfur active material and would therefore decrease energy density in the resulting cells. Theoretical specific energy densities of 961 Wh/kg and 552 Wh/kg[138] would be available for CuS and Cu_2S based copper sulfide-lithium cells.

4.2.3 Conclusion and outlook

Porous carbon material derived from pDCPD through ROMP of high internal phase emulsion and subsequent oxidation and pyrolysis was evaluated with regard to its suitability as sulfur host in carbon sulfur electrodes. These investigations were carried out in collaboration with Kovačič and treated one of several possible applications of HIPE-structured pDCPD derived materials in batteries. In this context, the potential application of pDCPD material as separator in LIBs [139], as current collector after metal deposition [131] and as carbon precursor for carbon coated silicon particles in negative electrodes [133] were evaluated.

In general it can be concluded, that the feasibility of the described procedure was shown and states a cheap and easily scalable process for the preparation of sulfur electrodes. A polymer coating on metal substrate and the conversion to carbon material via pyrolysis was realized

without the loss of adhesion. The main advantages of such electrodes lie in the combined production of carbon material and electrode preparation and in the cheap carbon precursor compound.

Interestingly, despite the low surface area of the here applied carbon structure between 2.5 m^2/g and 3.1 m^2/g (cf. 4.2.1.5, p. 62) in comparison to most carbon structures discussed in literature (which show values in the magnitude of several hundreds of m^2/g) and despite the low electrical conductivity of the pryrolysed materials, sulfur utilization of 42% was obtained at a moderate sulfur loading of 1.5 mgS/cm^2 and 46 w% sulfur ratio. Due to macro porosity, electrolyte could easily penetrate into all regions of the carbon/sulfur electrode. Further it is likely, that due to the prohibited Li_2S induced pore clogging in the macroporous channels, electrolyte access throughout the electrode was maintained over prolonged cycling.

Nevertheless there is certainly room for improvement. A main challenge was the production of polymer membranes with constant quality. The inner structure of the polymer coatings as well as the adhesion of carbon layers on the metal substrate varied and made the comparison of differently prepared samples more difficult. The application of Ni-mesh as metal substrate showed that the mass loading per square centimetre could be increased which is an important factor for achieving higher energy densities in resulting Li-S cells. However sulfur loading and utilization have to be further increased. In this regard, smaller pore size distribution would be favourable for improved sulfur utilization and dissolved PS species confinement. First investigations in pore size tuning by simply applying an ultrasonic nozzle during HIPE preparation, however, resulted in phase separated samples which lost the typical HIPE structure. Moreover, positive electrodes had to be prepared on Ni-foils because chemical reactions prohibited the use of light weight Al or cheaper Cu current collector foils. In this context the evaluation of carbon coated Al foils would be interesting. First tests were conducted and showed an improvement to plane Al foils, where the electrochemical redox reaction was completely prohibited due to creation of an insulating layer. Further steps could include tests with increased carbon coating thicknesses to further prevent the surface reaction with Al. The use of Cu current collector foil resulted in the in-situ generation of CuS/Cu_2S and showed stable cycling but lower average discharge potentials which would diminish the obtainable energy density.

The shown preparation route was feasible only at reduced pyrolysis temperature, which stated a tradeoff between electrical conductivity and preserved adhesion. Especially at higher current loads, problems related to the poor electrical conductivity, like increased polarization, will be enhanced. In this context the influence of different heating rates on the adhesion may bring

improvement for preserved adhesion at higher temperatures. The heating and cooling rate were kept constant for all experiments, guaranteeing comparability of the samples of different formulations and on different substrates. However it is a well known fact, that heating rates can influence the rate of gas evolution during thermal degradation of the polymer and hence the formation of pores in the carbon material. Applying slower heating rates (lower than 4 °C/min) could lead to the creation of smaller pores (also at the metal-carbon interphase) and reduce distortions during pyrolysis step which may positively influence adhesion on the metal substrates during pyrolysis. [140]

It can be concluded that at the current state of development the material would not be competitive to conventionally prepared sulfur electrodes from commercial carbons by slurry technique, due to the above discussed drawbacks (e.g. low material loading and sulfur utilization). However, the listed measures may lead to improved HIPE-structured pDCPD derived carbon coated metal substrates and therefore improve the suitability for use in sulfur electrodes.

4.3 Considerations on lithium metal negative electrodes in Li-S cells

With regard to its specific energy density and specific capacity, lithium is the most promising choice as negative electrode material. With the use of lithium in Li-S cells, full advantage can be taken of the high specific capacity of sulfur as active material. However, as discussed in chapter 2.4 (p. 26), the major drawbacks come along with the application of metallic lithium in rechargeable cells. Dendritic lithium growth can result in short circuits after prolonged cycling. Heat evolution in the shorted cell can impose serious safety issues like thermal runaway. The generation of *dead* lithium may cause poor coulombic efficiencies and severe capacity fading at the negative electrode.

In the following section the behaviour of lithium during galvanostatic charge and discharge experiments is investigated. In this context, the lithium polarization was monitored against Li reference electrode (RE_{Li}) and the evolution of the lithium surface was observed via SEM. The results clearly reflect the challenges which prevent Li-S technology from commercialization until now.

4.3.1 Li metal electrode polarization during galvanostatic cycling of Li-S cells

Through implementation of a Li reference electrode in pouch cells, single electrode potentials of positive and negative electrodes were monitored additionally to the cell voltage during cycling. This cell set up was chosen to monitor the evolution of the lithium electrode potential and hence the polarization during galvanostatic measurements. The influence of different lithium to sulfur capacity ratios on the cycling performance of Li-S cells was investigated.

Galvanostatic cycling experiments were conducted in full cell configuration (cf. chapter 3.2.5). Physical vapour deposited (PVD) lithium coated copper foils with lithium coatings of 5 µm and 15 µm and a foil of 230 µm without Cu copper foil were applied. The latter will be referred to as bulk Li foil in the following discussion. The copper foil (13 µm) increased mechanical strength and allowed handling of thin lithium layers. The lithium coatings of different thicknesses corresponded to areal capacities of 1.0 mAh/cm^2 and 3.1 mAh/cm^2 and 46 mAh/cm^2 in case of the bulk lithium. A sulfur electrode with a theoretical areal capacity of 1.5 mAh/cm^2 and practical areal capacity of 0.75 mAh/cm^2 was combined with the lithium coated copper foils of different capacities. The applied current density was 0.15 mA/cm^2. The standard parameters (defined in

3.2.5, p.45) were applied for the galvanostatic measurement. Table 3 summarizes the applied capacity ratios of negative and positive electrodes in performed experiments.

Li [µm]	theoretical capacity of Li [mAh/cm^2]	theoretical capacity of C/S-electrode [mAh/cm^2]	practical capacity of C/S-electrode [mAh/cm^2]	Li : S capacity ratio theoretical	Li:S capacity ratio practical
5	1.0	1.5	0.75	0.67	1.3
15	3.1	1.5	0.75	2.0	4.1
230	46	1.5	0.75	31	61

Table 3: Layout and balancing of negative and positive electrodes for investigation of electrode and cell polarization

Figure 34 depicts the cycle performance of cells with 1.3-fold (a) and 4.1-fold (b) lithium to sulfur capacity ratio (considering theoretical Li capacity and practically obtained sulfur capacity). Due to utilization of only half of the available sulfur at the positive electrode, lithium was still overbalanced in terms of capacity.

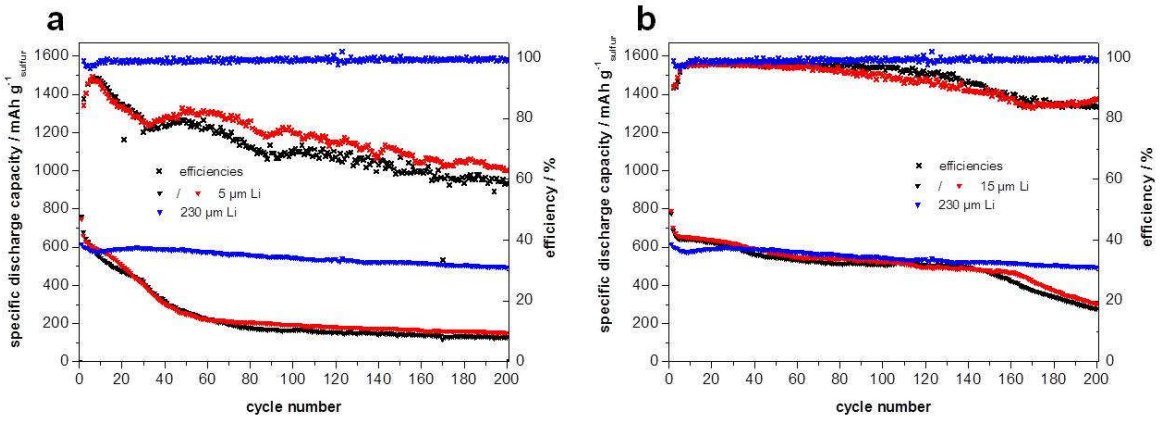

Figure 34: Cycle performance of Li-S cells with (a) 5µm Li or 1.3-fold practical Li:S capacity ratio and (b) 15µm Li or 4.1-fold practical Li:S capacity ratio in comparison to 230µm (blue)

Irrespective of the applied lithium amounts (1.3-fold vs. 4.1-fold) initial sulfur discharge capacities of 800 mAh/g were obtained and these values were comparable to initial discharge capacities obtained in cells with bulk lithium of 230 µm. The black and red curves depicted in Figure 34 are the results of repeated measurements. Therefore it was confirmed that initially

lithium capacity was not limiting cell performances in the discussed cells. The discharge capacity quickly faded to values below 200 mAh/g within 60 cycles in case of the 5 µm PVD-Li electrodes. The coulombic efficiency (CE) in the first cycle was 84% and increased within the first eight cycles to reach a maximum of 92% and declined afterwards to 60% after 200 cycles.

In case of higher lithium to sulfur capacity ratio (4.1-fold, practical) in Figure 34 b, the discharge capacity of sulfur declined more moderate to a value of 570 mAh/g and reached a value of 350 mAh/g after 200 cycles. The CE stabilized between 97% and 98% after an initial raise for 60 cycles and continuously declined from the 60th cycle onwards. For comparison, a Li-S cell applying huge excess of lithium (bulk lithium of 230 µm) showed a more stable CE and specific discharge capacity of sulfur of 99% and ~500 mAh/g respectively after 200 cycles (Figure 34 b blue curve).

The CE of cells with limited amount of Li showed a very poor CE from the beginning. The quality of deposited lithium and a poor mechanical, electrical connection may partially impede the utilization of loosely deposited lithium in following discharge cycle and decrease CE. Chemical reaction of polysulfides (PS) species could proceed unhindered during charging step and further decreased CE. In cells with higher lithium excess a lithium buffer was available compensating lithium losses. Cells with low lithium loading, on the contrary, reflected the deterioration of the negative electrode which caused poor CE and limited cell capacity. CE in Li-S cells is heavily influenced by $LiNO_3$ which suppresses the PS shuttle (cf. Figure 11), but is consumed during repeated stripping and plating of lithium and the generation of fresh lithium surface.[107] An increased lithium surface leads to increased reaction of electrolyte and lithium and causes the early consumption of $LiNO_3$ which decreases CE, as was observed in the cycling behaviour of cells depicted in Figure 34 b after 160 cycles.

Further it is a well known fact that the application of moderate pressure during cycling of metallic lithium electrodes leads to more compacted lithium deposition and therefore enhances the cycling efficiency.[80] At the time of performing the described measurements, no vacuum sealing device was available for sealing the pouch cells. For exclusion of gaseous electrolyte decomposition products and Ar bubbles from in between the electrode stack and for preserving the contact of electrodes and separator, pressure was applied during measurement by using jigs. Deviations in the applied pressure between single cells could have influenced the measurements. Moreover, inhomogeneous pressure on the electrode stack within a single cell could result in an inhomogeneous reaction at lithium (and sulfur) electrodes.

Electrode potentials of positive and negative electrodes vs. RE_{Li} during galvanostatic cycling experiments were monitored (Figure 35). The blue lines indicate the cell voltage with the cut off voltages set at 2.6 V and 1.8 V.

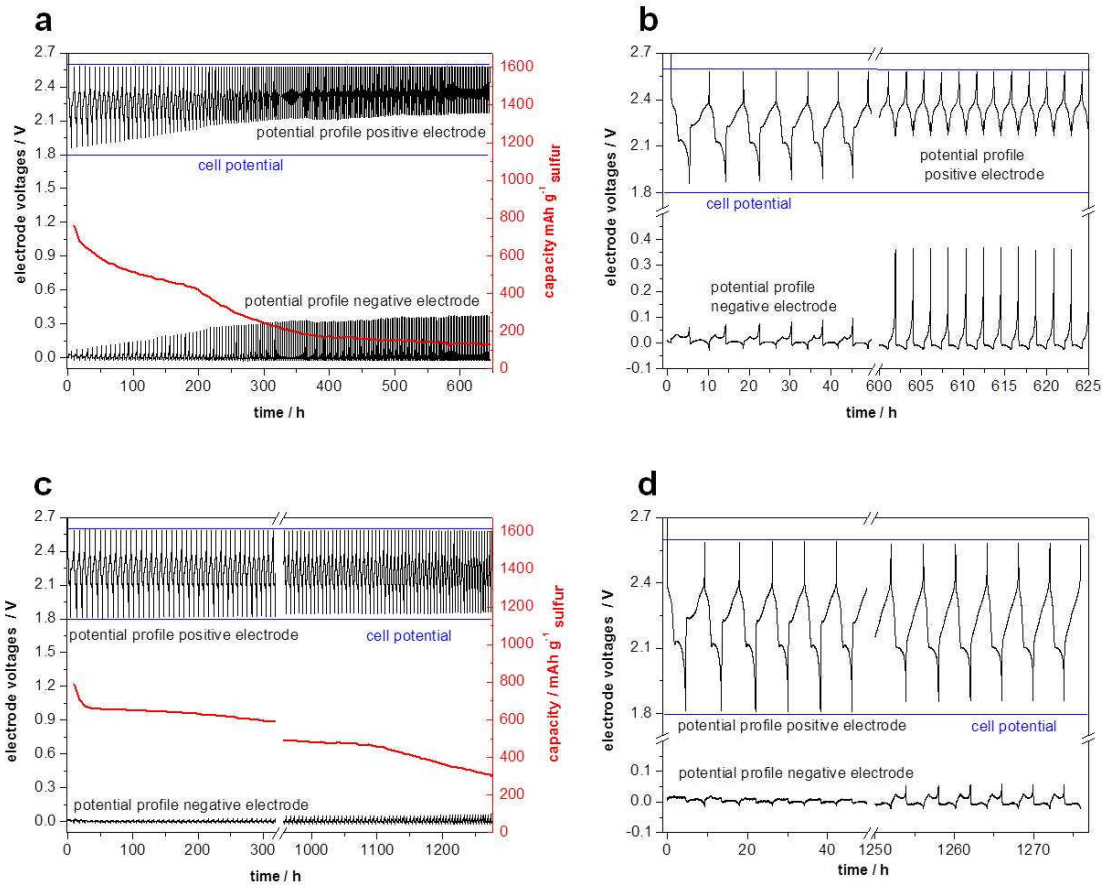

Figure 35: Voltage profiles of positive and negative electrodes of Li-S cells controlled via cell voltage with (practical) Li:S ratio of 1.3 (a and b) and 4.1 (c and d)

Increasing polarization of the negative electrode occurred upon repeated cycling and was particularly distinct in case of low negative electrode capacity (1.3-fold Li capacity, practical). A flat plateau for stripping (at positive potential vs. RE_{Li}) and plating (negative potential vs. RE_{Li}) with only minor deviation of the lithium potential from 0 V would be expected for lithium dissolution and precipitation.

Considering the potential profile of Li electrode, a sharp increase was observed at the end of each stripping process (lithium potential raised to ~350 mV vs. Li/Li^+ at stripping process) while this behaviour was not observed for plating process.

Minor lithium excess and irreversibly consumed lithium, which decreased the available lithium amount in the cell, resulted in the raise of lithium potential and limited cell capacity with increasing cycle number. In case of lithium stripping at the negative electrode, sulfur was reduced to PS at the positive electrode. When all electrically available lithium was dissolved, the potential of the negative electrode raised until the cut off voltage of the cell was reached. At this point, the reduction reactions at the positive electrode may not have been completed and therefore positive electrode potential was not approaching the fully discharged voltage of 1.8 V vs. Li/Li^+. On the contrary, when lithium was deposited at the negative electrode and therefore PS species were oxidized to sulfur, the potential of the sulfur electrode approached the 2.6 V vs. Li/Li^+ of the fully charged state. In this case the cut off voltage of the cell was reached without major deviations of the lithium potential.

In case of the four-fold (practical) lithium capacity excess the polarization was less distinct and the voltage profile showed the expected shape within in the initial cycles (lithium potential raised to ~50 mV during stripping process). The observed increase in electrode polarization was probably due to deterioration of lithium surface and compactness.

While the use of limited lithium amount in Li-S cells reflected the influence of poor lithium cycling efficiency on lithium capacity fading (satisfying initial capacity but fast capacity fading in the first cycles), the application of lithium excess reflected the influence of lithium deterioration on negative electrode polarization. Increased polarization due to precipitated Li_2S_2 and Li_2S[82] and dendritic surface structure[100] may be the cause for this behaviour.

After cycling, the cells were opened and revealed inhomogeneous reacted lithium surfaces. Interestingly no creation of copper sulfides was observed when applying Cu current collector at the negative electrode (a dark blue to black discoloration of the copper foil would have indicated a reaction) in comparison to application of Cu on the positive electrode (cf. chapter 4.2.2). Probably, no chemical reaction of Cu and PS species occurred at the negative potential of the lithium electrode, as long as lithium was available at the electrode to react with.

For Li-S cells lithium excess is necessary to buffer capacity loss and keep polarization low. The factor of necessary lithium excess has to be determined individually in dependence of positive electrode material and cycling conditions and will vary with the amount of plated and stripped lithium in each cycle. Irrespective of the used lithium amount the consumption of electrolyte will proceed upon cycling and limit the cell performance to a restricted number of cycles. The electrolyte amount and amount of charge plated and stripped within one cycle will determine the number of achievable cycles besides the performance of the sulfur electrode performance.

A lithium surface deterioration (structural and chemical) was mentioned before as possible reason for increased electrode polarization and poor cycling efficiency over prolonged galvanostatic cycling. To gain a better understanding of the obtained electrochemical data, a SEM study on the surface structure evolution of lithium metal was performed. These results are discussed in the following chapter.

4.3.2 SEM investigation of Li metal electrode surface morphology during galvanostatic cycling

The SEM investigation of a PVD-Li electrode surface after 200 cycles in a Li-S cell (corresponding to the measurements shown in Figure 34 b and Figure 35 c,d) revealed a heavily deteriorated surface structure. Further, a more basic study of lithium surface evolution was performed including the investigation of lithium surface at different SOCs and in dependence of current load.

4.3.2.1 Surface morphology of the Li metal electrode after prolonged cycling in Li-S cell

The following Figure 36 shows the surface morphology of a PVD-Li (15 µm) electrode after 200 cycles at a current density of 0.15 mA/cm^2 and stripping or plating a total amount of charge in each half cycle of theoretically 1.5 mAh/cm^2 (practically ~0.75 mAh/cm^2). The corresponding cycling performance is shown in Figure 34 b. SEM investigation was performed at charged state. Comparison to the pristine PVD-Li surface (Figure 46) clearly demonstrated the surface deterioration during the cycling experiment.

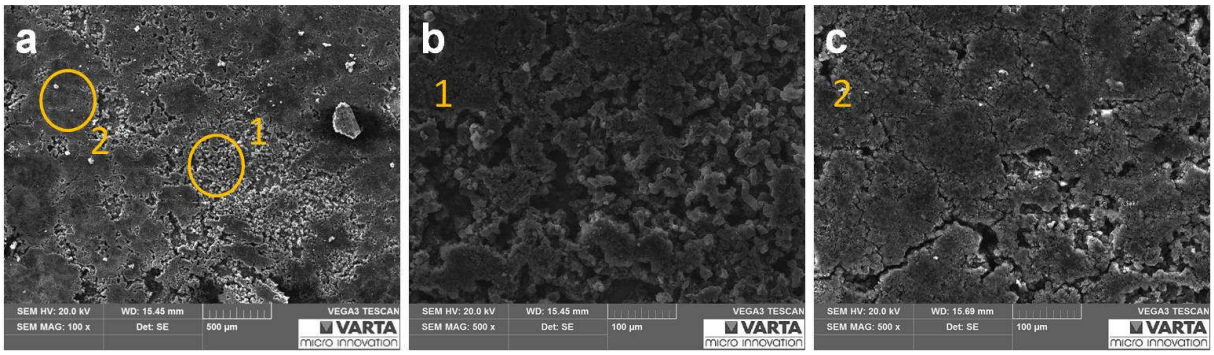

Figure 36: PVD-Li (15 µm) surface after 200 cycles at a current load of 0.15 mA/cm^2 and theoretical 1.5 mAh/cm^2 total charge amount stripped and plated per cycle at (a) 100x magnification and at (b and c) 500 x magnification

The surface of the lithium electrode cycled for 200 cycles clearly revealed an inhomogeneous appearance. Zones of columnar lithium, marked with a yellow circle 1 in Figure 36 a and magnified in Figure 36 b, were formed next to more densely packed areas, marked with yellow circle 2 in Figure 36 a and magnified in Figure 36 c, of less surface structuring. The revealed surface was cracked and in some areas the Cu current collector beneath got visible. Probably different pressure distribution during cycling experiment caused the different appearance, with densely deposited zones resulting from areas with higher pressure. Inhomogeneous surface morphology of the sulfur electrode (larger agglomerated particles rising from flat surface leaving behind marks on Li negative electrode) and SEM sample preparation could have influenced the appearance.

All in all, the SEM investigation of lithium electrodes after use in Li-S test cells confirmed the deterioration of lithium electrode surface upon prolonged cycling. The covering of the surface with porous and loosely packed lithium may have caused higher electrical resistance due to poor mechanical/electrical connection of the dendrites to the bulk lithium electrode and therefore increase electrode polarization. The deterioration of Li metal due to the formation of Li_2S layer was not investigated.

4.3.2.2 Li metal electrode surface morphology during stripping/plating experiments in Li:Li test cells

A further examination of Li electrodes was conducted to gain information on the evolution of lithium surface structure during electrochemical plating and stripping experiments.

Li-Li symmetrical pouch cells were used as testing device. For characterization of lithium electrodes in Li-S batteries, an increased number of factors (homogeneity and quality of sulfur electrodes of high loadings) would have complicated the study. However, for comparability between the Li-Li test cells and Li-S system, PS species (0.15M Li_2S_6) were added to the standard electrolyte to simulate conditions present in Li-S cells. The choice of parameters for stripping and plating experiments (current density and capacity) was based on the following considerations: In a practical Li-S cell high sulfur loadings per square centimetre are necessary to obtain reasonable energy densities. Therefore a sulfur loading of 3 mg/cm^2 was anticipated for Li-Li electrochemical tests (cf. chapter 4.4, p.90). The resulting capacity of 5 mAh/cm^2 was set as 1 C current. The influence of the current density (0.1 C and 0.5 C corresponding to 0.5 mA/cm^2 and 2.5 mA/cm^2) on the lithium surface morphology after stripping and plating procedure was investigated by stopping the Li-Li cells at different states of discharge and states

of charge within the first cycle and subsequent investigation of the Li metal electrodes by means of SEM. A total amount of charge of 5 mAh/cm^2 for each half cycle was investigated. Further, the lithium surface obtained after 10 charge/discharge cycles at a current density of 0.5 mAh/cm^2 and the evolution of lithium surface morphology of PVD-Li coated copper electrodes after stripping the entire Li coating and subsequent plating was studied. In the following discussion "discharge" refers to the dissolution of Li, like in a Li-S cell and "100%" corresponds to lithium stripping or plating of 5 mAh/cm^2.

For all samples, macroscopically visible differences in electrode appearance within one sample were observed. Shiny lithium areas, where obviously less lithium was stripped and plated, alternated rough and tarnished areas. Insufficient or inhomogeneous contact between the electrodes or a slightly curled separator may have caused the observed differences. SEM samples were taken from these regions which had obviously taken part in the electrochemical processes.

4.3.2.2.1 The influence of current density on the Li metal electrode surface morphology during one cycle of stripping/plating

Lithium metal electrodes with a thickness of 100 µm were used for the preparation of Li:Li cells. Figure 37 displays the surface of 100 µm Li before electrochemical modification. The investigation of the pristine lithium metal revealed a surface pattern along the direction of rolling during foil preparation process. A rough, rather than a perfectly smooth surface was observed.

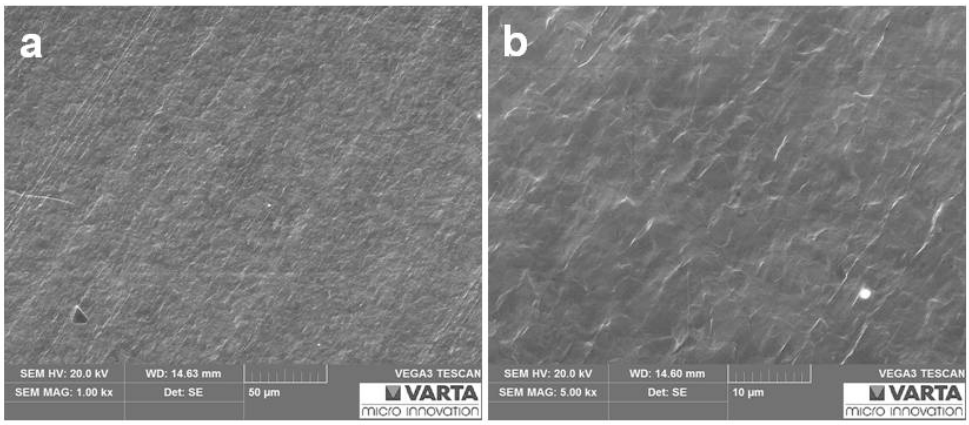

Figure 37: Surface of fresh 100 µm lithium metal foil at (a) 1kx and (b) 5kx magnification

From crystallographic point of view, the deformation of the ductile metal introduces irreversible displacements in the atomic structure. The presence of different types of defects on the lithium surface (pits, cracks, crystalline defects or grain boundaries) causes non-uniform lithium deposition. [79] [141]

The following figures show the surface of lithium after stripping experiment (100% discharged) at a current load of 0.5 mAh/cm^2 (cf. Figure 38) and 2.5 mAh/cm^2 (cf. Figure 40) respectively.

The dissolution of Li did not occur homogeneously distributed over the surface. Randomly distributed pits of various sizes (starting from approximately 50 µm) were generated at the surface of the lithium metal electrode. Areas where the initial morphology of the pristine lithium were preserved (cf. Figure 38 yellow circle 1) alternated with pit-like holes. The generation of randomly distributed pit holes was described in literature for low current densities (1 mA/cm^2) and was ascribed to metal passive layer breakdown and the subsequent further increased dissolution at these sites.[141] In some areas (cf. Figure 38 yellow circle 2) the whole initial surface was degraded and uncovered inner structure of lithium beneath the surface.

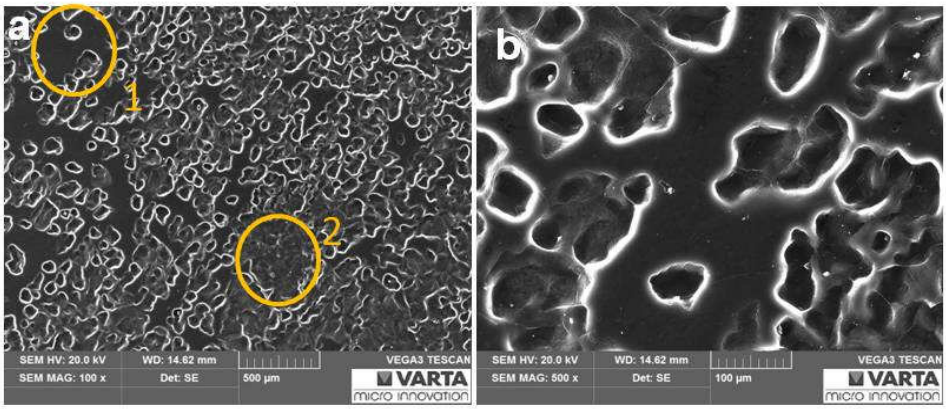

Figure 38: Lithium metal electrode surface after stripping at 0.5 mA/cm^2, 100% discharged, at (a) 100x and (b) 500x magnification

In the three dimensional image shown in Figure 39, the inhomogeneous lithium dissolution and the resulting height profile became obvious. The 3D image revealed the extent of holes in z direction with pits of approximately 50 µm in depth.

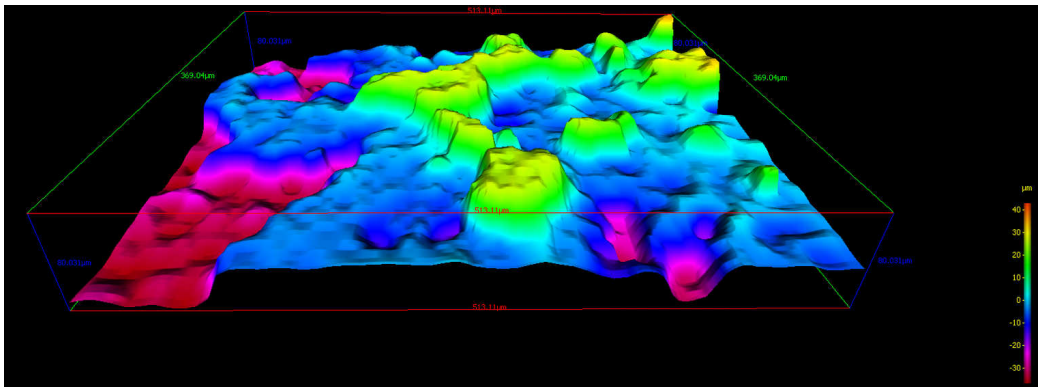

Figure 39: 3D image of lithium metal electrode surface after stripping 0.5 mA/cm^2, 100%discharged, recorded at 1kx magnification

The surface morphology of lithium electrode obtained from stripping experiment at the five-fold current load of 2.5 mA/cm^2, revealed a different structure compared to the morphology obtained at 0.5 mA/cm^2. Although some random pits are observed, these appear to be smaller in diameter (approximately 10µm) and the surface is dominated by irregularly shaped structure.

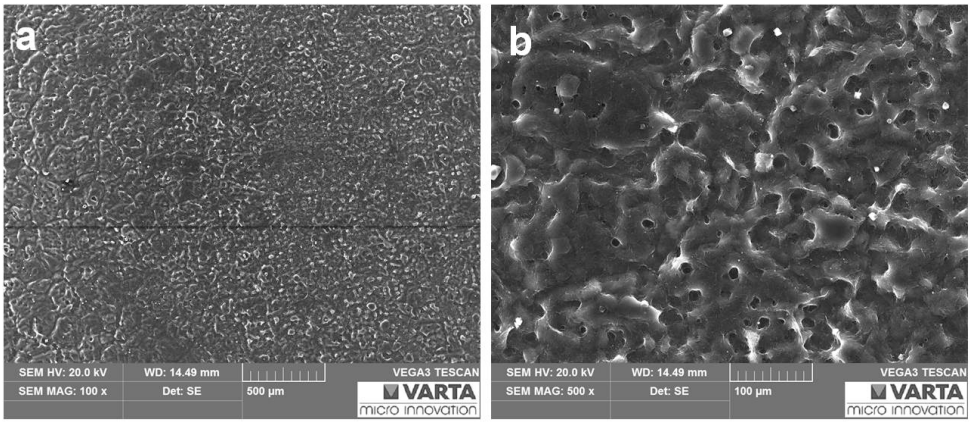

Figure 40: Lithium metal electrode surface after stripping at 2.5 mA/cm^2 (100% discharge) at (a) 100x and (b) 500x magnification

In subsequent plating process at 0.5 mAh/cm^2 (Figure 41) and 2.5 mAh/cm^2 (Figure 42) respectively, dendritic deposits were formed at the lithium surfaces. The images show the lithium surface obtained at 25% SOC (stripping 5 mAh/cm^2 and subsequent deposition of 1.25 mAh/cm^2).

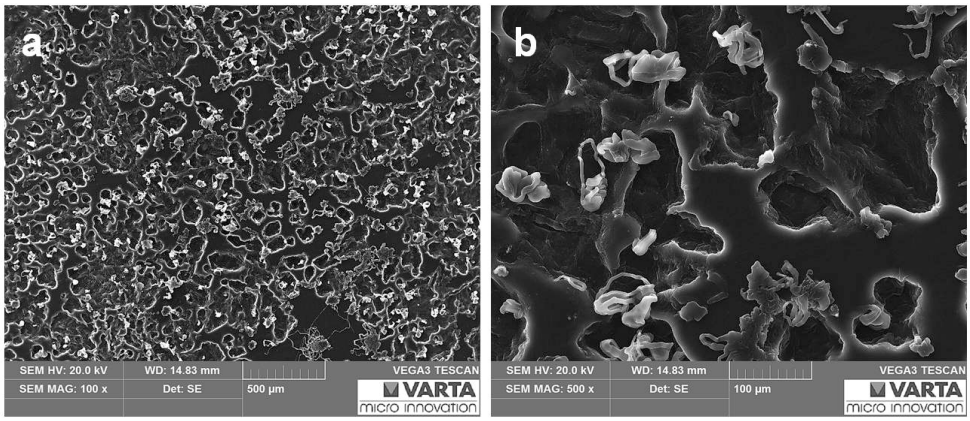

Figure 41: Lithium metal electrode surface after stripping (100%) and subsequent plating (25%SOC) at 0.5 mA/cm^2 at (a) 100x and (b) 500x magnification

At the pitted lithium surface, dendrites started to grow preferentially inside the pits and at the edges of the pits and therefore at sites with increased local current density.

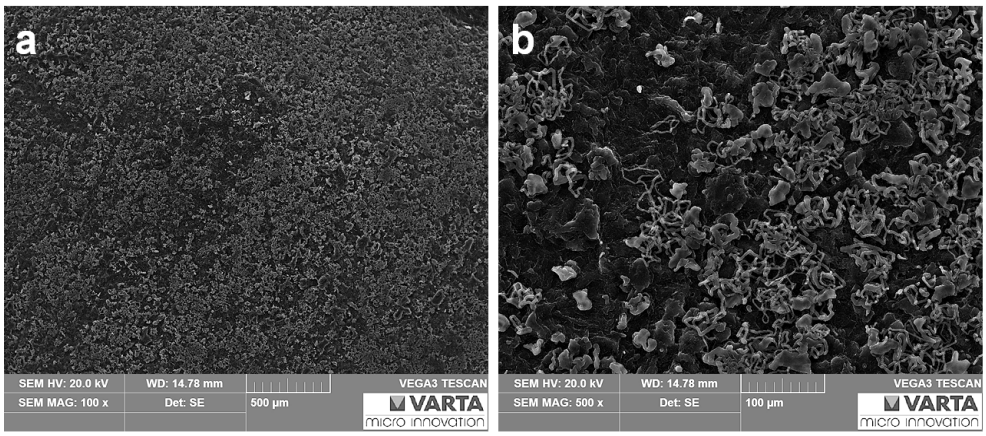

Figure 42: Lithium metal electrode surface after stripping (100%) and subsequent plating (25%SOC) at 2.5 mA/cm^2 at (a) 100x and (b) 500x magnification

In case of the irregularly structured surface obtained from stripping experiment with 2.5 mAh/cm^2 current density, dendritic deposits were irregularly distributed over the surface without obvious preferential spots. The separator hindered the dendrites from growing in direction of the counter electrode, instead dendrites started to bend backwards and form clew like structures which protruded from the lithium metal surface.

After one full cycle of stripping and subsequent plating (total amount of charge of 5 mAh/cm^2 for each step) the observed surface morphologies had nothing in common with the initial lithium metal surface morphology. Instead heavily structured surfaces were generated (Figure 43).

In case of lower current density (Figure 43 a and b), lithium deposits appear to form bended dendrites of larger diameter (approximately 10-20 µm and above) and some clew like formations protruding from the structured surface. In samples which were prepared at higher current density (Figure 43 c and d) the surface of lithium was covered by dendrites of smaller diameters (higher share of thread shaped deposits of 10 µm). In both cases the dendrite sizes are inhomogeneous, however the dimension of the dendrites obviously decreased with current density.

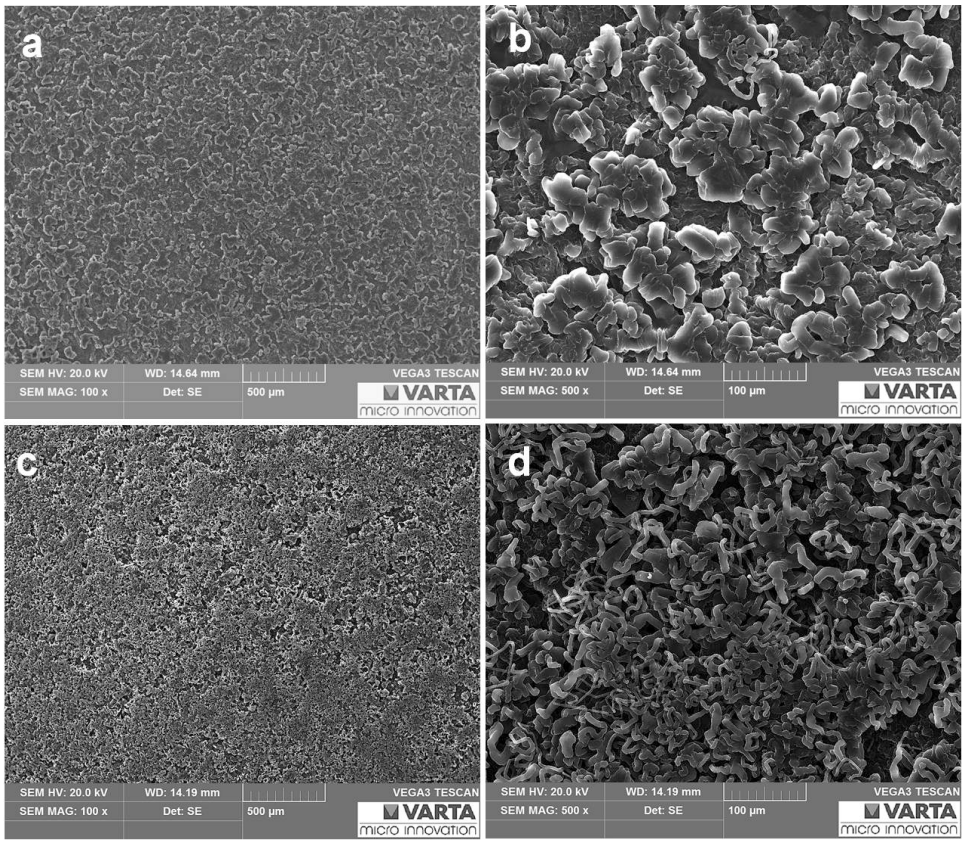

Figure 43: Lithium metal electrode surface after stripping (100%) and subsequent plating (100%SOC) at 0.5 mA/cm^2 (a,b) and 2.5 mA/cm^2 (c,d) at 100x and 500x magnification

Additionally lithium was stored in Li_2S_6 containing electrolyte for 20 hours corresponding to the duration of a full cycle of stripping and plating experiment at 0.1 C. No major morphological changes were observed within this time.

4.3.2.2.2 Influence of repeated stripping/ plating (10 cycles) on Li metal electrode surface morphology

Repeated stripping and plating for 10 cycles (ending with stripping process Figure 44 and ending with plating process Figure 45) at 0.5 mA/cm^2 revealed heavily structured surfaces. After stripping process a pitted surface was formed. At higher magnification (500x and 2kx) a loosely packed and highly structured layer of lithium deposits got visible. Inside the pits more pristine like lithium areas were observed. The lithium underneath did not show a continuous surface but was pitted itself. The adhesion of the porous layer to the bulk lithium seemed rather loose.

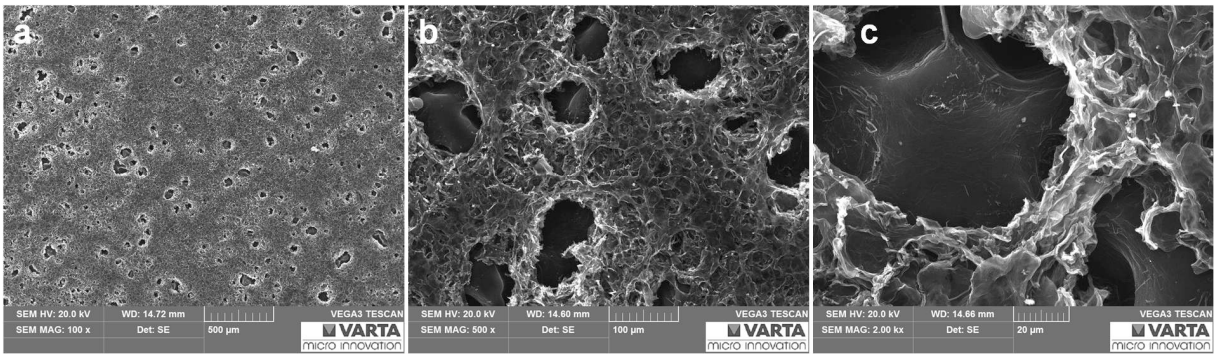

Figure 44: Lithium metal electrode surface after 10 cycles ending with stripping process at 0.5 mA/cm^2 at (a) 100x, (b) 500x and (c) 2kx magnification

During subsequent plating the surface was covered with lithium deposits which could be interpreted as bended needle like depositions of irregular shape and size of 10-20 µm in diameter. Cracks provided insight into regions beneath this layer and revealed the structured surface discussed in Figure 44.

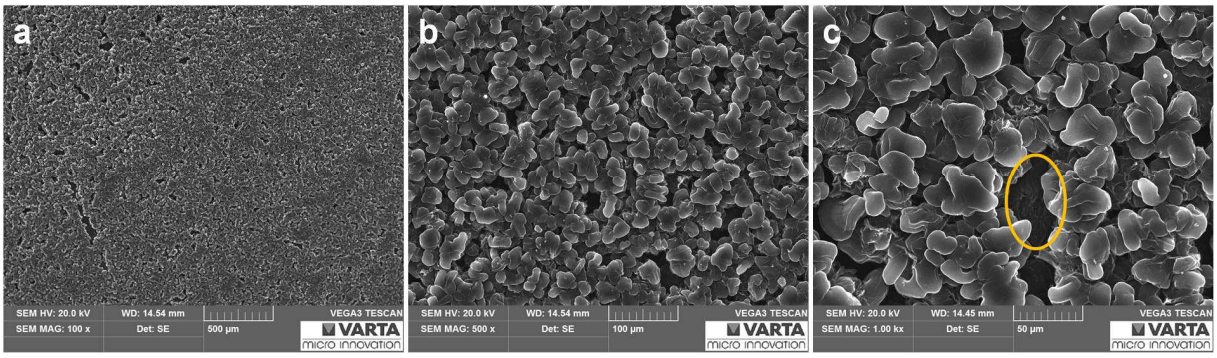

Figure 45: Lithium metal electrode surface after 10 cycles ending with plating process at 0.5 mA/cm^2 at (a) 100x, (b) 500x and (c) 1kx magnification

4.3.2.2.3 PVD-Li metal (on Cu current collector) electrode surface morphology during one cycle of stripping/plating

Further stripping/plating experiments with PVD-Li coated copper foil were performed. 20 µm PVD-Li coated Cu-foils were cycled under comparable conditions like in Li-Li cells with 100 µm thick bulk lithium.

The initial surface of PVD-Li (Figure 46) showed a clear difference in the surface texture in comparison to previously discussed 100 µm lithium metal foil. A difference was expected, due to the differences in the manufacturing processes of the two samples. Physical vapour deposition of lithium on copper foil substrate revealed a surface with domains of differently oriented stripe like structures in comparison to the stripes with preferential orientation in bulk lithium foils. Figure 46 a shows the obtained SEM image at 1kx magnification, while for Figure 46 b (1 kx) and c (5 kx) the SEM images are depicted as negative images in order to make the surface structure (differently oriented domains) better visible.

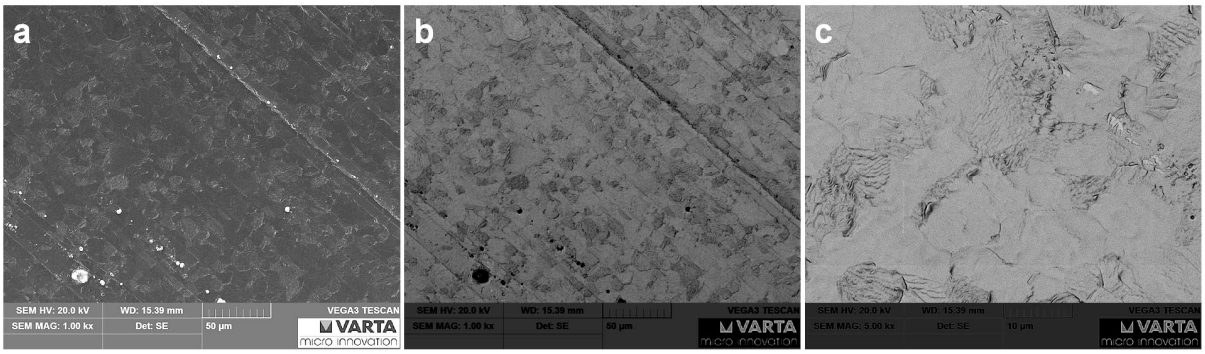

Figure 46: PVD-Li of 20 µm thickness on Cu foil at (a) 1kx and (b) 5kx

Inhomogeneous Li dissolution at a current density of 0.5 mA/cm^2 became visible in the SEM image when investigating the lithium/copper sample surface after 50% discharge (Figure 47 a and b). Randomly distributed isles of different size of lithium were observed next to areas where lithium was completely stripped and uncovered Cu surface appeared. The shape of the lithium isles reflected the surface structuring of the initial fresh sample and proved the strong influence of the initial micro texture on the stripping process. Lithium stripping of PVD-Li coated Cu occurred in angular formations. Within one cycle the complete lithium coating was stripped and therefore revealed the bare copper surface (Figure 47 c and d).

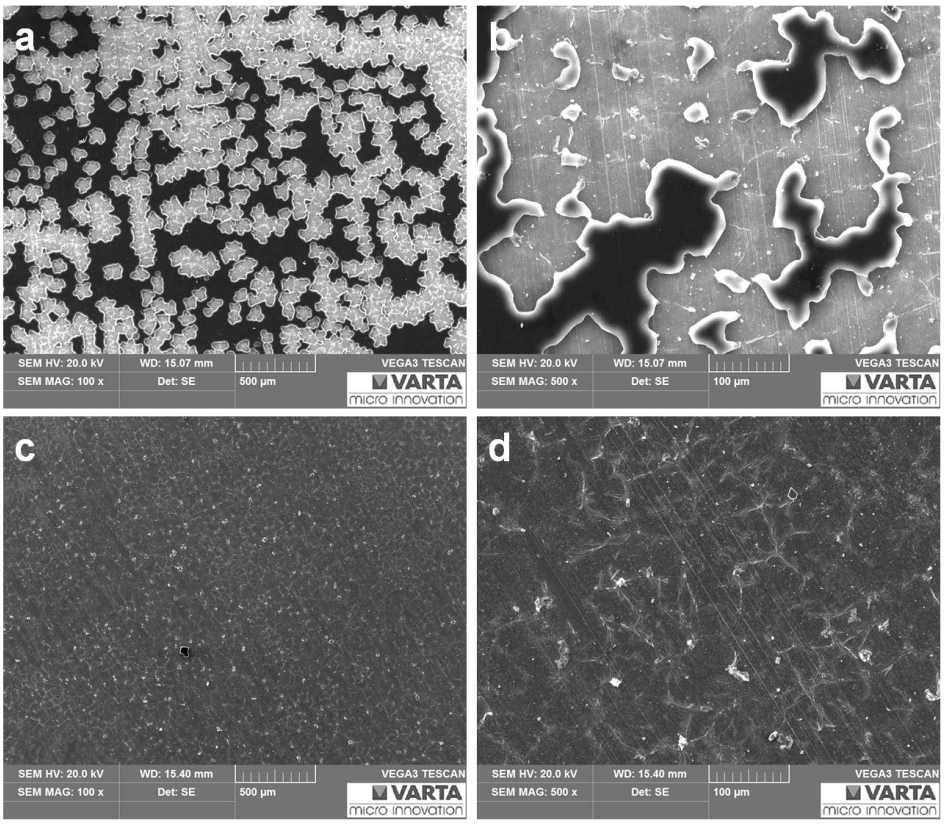

Figure 47: PVD-Li electrode surface after stripping 50% of the Li coating at 0.5 mA/cm^2 at 100x and 500x (a and b) and after stripping 100% of the Li coating at 100x and 500x (c and d)

In the subsequent plating process dendritic lithium deposits were observed covering up the copper surface (Figure 48). It has to be noted that in case of the 20 µm thick coating a total amount of charge of 4.2 mAh/cm^2 was plated/stripped during the experiments. This slightly deviated from the total amount of charge of 5 mAh/cm^2 applied in the experiments with 100µm bulk lithium.

PVD-Lithium coated on a copper foil current collector introduces the advantage of higher mechanical strength of the negative electrode during cell assembly and during operation of the cell. In [16] it was claimed that the application of lithium electrode with copper current collector and a rather complete utilization of lithium per cycle results in the creation of denser lithium electrode structure without the generation of dendritic surface upon cycling. This behaviour was not observed in the experiments applying PVD-Li coated copper samples as shown in Figure 48. This fact might be caused by the missing pressure during the electrochemical plating/stripping experiments.

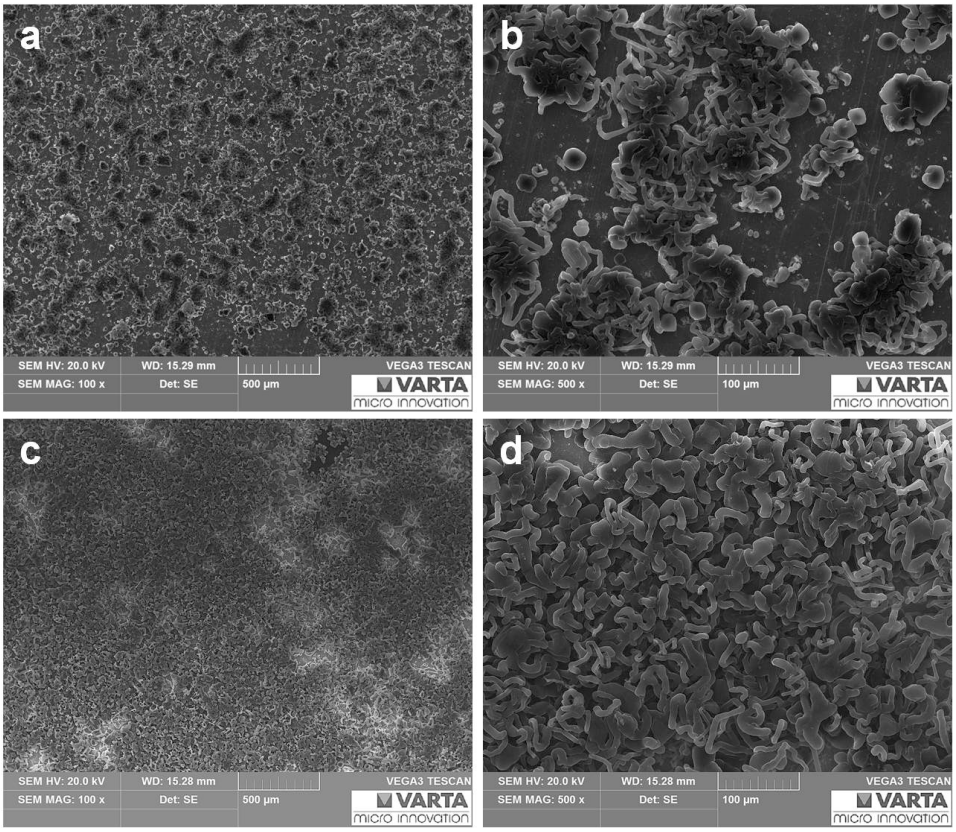

Figure 48: PVD-Li electrode surface after stripping at 0.5 mA/cm^2 (100%) and subsequent plating 25%SOC at 100x and 500x (a and b) and after plating 100%SOC at 100x and 500x (c and d)

4.3.3 Conclusion and outlook

The surface evolution of lithium electrodes during electrochemical lithium dissolution and subsequent plating was investigated in symmetrical Li:Li test cells. The cell and measurement set up was chosen correspondingly to practical Li-S cells with PS containing electrolyte, realistic current load and total amount of charge which was plated and stripped within one cycle. The surface of the electrode was completely changed within one cycle of stripping and subsequent plating as it was covered by dendritic deposits. Higher current densities resulted in higher surfaces areas, as finer dendritic structures were created. Repeated charge/discharge processes revealed a pitted porous lithium top layer on a more pristine lithium bulk beneath the surface after stripping process. This surface was again covered by dendritic shaped deposits in the following deposition procedure. The generation of the porous layer between bulk lithium and dendritic lithium deposits may have caused the increased lithium overpotential upon prolonged cycling in Li-S cell, as observed in three electrode galvanostatic cycling measurements and

simultaneous monitoring of electrode potentials. The implementation of the reference electrode (RE_{Li}) allowed ascribing the individual contributions of positive and negative electrode on cell performance. It revealed the high impact of the lithium metal electrode on cell performance over 200 cycles in dependence of capacity balance. The variation of electrode potentials in otherwise comparable measurements stated a challenge in these experiments. Assembling of the cells clearly had an impact on the quality and reproducibility of the results. Lithium electrode potential fluctuations from the very beginning clearly indicated the influence of cell manufacturing. Tests in which two Li reference electrodes (RE_{Li}) were applied within one Li-S pouch cell for monitoring the lithium potential (CE) twice (RE_{Li1} – CE and RE_{Li2} – CE) reflected the influence as two different potential curves were observed. Hence, only measurements with low initial overpotential (<±50 mV) for stripping and plating process were used for drawing further conclusions. Moreover an ideal reference electrode was assumed [142], which included the assumption that the RE_{Li} was non-polarisable and that its potential remained constant during the measurement, although no real reference electrode may completely fulfil these criteria.

A lithium buffer needs to be applied to compensate the poor cycling efficiency of lithium. However, as shown in the above measurements, lithium excess alone will not necessarily result in satisfying cycling performance, as e.g. continuous $LiNO_3$ and electrolyte consumption at increased lithium surface area and deteriorating lithium surface (increased electrode polarization) will further restrict (long term) performance. Problems caused by the lithium negative electrode need to be addressed as it greatly limits cell performance and safety. In contrast, intensive research on tailored structures in sulfur electrodes was conducted in the recent years and led to great improvements in terms of cycling stability and specific capacity of sulfur cathodes such as. [143] About 70% of publications until 2013 dealt with cathodes. [102]

With metallic lithium as negative electrode it remains questionable if safe cells with long cycle life can be realized. Solid electrolytes may be one of the possible solutions towards realizable Li-S batteries. Although plagued by several drawbacks such as low room temperature ionic conductivity and high inter-facial resistance between electrode materials and electrolyte, a solid electrolyte may restrict dendritic lithium deposition morphology and the continuous reaction of electrolyte with freshly generated lithium surface. Further the safety is enhanced due to exclusion of volatile and flammable electrolyte solvents. On the other hand, substitution of the Li electrode or the application of protected lithium electrodes (protecting layers) may allow the realization of safe Li-S cells (cf. chapter 2.4.4 and 2.4.5, p.30 and p.31).

4.4 Energy densities of Li-S demonstrator cells

The main motivation for the intensive research on Li-S cells is their high theoretical specific energy density of ~2500 Wh/kg (based on mass of active materials exclusively) resulting from high specific capacity of sulfur (1672 mAh/g) and lithium (3862 mAh/g) in combination with a moderate mean discharge voltage of 2.15 V (cf. page 11). This would correspond to a six-fold increase when compared to commercialised LIBs like $LiCoO_2$/graphite with a theoretical value of 387 Wh/kg.

Considering the volumetric energy density, theoretical values of ~2800 Wh/L considering Li and S and ~2200 Wh/L when including the volume of Li_2S at the end of discharge are obtained. Volumetric energy density of Li-S therefore still lies above theoretical values obtained in LIBs of e.g. ~1000 Wh/L for $LiCoO_2$/C, but the theoretical difference is not as high as in case of gravimetric energy densities. [14]

However, speaking in practical terms, the specific energy density of Li-S system is lowered significantly. The insulating nature of sulfur causes incomplete utilization of sulfur as active material and the necessity of high ratios of conducting agents in the electrodes. On the other hand low cycling efficiency of lithium and the continuous electrolyte consumption of ether based electrolytes at the lithium electrode raise the need of electrolyte excess in case of unprotected lithium electrodes (cf. chapter 2.5.1.3, page 37) and decrease the advantage in comparison to current state of the art LIBs.

4.4.1 Practically obtained energy densities in lab-scale Li-S cells

In comparison to test cells in single layer configuration (one single side coated cathode and anode), which were prepared for the investigation of electrochemical performance of electrode materials, lab-scale pouch demonstrator cells of higher capacity (~135 mAh theoretical capacity), applying prismatically wound electrodes, were assembled. Tests were conducted in order to gain information on the actually obtainable energy densities of the Li-S system on cell level. In context with Li-S cells, many publications aim at the presentation of sulfur electrodes of superior performance, but do not evaluate the compatibility of newly invented materials towards their use in practical cells and obtainable energy densities. The electrolyte amount and lithium balancing are rarely mentioned. The advantage of high capacity sulfur electrodes with high cycle lives may not be transferred directly to increased cell energy densities in *practical* Li-S cells because their performance pretty much depends on applied electrolyte ratio. One exception in

recent publications is Hagen et al. [144], who considered electrode composition and applied electrolyte amount in context with energy density of resulting Li-S cells.

Double sided sulfur electrodes with a sulfur ratio of 42 w% and a sulfur load on one single side of 1.8 mg/cm^2, corresponding to 3 mAh/cm^2, were used for preparation of demonstrator cells with ~135 mAh theoretical capacity. Lithium was used in excess (100 µm lithium corresponding to a theoretical and practical Li:S ratio of 3.5:1 and 7:1 respectively). The applied electrolyte amount was 5 µl/mgS and was calculated based on the theoretical sulfur loading irrespective of sulfur utilization. Prismatically wound cells were realized applying lithium electrodes without current collector foil for obtaining decreased cell weight despite the fact that this approach might not be cost effective. A higher lithium excess was necessary to maintain (mechanical) integrity especially during lithium dissolution upon discharge, keeping in mind the irregular dissolution of lithium observed in the SEM study (cf. chapter 4.3.2, p.78). Based on these experiments, theoretical calculations on obtainable energy densities of Li-S cells in dependence of sulfur electrode specifications (sulfur ratio, sulfur utilization) and various electrolyte ratios were made.

Figure 49 shows the cycling performance of the corresponding Li-S pouch cell with prismatically wound electrodes and a theoretical capacity of 135 mAh as well as the cycling performance of a single layer cell applying the same materials. The cycling performances of the single layer and of the prismatically wound Li-S cells were comparable and confirmed the feasibility of up scaling single layer to lab-scale demonstrator cells. In the initial cycle, specific discharge capacities based on mass of sulfur of 1000 mAh/g and 920 mAh/g and after 10 cycles of 830 mAh/g and 790 mAh/g were obtained for the single layer and the prismatically wound cells respectively.

Considering the prismatically wound cell, due to the rather low sulfur ratio of 42 w% in the electrode, the specific discharge capacity based on the mass of electrode loading was ~390 mAh/g. The theoretical cell capacity of 135 mAh was reduced to a practical value of ~75 mAh in the initial cycle. The average discharge voltage was ~2.1 V and the average charge voltage was ~2.3 V. The resulting energy density based on cell weight was 80 mWh/g.

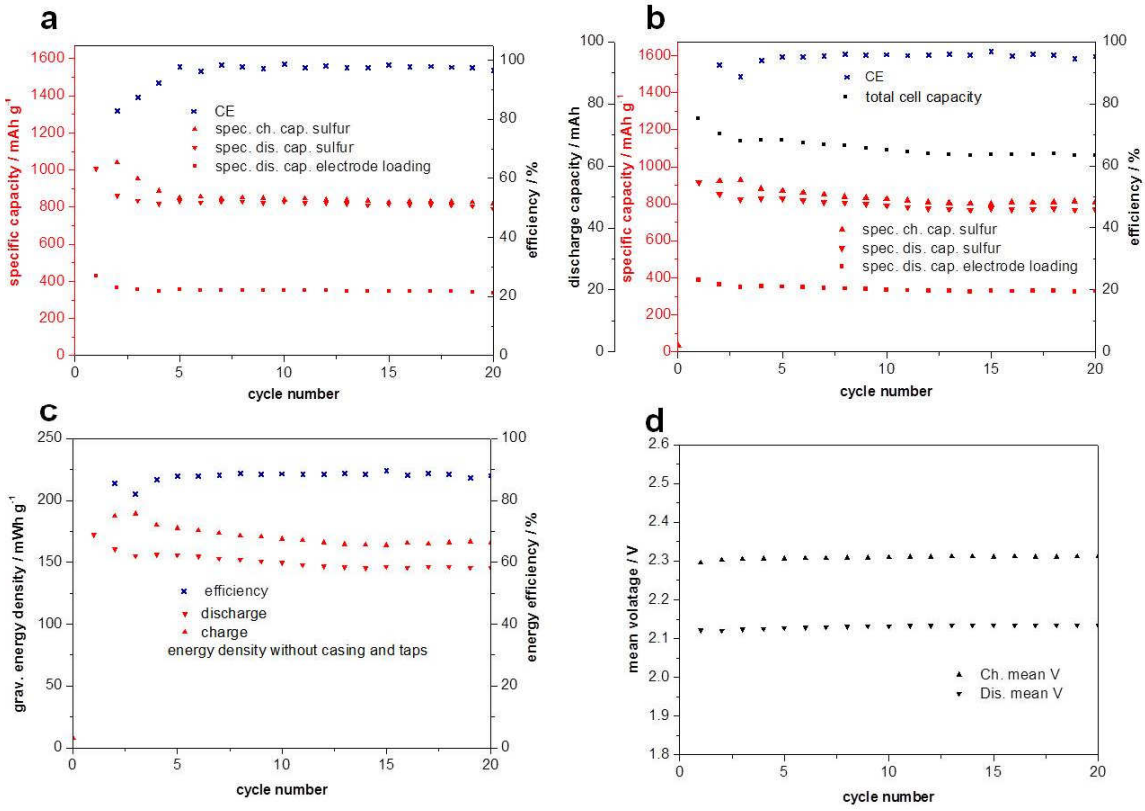

Figure 49: Cycle performances of a single layer Li-S cell of theor. 20 mAh (a) and a prismatically wound Li-S cell of theor. 135 mAh with prismatically wound cell (b); energy density without casing and taps of prismatically wound cell (c) and corresponding mean average voltages (d) for the first 20 cycles

However, size and weight of the casing vary with different cell designs. Including the cell casing in energy density calculations would have falsified the energy density calculations and therefore the cell casing and also the current collector taps were not considered in the cell weight in the following discussion. The resulting energy density for the here discussed cell, excluding casing and taps was 170 mWh/g in the first and 150 mWh/g in the 10th cycle. The energy efficiency was about 89-90% and was determined by CE and the difference between charge and discharge mean voltages. Energy efficiency is especially important for practical Li-S cells as it directly influences cost during battery usage.

The mass break down, which is shown in Figure 50, shows the share of different cell components on the total weight of the cell.

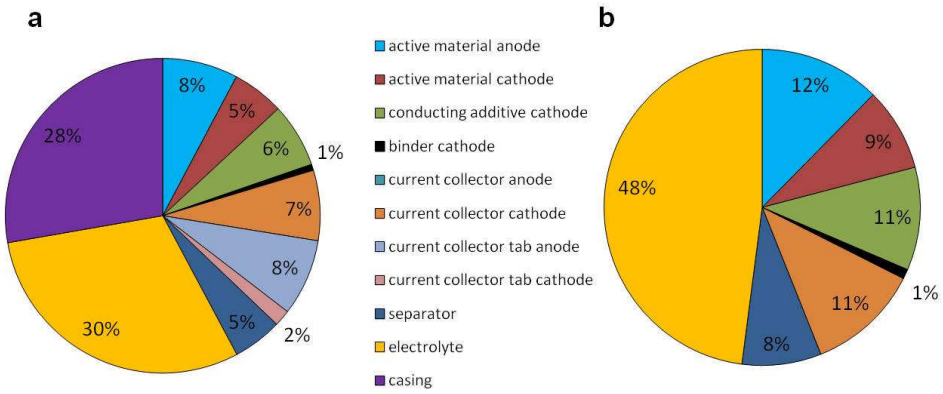

Figure 50: Mass break down (w%) of lab-scale demonstrator cell including (a) and not including (b) casing and current collector taps

From the mass break down the high share of electrolyte on the total cell weight got obvious. If the casing was not included in the mass break down, the electrolyte counted for nearly half of the weight of the components of the cell. In this scenario the electrolyte amount was already chosen rather low but practically realizable (5 µl/mgS) as shown in Figure 49 b.

In comparison to publications on optimized electrolyte ratio (for various electrode compositions) best cell performances were obtained with higher electrolyte amounts. Zheng et al. [43] screened electrolyte/sulfur ratios of 50-10 µl/mgS and determined a ratio of ~20 µl/mgS as optimum ratio for an electrode with ~0.4 mg/cm^2 sulfur loading (sulfur ratio in the range of 25 w%) to obtain a specific sulfur capacity of 800 mAh/g after 100 cycles at ~0.13 mA/cm^2. Zhang [34] obtained an optimized performance when applying an electrolyte ratio of 10 µl/mgS at a sulfur loading of 2.0 mg/cm^{2}with a specific sulfur capacity of 780 mAh/g after 100 cycles at 0.5 mA/cm^2 (sulfur ratio of 72 w%) (in comparison to 6.5 µl/mg and 13.3 µl/mg). In both cases electrolyte amount was optimized for cycling performance.

For the here discussed type of Li-S cell, pre-tests with higher electrolyte ratio of 8 µl/mgS and higher negative electrode capacity excess of 8:1 (theoretical) revealed specific sulfur capacities of 970 mAh/g and 870 mAh/g at the initial and the 10th cycle respectively. Therefore the lower electrolyte amount and also limited lithium capacity did not affect the cell performance in the initial 20 cycles negatively (cf. appendix Figure 52). However, in terms of energy density, the electrolyte amount (inactive weight of the cell) has to be further reduced.

The minimum amount of electrolyte which is necessary to obtain satisfying electrochemical performance depends on the sulfur electrode (density, thickness, sulfur loading, carbon type and loading) and lithium surface evolution and has to be determined separately for each type of sulfur electrode [34]. Continuous consumption, increased at higher current loads will determine the cycle life of cells with restricted electrolyte amounts. A common statement on preferential electrolyte ratio in the cell cannot be given and has to be determined experimentally, with regard to either maximized energy density or cycle life.

4.4.2 Theoretical calculations of energy densities of Li-S cells

For the theoretical design of cells with high energy densities various parameters had to be considered. Starting from the above discussed cell, several cell scenarios were simulated by simply varying single or multiple parameters with major influence on energy density. In practical cells, modifying one parameter would in turn influence other performance determining parameters (e.g. increasing the weight ratio of sulfur in an electrode or decreasing the electrolyte amount could result in decreased sulfur utilization and hence specific sulfur capacity). The advantage of theoretical calculations therefore was that conclusions on the influence of single parameters on energy density could be drawn, while all the others were kept at a constant value. This opened the possibility to test or even exceed the limits of practically feasible electrode or cell specifications.

In the following Figure 51 calculated gravimetric energy densities (without casing and current collector taps) are depicted. Starting from the above discussed practically realized cell (sulfur electrode with 42.5 w%S and a spec. discharge capacity of sulfur of 800 mAh/g), further calculations based on increased sulfur ratios in the electrode of 60 w% and 80 w% (anticipating constant thickness of 80 µm at each side, therefore absolute sulfur load was increased corresponding to relative ratio) and increased sulfur utilization of 1200 mAh/g and 1600 mAh/g were made. In this context, the influence of the electrolyte amount per mg of sulfur, which was identified as a major parameter increasing the cell weight, was investigated through step wise reduction to finally 1 µl/mgS. Some assumptions may not be realizable but demonstrated the limits of the considered system. All scenarios were calculated for a 5-fold and 3-fold lithium to sulfur capacity ratio (based on the 800, 1200 and 1600 mAh/g specific capacities of sulfur anticipated for the different scenarios). The electrolyte weight was calculated based on the determined standard electrolyte density at 20°C of 1.124 g/cm^3 and the average discharge voltage was set to 2.15 V vs. Li/Li$^+$. The separator had a weight of 0.0016 g/cm^2.

The calculation showed that even under unrealistic low electrolyte ratios of 1 µl/mgS a rather low gravimetric energy density of 250 mWh/g would be obtained when preparing cells from the above discussed electrodes with rather low sulfur ratio and utilization (cf. Figure 51 a and d, black rectangle symbol). The reduction of electrolyte ratio (based on sulfur loading, but not on sulfur utilization) from e.g. 3 µl/mgS to hypothetical 1 µm/mgS resulted in a gain in energy density of 150 mAh/g for the discussed Li-S cell (anticipating constant sulfur utilization despite reduced electrolyte amount).

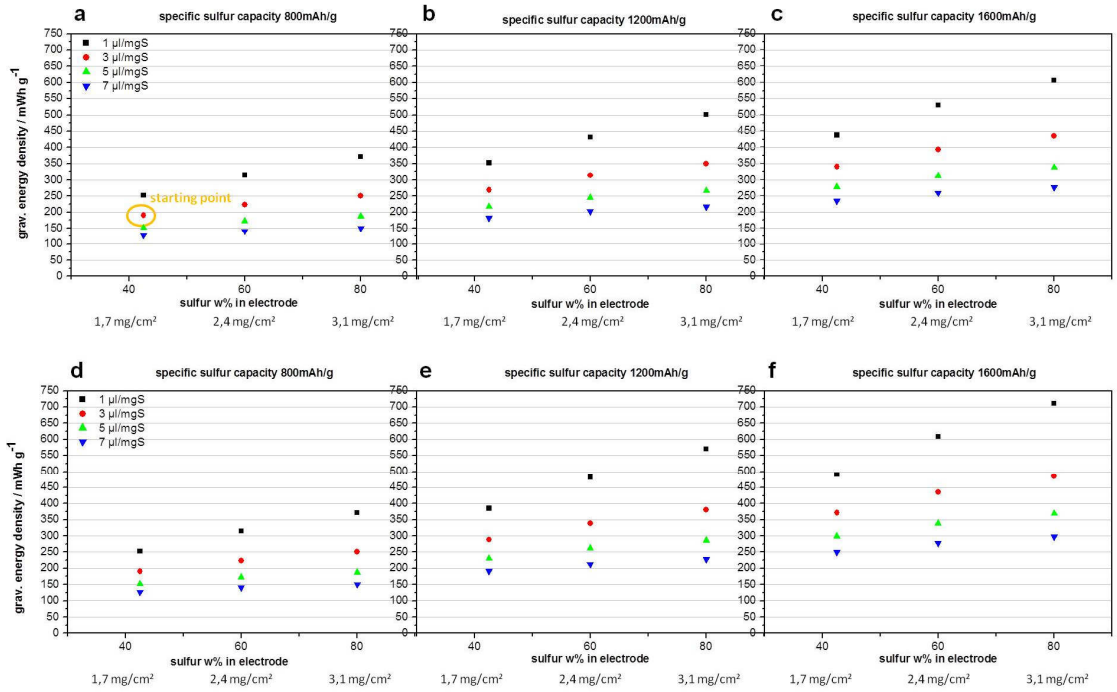

Figure 51: Calculated gravimetric energy densities of Li-S cells with 5-fold (a, b, c) and 3-fold (d, e, f) lithium capacity excess in dependence of sulfur weight ratio in the positive electrode, electrolyte amount and specific sulfur discharge capacity of (a, d) 800 mAh/g, (b, e) 1200 mAh/g and (c, f) 1600 mAh/g; the yellow circle marks the practically realized lab-scale demonstrator cell

With a sulfur load of 80 w% and a specific sulfur capacity of 1600 mAh/g (which may be hard to achieve when considering high sulfur ratios and low electrolyte amounts) and setting the electrolyte amount to a low value of 1 µl/mg resulted in maximum achievable energy densities of 600 mWh/g and 710 mAh/g at 5-fold and 3-fold lithium capacity excess respectively for the considered electrodes/electrolyte system (based on cell weight without casing and taps) (cf. Figure 51 c, f). Comparison of Fig a with d and c with f clearly showed that the impact of the overbalanced lithium electrode on specific energy density gets higher in case of high areal sulfur

capacities and utilization. While at low sulfur capacities, a 5-fold or 3-fold lithium capacity excess hardly showed an influence on specific energy density, in case of 1600 mAh/g However, according to literature, working Li-S cells that show good performance though applying such low electrolyte amounts have not been realized yet. Nevertheless, the simulations showed that there is a great potential of Li-S cells to outperform state of the art LIBs in terms of energy density.

4.4.3 Conclusion and outlook

The calculations illustrate the difficulty to transfer the theoretical advantages of high specific capacity and energy density from material to cell level. Calculations on theoretically obtainable gravimetric energy densities in dependence of electrode characteristics and electrolyte amount were shown.

Since Li-S is not yet commercialized, energy densities achieved with practical Li-S cells are not available. OXIS Energy LDT however promotes Li-S cells of 165 Wh/kg and high cycle life 1500 cycles as well as cells of 300 Wh/kg with restricted cycle life of 100 cycles (cf. chapter 2). The different specifications of the promoted cells, aiming either at high cycle life or high gravimetric energy density, reflect the conflict of goals caused by the necessity of an electrolyte buffer. With the ether based electrolyte LiTFSI-$LiNO_3$-DME-DOL and unprotected lithium, high energy densities outperforming the current LIBs will only be feasible at an expense of cycle life.

Sion Power Corp. is using a protecting layer on the lithium electrode to reduce negative influence of lithium on cycling performance of rechargeable lithium cells and claims to achieve energy densities in Li-S cells of ~400 Wh/kg. This approach might state a possibility to increase energy density due to decreased electrolyte amount. However, protecting layers which are introduced at electrode surface prior to assembly might deteriorate (cf. chapter 2.4.4, p.30) during prolonged cycling, if self healing properties are not given.

Within this chapter emphasis was put on the gravimetric energy density. In terms of volumetric energy density the tap density of the electrode is crucial. High ratios of conductive carbons, that are necessary to obtain reasonable sulfur utilization, decrease volumetric energy density. Further, the fact that sulfur has a relatively low density of 2.07 g/cm^3 in comparison to metal oxides (4-5 g/cm^3) and phosphates (3.6 g/cm^3) may impose an additional challenge for Li-S to outperform state of the art LIBs in terms of volumetric energy density.[145] On the other hand, a high lithium excess has higher impact on volumetric than on gravimetric energy density, due to

the low density of Li metal of 0.534 g/cm^3. Also high electrolyte ratios again decrease volumetric energy density.

The substitution of the Li metal electrode by e.g. Si based negative electrode materials may enable the reduction of electrolyte amounts due to decreased electrolyte consumption. On the other hand, the search for different electrolytes should be intensified, that are thermodynamically more stable against the negative Li metal electrode than ether based electrolytes. New electrolytes may also be selected in terms of increased lithium cycling efficiency. Sulfur electrodes with tailored structures are needed that enable high sulfur utilization even at high areal loadings and that work with low electrolyte amounts. Increased sulfur utilization at low electrolyte amounts is the key to increase energy density. These measures may enable increased energy densities for Li-S in future.

5 Appendix

5.1 List of Abbreviations for experimental part

abbreviation	description
ATR-FTIR	attenuated total reflection-Fourier transform infrared spectroscopy
CC	galvanostatic cycling
CE	coulombic efficiency
CMC	carboxymethylcellulose
CV	cyclovoltammetry
DCPD	dicyclopentadiene
DME	1,2-dimethoxyethane
DOL	1,3-dioxolane
E_{CE}	counter electrode potential
EDX	Energy Dispersive X-Ray
E_{RE}	reference electrode potential
E_{WE}	working electrode potential
HIPE	high internal phase emulsion
Li	Li metal
Li^+	Li-ion
LIB	lithium ion battery
$LiNO_3$	lithium nitrate
Li-S	lithium-sulfur
LiTFSI	lithium bis(trifluoromethane)sulfonimide
OCV	open circuit voltage
pDCPD	poly dicyclopentadiene
Pluronic® L-121	Poly(ethylene glycol)-block-poly(propylene glycol)-block-poly(ethylene glycol) (PEG-PPG-PEG)
PP	polypropylene
PS	lithium polysulfides Li2Sx(x=2-8)
PVD-Li	physical vapour deposited Li
RE_{Li}	lithium reference electrode
ROMP	ring opening metathesis polymerization

RT	room temperature
SBR	styrene butadiene rubber
SEM	Scanning Electron Microscopy
SOC	state of charge
Super P^{TM}Li	carbon black
TGA/DSC	thermogravimetry-differential scanning calorimetry

5.2 List of Chemicals

chemical	**company**
Al	Carl Roth GmbH + CO. KG, 99,0%
Cu-foil	Carl Schlenk AG
DCPD	Sigma Aldrich
DME	Fluke, distilled
DOL	Sigma Aldrich, distilled
KOH	Carl Roth GmbH + CO. KG, ≥85%
Li metal	Kyokuto Metal Co. Ldt.
$LiNO_3$	Sigma Aldrich, 99.99%
LiTFSI	io-lit-tec, >99%
M2	Sigma Aldrich
Ni-foil	Carl Schlenk AG, 99.6%
Ni-mesh	Spörl oHG, 99.2%
Pluronic®L-121	Sigma Aldrich, Mn~4400
PVD-Li on 13µm Cu foil	Sidrabe Inc.
Sulfur	Sigma Aldrich, reagent grade
Toluol	Merck, 99.5%

5.3 List of figures

5.4 List of tables

5.5 Contributions for publications

Papers:

Müller M., Choudhury S., Gruber K., Cruz V.B., Fuchsbichler B., Jacob T., Koller S., Stamm M., Ionov L, Beckhoff B. Sulfur X-ray absorption fine structure in porous Li-S cathode films measured under argon atmospheric conditions, *Spectrochmica Acta Part B: Atomic Spectroscopy* ,2014, 94-95, 22-26

Agrawal M., Choudhury S., Gruber K., Simon F., Fischer D., Albrecht V., Göbel M., Koller S., Stamm M., Ionov L. Porous carbon materials for Li–S batteries based on resorcinol–formaldehyde resin with inverse opal structure, *J. Power Sources*, 2014, 261, 363-370

Thieme S., Brückner J., Meier A., Bauer I., Gruber K. Kaspar J., Helmer A., Althues H., Schmuck M., Kaskel S. A lithium–sulfur full cell with ultralong cycle life: influence of cathode structure and polysulfide additive, *J.Mater.Chem.A*, 2015, 3, 3808-3820

Poster:

Gruber K., Fuchsbichler B., Koller S., Investigation of performance parameters of Lithium Sulfur Batteries, *The 16th International Meeting on Lithium Batteries*, June 17 -22, 2012, ICC Jeju, Korea

6 Bibliography

[1]. **IEA.** [Online] [Cited: 20 03 2015.] http://www.worldenergyoutlook.org/.

[2]. **Larcher D., Tarascon J-M.** Towards greener and more sustainable batteries for electrical energy storage. *Nature Chem.* 7 (2015) 19.

[3]. *www.volkswagen.at.* [Online] [Cited: 01 06 2015.] https://www.volkswagen.at/modelle/e-golf/ausstattungsvarianten.

[4]. **Herbert D., Ulam J.** *Electric dry cells and storage batteries.* (1962). US Patent 3, 043, 896.

[5]. **Rao M.L.B.** *Organic electrolyte cells.* (1968). US Patent 3, 413, 154.

[6]. **Daniel C., Besenhard J.O.** *Handbook of Battery Materials, Second Edition.* Wiley-VCH Verlag GmbH & Co. KGaA. (2011) chapter 1,3,13,24.

[7]. **Brandt K.** Historical development of secondary lithium batteries. *Solid State Ionics.* 69 (1994) 173.

[8]. **Mohri M., Yanagisawa N., Tajima Y., Tanaka H., Mitate T., Nakajima S., Yoshida M., Yoshimoto Y., Suzuki T., Wada H.** Rechargeable Lithium Battery Based on Pyrolytic Carbon as a Negative Electrode. *J. Power Sources.* 26 (1989) 545.

[9]. **Mizushima K., Jones P.C., Wiseman P.J., Goodenough J.B.,.** LixCoO2 (0<x<=1): A New Cathode Material For Batteries Of High Energy Density. *Solid State Ionics .* 3/4 (1981) 171.

[10]. **Tarascon J.-M., Armand M.** Issues and challenges facing rechargeable lithium batteries. *Nature.* 414 (2001) 359.

[11]. **Van Noorden R.** A Better Battery - Chemists are reinventing rechargeable cells to drive down costs and boost capacity. *Nature (news feature).* 507 (2014) 26.

[12]. **Scrosati B., Garche J.** Lithium batteries: Status, prospects and future. *J. Power Sources.* 195 (2010) 2419.

[13]. **Hagen M.** Dissertation. *Untersuchung von binderfreien Schwefelkathoden als Hochenergiespeicher der nächsten Generation.* 2013.

[14]. **Bruce P.G., Freunberger S.A., Hardwick L.J., Tarascon J-M.** Li-O2 and Li-S batteries with high energy storage. *Nature Mater.* 11 (2012) 19.

[15]. **OXISenergy.** [Online] [Cited: 27 03 2015.] http://www.oxisenergy.com/.

[16]. **SionPower.** [Online] [Cited: 12 02 2015.] http://www.sionpower.com/technology.html.

[17]. **Broadhead J., Kuo H.C.** Electrochemical Principles and Reactions. Linden D., Reddy T.B. *Handbook of Batteries - third edition.* The McGraw-Hill Companies, Inc. (2002).

[18]. **Hamann C.H., Vielstich W.** *Elektrochemie 4.Auflage.* Wiley-VCH Verlag GmbH & Co. KGaA. (2005) chapter 3, 4.

[19]. **Winter M., Brodd R.J.** What Are Batteries, Fuel Cells, and Supercapacitors? *Chem. Rev.* 104 (2004) 4245.

[20]. **Brett C.M.A., Brett M.O.** *Electrochemistry - Principles, Methods, and Applications.* Oxford University Press (1994) p.13-20.

[21]. **Bagotsky B.S.** *Fundamentals of Electrochemistry Second Edition.* John Wiley & Sons, Inc (2006) p.22-31, 48-50,79-82.

[22]. **Stangl C.** Non-destructive electrochemical investigations of Lithium Ion Batteries. *Dissertation.* (2011).

[23]. **Holleman A.F., Wiberg E., Wiberg N.** *Lehrbuch der Anorganischen Chemie 102. Auflage.* Berlin : Walter de Gruyter & Co., (2007).

[24]. **Liang C., Dudney N.J., Howe J.Y.** Hierarchically Structured Sulfur/Carbon Nanocomposite Material for High-Energy Lithium Battery. *Chem. Mater.* 21 (2009) 4724.

[25]. **Ellis B. L., Lee K.T., Nazar L.F.** Positive Electrode Materials for Li-Ion and Li-Batteries. *Chem. Mater.* 22 (2010) 691.

[26]. **Kolosnitsyn V.S., Karaseva E.V.** Lithium-Sulfur Batteries: Problems and Solutions. *Russ. J. Elektrochem.* 44 (2008) 548.

[27]. **Ahn H-J., Kim K-W., Ahn J-H.** Lithium-Sulfur. Garche J. *Encyclopedia of Electrochemical Power Sources.* Elsevier B.V.. (2009) 155.

[28]. **Hagen M., Schiffels P., Hammer M., Dörfler S., Tübke J., Hoffmann M.J., Althues H., Kaskel S.** In-Situ Raman Investigation of Polysulfide Formation in Li-S Cells. *J. Electrochem. Soc.* 160 (2013) A1205.

[29]. **Schneider H., Gollub C., Weiß T., Kulisch J., Leitner K., Schmidt R., Safont-Sempere M.M., Mikhaylik Y., Kelley T., Scordilis-Kelley C., Laramie M., Du H.** On the Electrode Potentials in Lithium-Sulfur Batteries and Their Solvent-Dependence. *J. Electrochem. Soc.* 161 (2014) A1399.

[30]. **Leghié P., Lelieur J-P., Levillain E.** Comments on the mechanism of the elctrochemical reduction of sulphur in dimethylformamide. *Electrochemistry Communications.* 4 (2002) 406.

[31]. **Zhang S.S.** Liquid electrolyte lithium/sulfur battery: Fundamental chemistry, problems, and solutions. *J. Power Sources.* 231 (2013) 153.

[32]. **Marmorstein D., Yu T.H., Striebel K.A., McLarnon F.R., Hou J., Cairns E.J.** Electrochemical performance of lithium/sulfur cells with three different polymer electrolytes. *J. Power Sources.* 89 (2000) 219.

[33]. **Koh J.Y., Park M-S., Kim E.H., Jeong B.O., Kim S., Kim K.J., Kim J-G., Kim Y-J., Jung Y.** Understanding of Electrochemical Oxidation Route of Electrically Isolated Li2S Particles. *J. Electrochem. Soc.* 161 (2014) A2133.

[34]. **Zhang S.S.** Improved Cyclability of Liquid Electrolyte Lithium/Sulfur Batteries by Optimizing Electrolyte/Sulfur Ratio. *Energies.* 5 (2012) 5190.

[35]. **Cheon S-E., Ko K-S., Cho J-H., Kim S-W., Chin E-Y., Kim H-T.** Rechargeable Lithium Sulfur Battery 1.Structural Change of Sulfur Cathode During Discharge and Charge. *J. Electrochem. Soc.* 150 (2003) A796.

[36]. **Akridge J.R., Mikhaylik Y. V., White N.** Li/S fundamental chemistry and application to high-performance rechargeable batteries. *Solid State Ionics.* 175 (2004) 243.

[37]. **Mikhaylik Y. V., Akridge J.R.** Polysulfide Shuttle Study in the Li/S Battery System. *J. Electrochem. Soc.* 151 (2004)A1969.

[38]. **Rauh R.D., Abraham K.M., Pearson G.F., Surprenant J.K., Brummer S.B.** A Lithium/Dissolved Sulfur Battery with an Organic Electrolyte. *J. Electrochem. Soc.* 126 (1979)523.

[39]. **Peled E., Sternberg Y., Gorenshtein A., Lavi Y.** Lithium-Sulfur Battery: Evaluation of Dioxolane-Based Eelctrolytes. *J. Electrochem. Soc.* 136 (1989) 1621.

[40]. **Yamin H., Gorenshtein A., Penciner J. Sternberg Y., Peled E.** Lithium Sulfur Battery - Oxidation/Reduction Mechanism of Polysulfides in THF Solutions. *J. Electrochem. Soc. .* 135 (1988) 1045.

[41]. **Cheon S-E., Ko K-S., Cho J-H, Kim S-W., Chin E-Y., Kim H.T.** Rechargeable Lithium Sulfur Battery 2. Rate Capability and Cycle Characteristics. *J. Electrochem. Soc.* 150 (2003) A800.

[42]. **Lacey M.J., Jeschull F., Edström K., Brandell D.** Functional, water-soluble binders for improved capacity and stability of lithium-sulfur batteries. *J. Power Sources.* 264 (2014) 8.

[43]. **Zheng J., Lv D., Gu M., Wang C., Zhang J-G., Liu J., Xiao J.** How to Obtain Reproducible Results for Lithium Sulfur Batteries? *J.Electrochem.Soc.* 160 (2013) A2288.

[44]. **Ding N., Chien S.W., Hor T.S.A., Liu Z., Zong Y.** Key parameters in design of lithium sulfur batteries. *J. Power Sources.* 269 (2014) 111.

[45]. **Ji X., Lee K.T., Nazar L.F.** A highly ordered nanostructured carbon-sulphur cathode for lithium-sulphur batteries. *Nature Mater.* 8 (2009) 500.

[46]. **He G., Evers S., Liang X., Cuisinier M., Garsuch A., Nazar L.** Tailoring Porosity in Carbon Nanospheres for Lithium-Sulfur Battery Cathodes. *ACS nano.* 7 (2013) 10920.

[47]. **Jayaprakash N., Shen J., Moganty S.S., Corona A., Archer L.** Porous Hollow Carbon@Sulfur Composites for High-Power Lithium-Sulfur Batteries. *Angew. Chem. Int. Ed.* 50 (2011) 5904.

[48]. **Wang J-Z., Lu L., Choucair M., Stride J. A., Xu X., Liu H-K.,.** Sulfur-graphene composite for rechargeable lithium batteries. *J. Power Sources.* 196 (2011) 7030.

[49]. **Wang H., Yang Y., Liang Y., Robinson J.T., Li Y., Jackson A., Cui Y., Dai H.** Graphene-Wrapped Sulfur Particles as a Rechargeable Lithium-Sulfur Battery Cathode Material with High Capacity and Cycling Stability. *Nano Lett.* 11 (2011) 2644.

[50]. **Ji L., Rao M., Zheng H., Zhang L., Li Y., Duan W., Guo J., Cairns E.J., Zhang Y.** Graphene Oxide as a Sulfur Immobilizer in High Performance Lithium/Sulfur Cells. *J.Am.Chem.Soc.* 133 (2011) 18522.

[51]. **Qui Y., Li W., Zhao W., Li G., Hou Y., Liu M., Zhou L., Ye F., Li H., Wei Z., Yang S., Duan W., Ye Y., Guo J., Zhang Y.** High-Rate, Ultralong Cycle-Life Lithium/Sulfur Batteries Enabled by Nitrogen-Doped Graphene . *Nano Lett.* 14 (2014) 4821.

[52]. **Su Y-S., Fu Y., Manthiram A.** Self-weaving sulfur-carbon composite cathodes for high rate lithium-sulfur batteries. *Phys.Chem.Chem.Phys.* 14 (2012) 14495.

[53]. **Qui L., Manthiram A.** A Facile Layer-by-Layer Approach for High-Areal-Capacity Sulfur Cathodes. *Adv. Mater.* 27 (2015) 1694.

[54]. **Zhang S.S.** Does the sulfur cathode require good mixing for a liquid electrolyte lithium/sulfur cell. *Electrochem.Commun.* 31 (2012) 10.

[55]. **Seh Z.W., Li W., Cha J., Zheng G., Yang Y., McDowell M.T., Hsu P-C., Cui Y.** Sulphur-TiO2 yolk-shell nanoarchitecture with internal void space for long-cycle lithium-suphur batteries. *Nat.Commun.* 4:1331 (2013).

[56]. **Xiao L., Cao Y., Xiao J., Schwenzer B., Engelhard M.H., Saraf L.V., Nie Z., Exarhos G.J., Liu J.** A Soft Approach to Encapsulate Sulfur: Polyaniline Nanotubes for Lithium-Sulfur Batteries with Long Cycle Life. *Adv.Maer.* 24 (2012) 1176.

[57]. **Yin L., Wang J., Yang J., Nuli Y.** A novel pyrolyzed polyacrylonitrile-sulfur@MWCNT composite cathode material for high-rate rechargeable lithium/sulfur batteries. *J.Mater.Chem.* 21 (2011) 6807.

[58]. **Ji Y., Evers S., Black R., Nazar L.F.** Stabilizing lithium-sulphur cathodes using polysulphide reservoirs. *Nat.Commun.* 2:325 (2011).

[59]. **Choi Y.J., Jung B.S., Lee D.J., Jeong J.H., Kim K.W., Ahn H.J., Cho K.K., Gu H.B.** Electrochemical properties of sulfur electrode containing nano Al2O3 for lithium/sulfur cell. *Phys.Scr.* T129 (2007) 62.

[60]. **Hart C.J., Cuisinier M., Liang X., Kundu D., Garsuch A., Nazar L.F.** Rational design of sulphur host materials for Li-S batteries: correlating lithium polysulphide adsorptivity and self-discharge capacity loss. *Chem. Commun.* 51 (2015) 2308.

[61]. **Liang X., Hart C., Pang Q., Garsuch A., Weiss T., Nazar L.F.** A highly efficient polysulfide mediator for lithium-sulfur batteries. *Nat. Commun.* 6 (2015).

[62]. **Lacey M.J., Jeschull F., Edström K., Brandell D.** Why PEO as a binder or polymer coating increases capacity in the Li-S system. *Chem.Commun.* 49 (2013) 8531.

[63]. **Chen L., Shaw L.L.** Recent advances in lithium-sulfur batteries. *J.Power Sources* . 267 (2014) 770.

[64]. **Rao M., Song Y., Liao H., Cairns E.J.** Carbon nanofiber-sulfur composite cathode materials with different binders for secondary Li/S cells. *Electrochim.Acta.* 65 (2012) 228.

[65]. **Schneider H., Garsuch A., Panchenko A., Gronwald O., Janssen N., Novák P.** Influence of different electrode compositions and binder materials on the perfromance of lithium-sulfur batteries. *J.Power Sources.* 205 (2012) 420.

[66]. **Seh Z.W., Zhang Q., Li W., Zheng G., Yao H., Cui Y.** Stable cycling of lithium sulfide cathodes through strong affinity with a bifunctional binder. 4 (2013) 3673.

[67]. **Arora P., Zhang Z.** Battery Separators. *Chem. Rev.* 104 (2004) 4419.

[68]. **Bauer I., Thieme S., Brückner J., Althues H., Kaskel S.** Reduced polysulfide shuttle in lithium-sulfur batteries using Nafion-based separators. *J. Power Sources.* 251 (2014) 417.

[69]. **Huang J-Q., Zhang Q., Peng H-J., Liu X-Y., Qian W-Z., Wei F.** Ionic shield for polysulfides towards highly-stable lithium-sulfur batteries. *Energy Environ.Sci.* 7 (2014) 347.

[70]. **Jin X., Xie K., Hong X., Hu Z., Liu X.** Application of lithiated Nafion ionomer film as functional separator for lithium sulfur cells. *J. Power Sources.* 218 (2012) 163.

[71]. **Xu W., Wang J., Ding F., Chen X., Nasybulin E., Zhang Y. Zhang J-G.** Lithium metal anodes for rechargeable batteries. *Energy Environ. Sci.* 7 (2014) 513.

[72]. **USGS.** [Online] [Cited: 02 02 2015.] http://pubs.usgs.gov/fs/2014/3035/.

[73]. **Kanamura K.** Negative Electrodes: Lithium Metal. Garche J. *Encyclopedia of Electrochemical Power Sources.* Elsevier B.V. (2009) 27.

[74]. **Peled E.** The Electrochemical Behavior of Alkali and Alkaline Earth Metals in Nonaqueous Battery Systems - The Solid Electrolyte Interphase Model. *J. Electrochem. Soc.* 126 (1979) 2197.

[75]. **Aurbach D., Zaban A.** Impedance spectroscopy of lithium electrodes Part 2. The behaviour in propylene carbonate solutions - The significance of the data obtained. *J. Electroanal. Chem.* 367 (1994) 15.

[76]. **Möller K.-C., Winter M.** Skriptum. *Skript zum Praktikum Anorganisch-Chemische Technologie.* TU Graz : s.n., 2005.

[77]. **Aurbach D., Pollak E., Elazari R., Salitra G., Kelley C.S., Afinito J.** On the Surface Chemical Aspects of Very High Energy Density Rechargeable Li-Sulfur Batteries. *J. Electrochem. Soc.* 156 (2009) A694.

[78]. **Aurbach D., Zinigrad E., Cohen Y., Teller H.** A short review of failure mechanisms of lithium metal and lithiated graphite andoes in liquid electrolyte solutions. *Solid State Ionics.* 148 (2002) 405.

[79]. **Li Z., Juang J., Liaw B.Y., Metzler V., Zhang J.** A review of lithium deposition in lithium-ion and lithium metal secondary batteries. *J. Power Sources.* 254 (2014) 168.

[80]. **Hirai T., Yoshimatsu I., Yamaki J.** Influence of Electrolyte on Lithium Cycling Efficiency with Pressurized Electrode Stack. *J. Electrochem. Soc.* 141 (1994) 611.

[81]. **Ma G., Wen Z., Wu M., Shen C., Wang Q., Jin J., Wu X.** A lithium anode protection guided highly-stable lithium-sulfur battery. *Chem. Commun.* 50 (2014) 14209.

[82]. **Demir-Cakan R., Morcrette M., Babu G., Gueguen A., Dedryvere R., Tarascon J-M.** Li-S batteries: simple approaches for superior performance. *Energy Environ. Sci.* 6 (2013) 176.

[83]. **Zhang X., Wang, W., Wang A., Huang Y., Yuan K., Yu Z., Qui J., Yang Y.** Improved cycle stability and high security of Li-B alloy anode for lithium-sulfur battery. *J. Mater. Chem. A.* 2 (2014) 11660.

[84]. **Kim H., Lee J. T., Lee D-C., Oschatz M., Cho W.I., Kaskel S., Yushin G.** Enhancing performance of Li-S cells using a Li-Al alloy anode coating. *Electrochem. Commun.* 36 (2013) 38.

[85]. **Elazari R., Salitra G., Gershinsky G., Garsuch A., Panchenko A., Aurbach D.** Rechargeable lithiated silicon-sulfur (SLS) battery prototypes. *Electrochem. Commun.* 14 (2012) 21.

[86]. **Hagen M., Quiroga-González E., Dörfler S., Fahrer G., Tübke J., Hoffmann M.J., Althues H., Speck R., Krampfert M., Kaskel S., Föll H.** Studies on preventing Li dendrite formation in Li-S batteries by using pre-lithiated Si microwire anodes. *J. Power Sources.* 248 (2014) 1058.

[87]. **Xin Y., Yin Y-X., Guo Y-G. Wan L.J.** A High-Energy Room-Temperature Sodium-Sulfur Battery. *Adv. Mater.* 26 (2014)1261.

[88]. **Ellis B. L., Nazar L. F.** Sodium and sodium-ion energy storage batteries. *Current Opinion in Solid State and Materials Science .* 16 (2012) 168.

[89]. **Xu K.** Nonaqueous Liquid Electrolytes for Lithium-Based Rechargeable Batteries. *Chem. Rev.* 104 (2004) 4303.

[90]. **Scheers J., Fantini S., Johansson P.** A review of electrolytes for lithium-sulphur batteries. *J. Power Sources.* 255 (2014) 204.

[91]. **Rauh R.D., Shuker F.S., Marston J.M., Brummer S.B.** Formation of Lithium Polysulfides in aprotic media. *J. inorg. nucl. Chem.* 39 (1977) 1761.

[92]. **Xin S., Gu L., Zhao N-H., Yin Y-X., Zhou L-J., Guo Y-G., Wan Li-J.** Smaller Sulfur Molecules Promise Better Lithium-Sulfur Batteries. *J. Am. Chem. Soc.* 134 (2012) 18510.

[93]. **Wang L., He X., Li J., Chen M., Gao J., Jiang C.** Charge/discharge characteristics of sulfurized polyacrylonitrile composite with different sulfur content in carbonate based electrolyte for lithium batteries. *Electrochim.Acta.* 72 (2012) 114.

[94]. **Yim T., Park M-S., Yu J-S., Kim K.J., Im K-Y., Kim J-H., Jeong G., Jo Y. N., Woo S-G., Kang K.S., Lee I., Kim Y-J.** Effect of chemical reactivity of polysulfide toward carbonate-based electrolyte on the electrochemical performance of Li-S batteries. *Electrochmicia Acta.* 107 (2013) 454.

[95]. **Brouillette D., Perron G., Desnoyers J.E.** Effect of viscosity and volume on the specific conductivity of lithium salts in solvent mixtures. *Electrochim. Acta.* 44 (1999) 4721.

[96]. **Gutmann V.** Empirical Parameters for Donor and Acceptor Properties of Solvents. *Electrochim. Acta.* 21 (1976) 661.

[97]. **Olsher U., Izatt R.M., Bradshaw J.S., Dalley N.K.** Coordination Chemistry of Lithium Ion: A Crystal and Molecular Structure Review. *Chem. Rev.* 91 (1991) 137.

[98]. **Henderson W., A.** Glyme-Lithium Salt Phase Behavior. *J.Phys.Chem.B.* 110 (2006) 13177.

[99]. **Barchasz C., Leprêtre J-C., Patoux S., Alloin F.** Electrochemical properties of ether-based electrolytes for lithium/sulfur rechargeable batteries. *Electrochim. Acta.* 89 (2013) 737.

[100]. **Park M S., Ma S.B., Lee D.J., Im D., Doo S-G., Yamamoto O.** A Highly Reversible Lithium Metal Anode. *Sci. Rep.* 4 (2014) 3815.

[101]. **Yoon S., Lee Y-H., Shin K-H., Cho S.B., Chung W. J.** Binary sulfone/ether-based electrolytes for rechargeable lithium-sulfur batteries. *Electrochim. Acta.* 145 (2014) 170.

[102]. **Chen R., Zhao T., Wu F.** From a historic review to horizons beyond: lithium-sulphur batteries run on the wheels. *Chem. Commun.* 51 (2015) 18.

[103]. **Suo L., Hu Y-S., Li H., Armand M., Chen L.** A new class of Solvent-in-Salt electrolyte for high-energy rechargeable metallic lithium batteries. *Nat. Commun.* 4 (2013) 1481.

[104]. **Zhang S.S.** Role of LiNO3 in rechargeable lithium/sulfur battery. *Electrochim.Acta.* 70 (2012) 344.

[105]. **Zhang S.S., Read J.A.** A new direction for the performance improvment of rechargeable lithium/sulfur batteries. *J.Power Sources.* 200 (2012) 77.

[106]. **Mikhaylik J.V.** *Electrolytes for lithium sulfur cells. 7354680* USA, 2008.

[107]. **Zhang S.S.** Effect of Discharge Cutoff Voltage on Reversibility of Lithium/Sulfur Batteries with LiNO3-Contained Electrolyte. *J. Electrochem. Soc.* 159 (2012) A920.

[108]. **Aurbach D., Pollak E., Elazari R., Salitra G., Kelley C.S., Afinito J.** On the Surface Chemical Aspects of Very High Energy Density Rechargeable Li-Sulfur Batteries. *J. Electrochem. Soc.* 158 (2009) A694.

[109]. **Wang S., Yasukawa E., Mori S.** Inhibition of anodic corrosion of aluminum cathode current collector on recharging in lithium imide electrolytes. *Electrochim, Acta.* 45 (2000) 2677.

[110]. **Aurbach D., Zinigrad E., Teller H., Cohen Y., Salitra G., Yamin H., Dan P., Elster E.** Attempts to Improve the Behavior of Li Electrodes in Rechargeable Lithium Batteries. *J. Electrochem. Soc.* . 149 (2002) A1267.

[111]. **Choi J-S., Kom J-K., Cherubally G., Ahn J-H., Ahn H-J., Kim K-W.** Rechargeable lithium/sufur battery with suitable mixed liquid electrolytes. *Electrochim. Acta.* 52 (2007) 2075.

[112]. **Lin Z., Liu Z., Fu W., Dudney N. J., Liang C.** Phosphorous Pentasulfide as a Novel Additive for High-Performance Lithium-Sulfur Batteries. *Adv. Funct. Mater.* . 23 (2013) 1064.

[113]. **Zu C., Manthiram A.** Stabilized Lithium-Metal Surface in a Polysulfide-Rich Environment of Lithium-Sulfur Batteries. *J. Phys. Chem. Lett.* 5 (2014) 2522.

[114]. **Zhang S.S.** New insight into liquid electrolyte of rechargeable lithium/sulfur battery. *Electrochim. Acta.* 97 (2013) 226.

[115]. **Lee D-J., Agostini M., Park J-W., Sun Y-K., Hassoun J., Scrosati B.** Progress in Lithium-Sulfur Batteries: The Effective Role of a Polysulfide-Added Eelctrolyte as Buffer to Prevent Cathode Dissolution. *ChemSusChem.* 6 (2013) 2245.

[116]. **Shin E. S., Kim K., Oh S. H., Cho W. I.** Polysulfide dissolution control: the common ion effect. *Chem. Comm.* 49 (2013) 2004.

[117]. **Hu J.J., Long G.K., Liu S., Li G.R., Gao X.P.** A LiFSI-LiTFSI binary-salt eelctrolyte to achieve high capacity and cycle stability for a Li-S battery. *Chem. Chommun.* 50 (2014) 14647.

[118]. **Ding F., Xu W., Graff G.L., Zhang J., Sushko M.L., Chen X., Shao Y., Engelhard M.H., Nie Z., Xiao J., Liu X., Sushko P.V., Liu J., Zhang J-G.** Dendrite-Free Lithium Deposition via Self-Healing Electrostatic Shield Mechanism. *J. Am. Chem. Soc.* 135 (2013) 4450.

[119]. **Zhang, Y., Quian J., Yu W., Russell S. M., Chen X., Nasybulin E., Bhattacharya P., Engelhard M.H., Mei D., Cao R., Ding F., Cresce A.V., Xu K., Zhang J-G.** Dendrite-Free Lithium Deposition with Self-Aligned Nanorod Structure. *Nano Lett.* 14 (2014) 6889.

[120]. **Tatsumisago M., Nagao M., Hayashi A.** Recent development of sulfide solid electrolytes and interfacial modification for all-solid-state rechargeable lithium batteries. *J. Asian Ceram. Soc.* 1 (2013)17.

[121]. **Lin Z., Liu Z., Fu W., Dudney N. J., Liang C.** Lithium Polysulfidophophates: A Familiy of Lithium-Conducting Sulfur-Rich Compounds for Lithium-Sulfur Batteries. *Angew. Chem. Int. Ed.* 52 (2013) 7460.

[122]. **Nagata H., Chikusa Y.** A lithium sulfur battery with high power density. *J. Power Sources.* 264 (2014) 206.

[123]. **Kamaya N., Homma K., Yamakawa Y., Hirayama M., Kanno R., Yonemura M, Kamiyama T., Kato Y., Hama S., Kawamoto K., Mitsui A.** A lithium superionic conductor. *Nat. Mater.* 10 (2011) 682.

[124]. **Kovačič S., Preishuber-Pflügl F., Slugovc C.** Macroporous Polyolefin Membranes from Dicyclopentadiene High Internal Phase Emulsions: Preparation and Morphology Tuning. *Macromol. Mater. Eng.* 299 (2014) 843.

[125]. **Kovačič S.** Ring Opening Metathesis Polymerisation (ROMP) As a Tool for PolyHIPEs With Extraordinary Mechanical Properties. *Acta Chim. Slov.* 60 (2013) 448.

[126]. **Gruber K.** Untersuchung des Einflusses relevanter Faktoren auf die elektrochemische Leistungsfähgkeit von Lithium-Schwefel-Batterien. *Diplomarbeit.* (2011).

[127]. **Scharfegger M., Fuchsbichler B., Koller S., Slugovc C., Kovacic S.** *Method for producing a porous carbon material and porous carbon material which can be produced by process. WO 2013/178371 A1* 5 12 2013.

[128]. **Kovačič S., Krajnc P., Slugovc C.** Inherently reactive polyHIPE material from dicyclopentadiene. *Chem. Commun. .* 46 (2010) 7504.

[129]. **Khosravi E., Szymanska-Buzar T.** *Ring Opening Methatesis Polymerisation and Related Chemistry.* s.l. : Kluwer Acacdemic Publishers, 2002, 258.

[130]. **Leitgeb A., Wappel J., Urbina-Blanco C.A., Strasser S., Wappl C., Casin C.S.J., Slugovc C.** Two commercially available initiators for the retarded ring-opening metathesis polymerzation of dicyclopentadiene. *Monatsh Chem .* 145 (2014) 1513.

[131]. **Preishuber-Pflügl F.** Präparation und Charakterisierung 3-dimensional-strukturierter Elektrodenmaterialien aus PolyHIPE-Membran Templates. *VMI document.* (2012).

[132]. **Agrawal M., Choudhury S., Gruber K., Simon F., Fischer D., Albrecht V., Göbel M., Koller S., Stamm M., Ionov L.** Porous carbon materials for Li-S batteries based on resorcinol-formaldehyde resin with inverse opal structure. *J. Power Sources.* 261 (2014) 363.

[133]. **Pötz S.** High Capacity Electrodes for Lithium-Ion Batteries. *Dissertation.* (2014).

[134]. **Kovačič S., Matsko N.B., Gruber K., Koller S., Slugovc C.** Ring-Opening Metathesis Polymerization / soft templating approach towards highly conductive macroporous carbon-foams. *yet unpublished.* (2014).

[135]. NPL National Physical Laboratory. [Online] [Cited: 2015 06 02.] http://www.kayelaby.npl.co.uk/general_physics/2_3/2_3_5.html.

[136]. **Westmetall.** [Online] [Cited: 05 05 2015.] http://www.westmetall.com/de/markdaten.php.

[137]. **Chung J.-S., Sohn H.-J.** Electrochemical behaviors of CuS as a cathode materials for lithium secondary batteries. *J. Power Sources.* 108 (2002) 226.

[138]. **Jache B., Mogwitz B., Klein F., Adelhelm P.** Copper sulfides for rechargeable lithium batteries: Linking cycling stability to electrolyte composition. *J. Power Sources.* 247 (2014) 703.

[139]. **Kovačič S., Kren H., Kranjc P., Koller S., Slugovc C.** The Use of an Emulsion Templated Microcellular Poly(dicyclopentadiene-co-norbornene) Membrane as a Separature in Lithium-Ion Batteries. *Macromol. Rapid Commun.* 34 (2013) 581.

[140]. **Saufi S.M., Ismail A.F.** Fabrication of carbon membranes for gas separation - a review. *Carbon.* 42 (2004) 241.

[141]. **Gireaud L., Grugeon S., Laruelle S., Yrieix B., Tarascon J-M.,.** Lithium metal stripping/plating mechanismus studies: A metallurgical approach. *Electrochem. Commun.* 8 (2006) 1639.

[142]. **Belt, J. R., Bernardi D.M., Utgikar V.,.** Development and Use of a Lithium-Metal Reference Electrode in Aging Studies of Lithium-Ion Batteries. *J. Electrochem. Soc.* 161 (2014) A1116.

[143]. **Thieme S., Brückner J., Meier A., Bauer I., Gruber K., Kaspar J., Helmer A., Althues H., Schmuck M., Kaskel S.** A lithium-sulfur full cell with ultralong cycle life: influence of cathode structure and polysulfide additive. *J. Maer. Chem. A.* 3 (2015) 3808.

[144]. **Hagen M., Franz P., Tübke J.** Cell energy ensity and electrolyte/sulfur ratio in Li-S cells. *J. Power Sources.* 264 (2014) 30.

[145]. **Yang Y., Zheng G., Cui Y.** Nanostructured sulfur cathodes. *Chem.Soc.Rev.* 42 (2013) 3018.

[146]. **Wagner M.W., Liebenow C., Besenhard J.O.** Effect of polysulfide-containing electrolyte on the film formation of the negative electrode. *J. Power Sources.* 68 (1997) 328.

Supporting information

Supporting information:4.2.1.4 Preparation of HIPE structured carbon layer on Al-, Cu- foil and Ni-mesh :

Element	mass%	atomic%	mass%	atomic%
	Al surface		Al surface yellow discoloration	
C K	7.93	15.35	13.76	22.70
O K	9.49	13.80	28.05	34.74
Al K	81.88	70.56	57.71	42.39
Fe K	0.70	0.29	0.48	0.17
Total	100			

Table 4: investigation of elemental composition of Al surface after polyDCPD coating and oxidation

Supporting information: chapter 4.4.1 Practically obtained energy densities in lab-scale Li-S cells

Galvanostatic cycling performance of Li-S pouch cell with increased capacity of ~135 mAh applying an electrolyte ratio of 8 µl/mgS and a unlimited Li capacity (230 µm lithium foil) for comparison to cycling performance of the discussed cell in chapter 4.4.1.

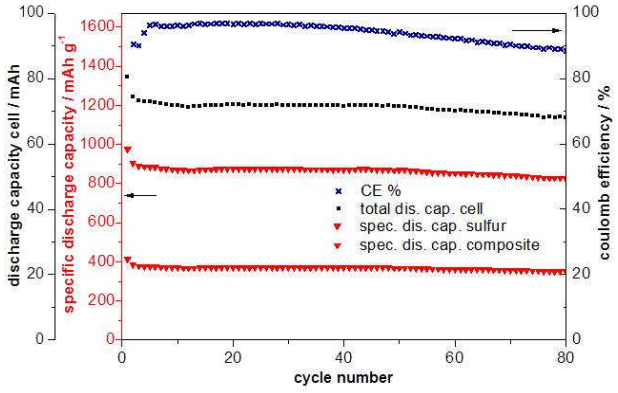

Figure 52: cycling performance of a comparable cell to chapter 4.4.1 but at higher electrolyte and lithium capacity

Supporting information on energy density calculations in 4.4.2. Theoretical calculations of energy densities of Li-S cells:

3-fold lithium capacity, spec. sulfur capacity 800 mAh/g							
sulfur loading	**S in**	**sulfur**	**electrode**	**density**	**electrolyte**	**energy**	**energy density**

[mgS/cm2]	electrode [w%]	capacity [mAh/g]	thickness [µm]	[g/cm3]	[µl/mgS]	[mWh/cell]	[mWh/g]
1,7	42,5	800	74µm	0,53	129	136	269
					110	136	199
					96	136	158
					86	136	131
2,4	60	800	74µm	0,53	173	193	341
					141	193	236
					119	193	180
					103	193	146
3,1	80	800	74µm	0,53	217	257	408
					169	257	266
					139	257	197
					117	257	157
3-fold lithium capacity, spec. sulfur capacity 1200 mAh/g							
sulfur loading [mgS/cm2]	**S in electrode [w%]**	**sulfur capacity [mAh/g]**	**electrode thickness [µm]**	**density [g/cm3]**	**electrolyte [µl/mgS]**	**energy [mWh/cell]**	**energy density [mWh/g]**
1,7	42,5	800	74µm	0,53	189	205	385
					162	205	288
					142	205	230
					126	205	192
2,4	60	800	74µm	0,53	251	289	482
					206	289	339
					174	289	262
					151	289	213
3,1	80	800	74µm	0,53	313	385	570
					246	385	381
					203	385	286
					172	385	229
3-fold lithium capacity, spec. sulfur capacity 1600 mAh/g							
sulfur loading [mgS/cm2]	**S in electrode [w%]**	**sulfur capacity [mAh/g]**	**electrode thickness [µm]**	**density [g/cm3]**	**electrolyte [µl/mgS]**	**energy [mWh/cell]**	**energy density [mWh/g]**
1,7	42,5	800	74µm	0,53	246	273	490
					212	273	371
					186	273	299
					166	273	250

2,4	60	800	74µm	0,53	324	385	608
					267	385	435
					228	385	339
					198	385	277
3,1	80	800	74µm	0,53	401	514	711
					318	514	485
					263	514	369
					225	514	297

Table 5: Calculated specific energy density values depicted in Figure 51 for 3-fold lithium capacity and spec. sulfur capacity of 800 mAh/g, 1200 mAh/g and 1600 mAh/g

5-fold lithium capacity, spec. sulfur capacity 800 mAh/g							
sulfur loading [mgS/cm2]	**S in electrode [w%]**	**sulfur capacity [mAh/g]**	**electrode thickness [µm]**	**density [g/cm3]**	**electrolyte [µl/mgS]**	**energy [mWh/cell]**	**energy density [mWh/g]**
1,7	42,5	800	74µm	0,53	151	387	252
					126	387	190
					108	387	152
					95	387	127
2,4	60	800	74µm	0,53	197	546	315
					157	546	223
					130	546	173
					111	546	141
3,1	80	800	74µm	0,53	242	729	371
					184	729	250
					148	729	188
					124	729	151
5-fold lithium capacity, spec. sulfur capacity 1200 mAh/g							
sulfur loading [mgS/cm2]	**S in electrode [w%]**	**sulfur capacity [mAh/g]**	**electrode thickness [µm]**	**density [g/cm3]**	**electrolyte [µl/mgS]**	**energy [mWh/cell]**	**energy density [mWh/g]**
1,7	42,5	800	74µm	0,53	216	581	352
					182	581	269
					157	581	218
					138	581	183
2,4	60	800	74µm	0,53	279	820	432
					224	820	314
					188	820	246

					161	820	203
3,1	80	800	74µm	0,53	338	1093	501
					261	1093	349
					213	1093	267
					180	1093	217
5-fold lithium capacity, spec. sulfur capacity 1600 mAh/g							
sulfur loading [mgS/cm2]	**S in electrode [w%]**	**sulfur capacity [mAh/g]**	**electrode thickness [µm]**	**density [g/cm3]**	**electrolyte [µl/mgS]**	**energy [mWh/cell]**	**energy density [mWh/g]**
1,7	42,5	800	74µm	0,53	275	774	438
					233	774	341
					203	774	279
					179	774	236
2,4	60	800	74µm	0,53	351	1093	530
					286	1093	394
					241	1093	313
					208	1093	260
3,1	80	800	74µm	0,53	421	1457	607
					330	1457	435
					272	1457	338
					231	1457	277

Table 6: Calculated specific energy density values depicted in Figure 51 for 5-fold lithium capacity and spec. sulfur capacity of 800 mAh/g, 1200 mAh/g and 1600 mAh/g